

**A study on
bi-directional hydrogen isotopes
permeation through the first wall of
a magnetic fusion power reactor**

Haishan ZHOU

Doctor of Philosophy

**Department of Fusion Science
School of Physics Sciences
The Graduate University for Advanced Studies**

2014

Abstract

For the construction of magnetic fusion reactors, reduced activation ferritic steels (RAFSs) such as F82H are currently considered to be the candidate materials for the first wall. In this PhD thesis research, one of the technical issues related to hydrogen isotopes transport through the first wall has been studied. For the blankets employing self-cooled breeder, the first wall is exposed to the edge plasma, containing energetic D^+ and T^+ on the one side and on the other side it is exposed to T_2 gas bred in blankets. Under these conditions, it is highly possible that these hydrogen isotopes would penetrate the first wall by a phenomenon called “bi-directional permeation”: (1) deuterium as well as tritium would transport into the blanket by plasma-driven permeation (PDP), which will hinder the recovery of tritium and will probably necessitate isotope separation; and (2) tritium would flow in the counter direction to the edge plasma by gas-driven permeation (GDP), which will affect edge plasma density. Despite its critical importance, there have been neither experimental nor theoretical studies on bi-directional permeation of hydrogen isotopes through reduced activation alloys. This PhD thesis research aims to understand the physical mechanisms driving hydrogen isotopes permeation processes and to establish fundamental knowledge databases for designing fusion power reactors.

Hydrogen permeation through a reduced activation ferritic steel alloy: F82H has been investigated in a steady state laboratory-scale plasma device: VEHICLE-1 under some of the reactor-relevant conditions. In PDP experiments, the hydrogen permeation flux is measured by a quadrupole mass spectrometer (QMS) at the downstream side. The plasma density is of the order of 10^9 - 10^{10} cm^{-3} and the electron temperature is ~ 3 eV. The particle bombarding energy is controlled by a negative bias voltage applied on the membrane flange. The net hydrogen implantation flux is estimated by taking into account the hydrogen species mix and reflection coefficient data. In GDP experiments, the upstream hydrogen gas pressure is 1.3×10^4 - 10^5 Pa measured by an absolute pressure gauge and the hydrogen permeation flux is measured by another QMS in VEHICLE-1 chamber. For all the permeation experiments, the

membrane samples made of F82H and SUS304 are prepared in the same dimensions as those commercially available conflat flanges with an outer diameter of 70 mm, except that a circular area of 35 mm in diameter inside the knife-edge is machined down to thicknesses of 0.5 to 5 mm. A resistive heater is set beneath the membrane and the sample temperature varies from 220 °C to 520 °C.

The hydrogen transport parameter data taken for SUS304 have been found to be in good agreement with the literature data, which means that the experimental setup on VEHICLE-1 is valid for the evaluation of other first wall candidate materials. Both GDP and PDP data through F82H show thickness dependence, suggesting that hydrogen permeation is diffusion-limited under some of the reactor-relevant conditions. The hydrogen transport parameters such as permeability, solubility, diffusion coefficient and surface recombination coefficient have been successfully measured for F82H. In particular, the surface recombination coefficient, which is essential to correctly predict the hydrogen isotopes permeation flux through the first wall, has been experimentally measured for the first time. Using the measured parameters and the steady state permeation model, hydrogen isotopes permeation flux and the dynamic wall inventory under some of the reactor-relevant conditions have been evaluated.

The surface effects on hydrogen PDP have been investigated from two aspects: surface contamination and morphology. A new model has been proposed to interpret the surface condition effects. Thick surface impurity film has been found to act as a second layer for diffusion and reduce the permeation flux in both laboratory and tokamak experiments. A decrease in steady state permeation flux has been measured when increasing plasma-facing surface area, which is in agreement with the theoretical prediction, i.e., the steady state permeation flux is inversely proportional to the square root of surface area. Experiments indicate that the permeation flux can be further reduced by simultaneous surface oxidization and area modification.

As a proof-of-principle experiment, first wall particle flux measurements in the QUEST spherical tokamak have been conducted, using a permeation probe that employs F82H as the

membrane and also SUS304 as a comparative reference membrane. Permeation measurements have been done during the conditioning steady state discharges heated with 2.45 GHz and 8.2 GHz ECR. Diffusion and surface recombination coefficients measured in VEHICLE-1 are used to interpret the results from the permeation probe measurements in QUEST. A much shorter PDP breakthrough time and higher steady state permeation flux have been found for F82H than SUS304, which is consistent with the results from VEHICLE-1 experiments. The effect of plasma heating power indicates that the steady state permeation flux is roughly proportional to the square root of the implantation flux. The F82H permeation probe shows good sensitivity to the variation of plasma parameters.

Bi-directional hydrogen (H) permeation has actually been demonstrated for the first time in a laboratory-scale steady state plasma facility. Gas-driven permeation hydrogen flows from the gas-facing surface into helium, argon and hydrogen plasmas have been measured. For the bi-directional hydrogen permeation experiments, the membrane temperature is set between 550 and 600 °C, the hydrogen gas pressure for GDP is increased to 9.3×10^4 Pa. At the plasma side, the electron temperature is raised up to ~ 10 eV for the improved sensitivity of H_α spectroscopy. Experiments indicate that gas-driven permeation can take place in the opposite direction of plasma-driven permeation, which then results in an unwanted increase in edge plasma density. A one-dimensional diffusion code: DIFFUSE has been utilized to simulate the experiment. The modelling result has been found to be in relatively good agreement with the experimental data. Hydrogen PDP flow from the plasma side to the gas side has been detected as well. The driving pressure for GDP has been found to decrease slower when a bias is applied to the sample, suggesting a PDP flow into the gas side.

DIFFUSE-code has extensively been executed, employing multiple hydrogen isotopes (D/T) for bi-directional permeation. The input data for DIFFUSE are such that the thickness of a membrane made of α -Fe (used as a surrogate of F82H) is 5 mm, the D/T inflows from the upstream (plasma-facing) side are driven by PDP with D/T implantation fluxes of 5×10^{15} D/cm²/s and 5×10^{15} T/cm²/s at a bombarding energy of 100 eV. The T inflow from the downstream (gas-facing) side is driven by GDP. Results indicate that the same isotopic

species interact with each other in the two counter flows. Deuterium flow appears to be independent of these tritium flows, driven by its own concentration gradient.

Re-analysis of the tritium flows in a FLiBe loop has been performed, taking into account tritium leakage from the first wall. The tritium pressure has been found to be $\sim 1.1 \times 10^3$ Pa, which is $\sim 10\%$ of the tritium equilibrium pressure in FLiBe at a temperature of 527°C . Under these conditions, $\sim 68\%$ of the bred tritium will be released at the plasma side by GDP. Assuming a particle reflection coefficient of 0.5 and a total incident flux of 2.0×10^{16} D&T/cm²/s, the first wall recycling rate has been estimated to be 1.006.

Acknowledgement

Foremost, I would like to express my sincere gratitude to my advisor Prof. Yoshihiko Hirooka for his guidance, caring, and providing me with an excellent opportunity to learn from him. I will cherish all the moments when we worked together and all the fun we had together.

My deeply thanks also goes to my vice-advisor Dr. Naoko Ashikawa for her supports to my experiments and her help with my life in Japan.

I want to express my gratitude to the rest of my thesis committee: Prof. Yukio Nakamura, Prof. Hideki Zushi, Prof. Yousuke Nakashima and Dr. Teruya Tanaka for their insightful comments, suggestions and questions, which are extremely important to improve my thesis.

I am very grateful to Prof. Takeo Muroga, Prof. Akio Sagara, Prof. Suguru Masuzaki, Prof. Izumi Murakami, Prof. Shoichi Okamura, Prof. Nagato Yanagi, Dr. Daiji Kato, Dr. Takuya Nagasaka, Dr. Masayuki Tokitani, Dr. Sadatsugu Takayama and Dr. Juro Yagi for their helps and caring.

I would like to thank Japan Atomic Energy Agency, Naka Fusion Institute for the material preparation.

I would like to express my thanks to the Graduate University for Advanced Studies (SOKENDAI) and the National Institute for Fusion Science (NIFS) for the financial supports during my PhD study.

A special thanks goes to Prof. Guang-nan Luo for his encouragements and supports for this oversea PhD study.

I would like to express my deeply gratitude to my friends, Erhui Wang, Tingfeng Ming, Pengfei Zheng, Yanfen Li, Shigenori Mizuno san, Hao Wang, Haiying Fu, Xiaodi Du, Hongming Zhang, Xianli Huang, Shaofei Geng, Chunfeng Dong, Xiang Ji, Xiaobing Ding, Botsz Huang for their encouragements and helps. I could not have imagined living in a foreign country without you.

*I dedicate this thesis to
my family and my wife, Sisi,
for their constant support.*

I love you all.

Contents

Abstract	I
Acknowledgement	V
Contents	VII
Chapter 1 Introduction	1
1.1. Nuclear fusion research.....	2
1.2. Reactor blanket and the first wall	4
1.3. Hydrogen isotopes permeation issues	8
1.4. Objectives of this work	15
1.5. Outline of the thesis	16
Reference	17
Chapter 2 Theories on hydrogen isotopes transport through solids	23
2.1. Entering and release of hydrogen isotopes in solids.....	24
2.1.1. Reflection and implantation.....	24
2.1.2. Solution.....	27
2.1.3. Diffusion and trapping	28
2.1.4. Surface recombination	29

2.2. Steady state permeation models.....	29
2.3. Isotope effects	32
2.4. Summary	34
Reference	35

Chapter 3 Hydrogen gas- and plasma-driven permeation through a reduced activation steel alloy F82H..... 37

3.1. VEHICLE-1 linear plasma facility and the permeation experimental setup	38
3.2. Characterization of hydrogen plasmas in VEHICLE-1	40
3.3. Sample preparation and analysis methods	45
3.4. Gas-driven permeation.....	46
3.5. Plasma-driven permeation	55
3.6. Surface effects on plasma-driven permeation.....	61
3.6.1. Models on surface modification effects on PDP.....	61
3.6.2. Surface condition effects experiments	64
3.7. Discussion	68
3.7.1. Comparison of the PDP behavior for F82H and SUS304.....	68
3.7.2. Compound surface condition effects on PDP	70
3.7.3. Comparison of hydrogen PDP and GDP through F82H.....	71
3.8. Summary	73
Reference	74

Chapter 4 Plasma-driven permeation through F82H in QUEST..... 79

4.1. QUEST spherical tokamak	80
------------------------------------	----

4.2. Permeation experimental setup in QUEST	81
4.3. Results and discussion	84
4.3.1. PDP through F82H and SUS304 membranes in QUEST	84
4.3.2. Effect of plasma heating power	88
4.3.3. Diffusivity measurements for F82H from the PDP data taken in QUEST	89
4.4. Summary	93
Reference	94
Chapter 5 Bi-directional hydrogen (H) permeation experiments and modelling	97
5.1. Introduction.....	98
5.2. Experimental methods	98
5.3. Hydrogen gas-driven permeation into Ar and He plasmas	99
5.4. Hydrogen gas-driven permeation into hydrogen plasma side.....	101
5.5. DIFFUSE-code calculation for the hydrogen GDP flow	103
5.5.1. DIFFUSE-code	103
5.5.2. Input data and assumptions for the bi-directional permeation calculations.....	104
5.5.3. Calculation results and discussion	105
5.6. Hydrogen plasma-driven permeation into hydrogen gas side.....	107
5.7. Summary	109
Reference	110
Chapter 6 Bi-directional hydrogen isotopes (D/T) permeation through the first walls of fusion reactors	111

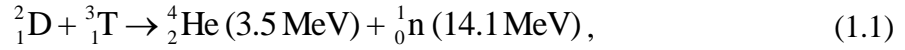
6.1. Introduction.....	112
6.2. Isotopes effects on permeation.....	112
6.2.1. Diffusivity and solubility	112
6.2.2. Recombination coefficient	113
6.2.3. Competition of the isotopes for traps.....	114
6.3. Modeling of bi-directional permeation involving multiple hydrogen isotopes	115
6.4. Re-evaluation of the tritium pressure in FLiBe blankets	118
6.5. Re-evaluation of hydrogen isotopes permeation through the first wall of FLiBe blankets	121
6.5.1. Evaluation of the hydrogen isotopes permeation fluxes.....	121
6.5.2. Evaluation of the possible impact of GDP on first wall recycling	124
6.6. Summary	125
Reference	126
Chapter 7 Summary and outlook.....	129
7.1. Summary	130
7.2. Outlook	131
List of publications	133

Chapter 1

Introduction

1.1. Nuclear fusion research

Nuclear fusion is a reaction in which atomic nuclei with lower mass collide to form a new type of atomic nucleus, accompanied by a release or absorption of energy. The primary energy source for stars is hydrogen fusion, which is also considered to be one of the most promising candidate sources to provide safe, environmentally friendly and economical energy for human beings [1-3]. Of all the possible fusion reactions the deuterium-tritium (D-T) reaction is the most attractive one because tritium and deuterium can react at relatively low energy, generating α -particle (He), neutron (n) and a large amount of energy [1]:



where the energies shown are kinetic energies of the reaction products. In a fusion plasma, the energy carried by the α -particle can be transferred to the plasma by collision so that the confined plasma can be persistently heated. Lawson [4] showed that a fusion plasma would burn to self-sustaining (ignition) if the product of energy confinement time τ_E [s] and plasma density n [m^{-3}] exceeded a given threshold for a fixed plasma temperature T [keV]. Because τ_E itself is a function of temperature, the ignition condition is more usually expressed as:

$$n \cdot T \cdot \tau_E > \sim 5 \times 10^{21} \text{ m}^{-3} \cdot \text{keV} \cdot \text{s}, \quad (1.2)$$

i.e., to achieve ignition, the high-temperature, high-density plasma must be confined in a relatively long time. In a star, the plasma is confined by the force of gravity due to the huge amount of matter. On the earth, two leading ideas are proposed to obtain usable energy from fusion reactions: magnetic confinement fusion (MCF) and inertial confinement fusion (ICF).

In MCF systems, the plasma is held by magnetic field in desired configurations. The core plasma density is kept at $\sim 10^{20} \text{ m}^{-3}$ for several seconds of confinement time to fill Eq. (1.2). From 1950's, various ideas of MCF have been proposed, among which tokamak and

stellarator are considered to be the most promising concepts to yield commercial fusion reactors. Many large and medium size MCF devices have been built, e.g., JET [5], JT-60[6], LHD [7], DIII-D [8], ASDEX-U [9], EAST [10], KSTAR [11] and QUEST [12]. Shown in Fig.1.1 is the International Thermonuclear Experimental Reactor (ITER) [13], which is under construction in Cadarache, France. ITER is planned to be the first experimental reactor to demonstrate extended burning of D-T plasmas at a few hundred MWs of fusion power and technology essential to a reactor in an integrated system, and to test nuclear components required to utilize fusion energy for practical purposes [14].

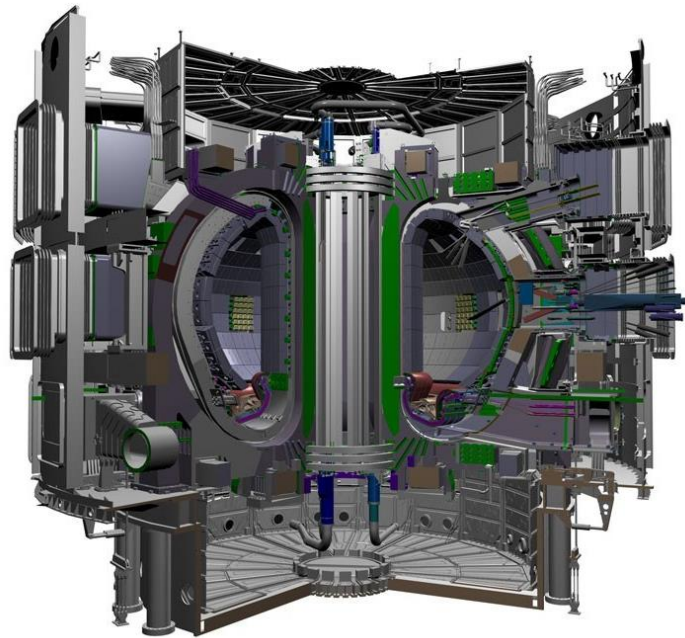


Figure 1.1 Design of ITER tokamak [13]

The MCF device beyond ITER will aim to demonstrate electricity production (DEMO reactor). SlimCS [15], PPCS-A to PPCS-D [16] and ARIES-AT [17] are several examples for tokamak type DEMO concepts. Stellarator type reactor concepts have also been proposed, for example the Force-Free Helical Reactor (FFHR) series concepts being developed by National Institute for Fusion Science in Japan [18]. Recently, some researchers suggested that a test reactor between ITER and DEMO may be necessary in the roadmap to the

realization of fusion energy. These concepts include the China Fusion Engineering Test Reactor (CFETR) [19] and the Fusion Nuclear Science Facility (FNSF) [20], which aim to provide an integrated, continuously fusion nuclear environment that can be used to investigate plasma material interactions, tritium fuel management, and power extraction, etc [20].

In contrast to MCF, ICF goes a different way to fill the Lawson Criterion. Fuel targets containing a mixture of deuterium and tritium are heated and compressed by high-energy laser lights or laser-produced X-rays to generate high temperature, high density plasmas. For the ICF plasmas, the density is usually larger than $\sim 10^{31} \text{ m}^{-3}$ while the confinement time is shorter than 10^{-10} s [21]. By present, the largest and most energetic ICF device built is the National Ignition Facility (NIF) located at the Lawrence Livermore National Laboratory in Livermore, USA [22]. Recently a fuel capsule gave off more energy than was applied to it in NIF, which is an important milestone towards commercialization of ICF [23].

On the whole, considerable progresses have been achieved for both MCF and ICF in the last 50 years, but a lot of physics and technical issues are still needed to be addressed to realize fusion energy as a power source. This thesis mainly makes a contribution to MCF research in the areas of plasma-wall interaction physics and reactor blanket engineering.

1.2. Reactor blanket and the first wall

No matter which concept is used to develop a fusion power plant, tritium, one of the fuels for D-T reaction, must be artificially produced in reactors because it is a quite limited resource due to its short half-life [24]. Tritium can be produced by the reactions between neutron and lithium (Li) isotopes as follows [25]:



Present developments in the context of fusion propose generating tritium are based on the reaction (1.3) because the reaction with the more abundant ${}^7\text{Li}$ is endothermic and has a smaller cross-section for neutrons with an energy lower than 5 MeV [25].

Lithium metal/alloys or lithium compounds are stored in the blanket structures so that lithium can capture fusion neutrons to generate tritium. This process is called *tritium breeding*, because the fusion neutrons come from the previous D-T reactions which consume tritium. Shown in Fig.1.2 is the 3D view of the FFHR2 reactor concept [18]. It can be seen that all the internal surface areas is covered by blanket structures for the highest achievable tritium breeding ratio (TBR). From the viewpoint of commercial operation, a fusion reactor must be tritium self-sustainable, which requires a TBR larger than 1 [24].

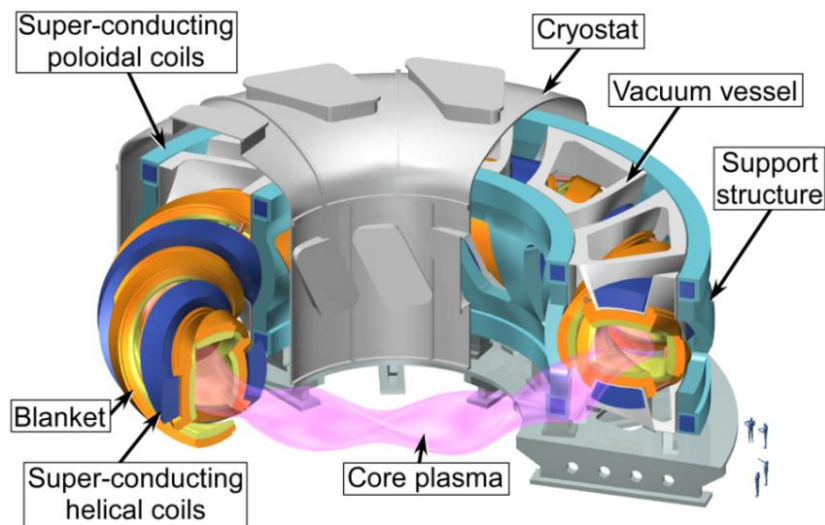


Figure 1.2 The FFHR2 reactor concept [18]

Figure 1.3 shows a module of the FFHR2 outboard blanket and (b) a schematic diagram of the blanket structure [26]. The definition of the “first wall” will be different for magnetic fusion devices up to ITER and for those to be built thereafter for power generation. It is widely recognized that ITER will generate fusion power which, however, is not intended to be converted into electrical power. This is because no complete blanket concept will be

implemented except for test blanket modules to cover only a fraction of the surface area exposed to burning plasmas. In this case, the definition of the first wall is nothing but a vacuum chamber wall to separate DT-plasma from the environment. As opposed to that, for fusion power reactors, essentially all the internal surface areas must be covered by blanket structures for the highest achievable tritium breeding ratio. *The first wall is thus redefined as the plasma-facing walls of blankets.*

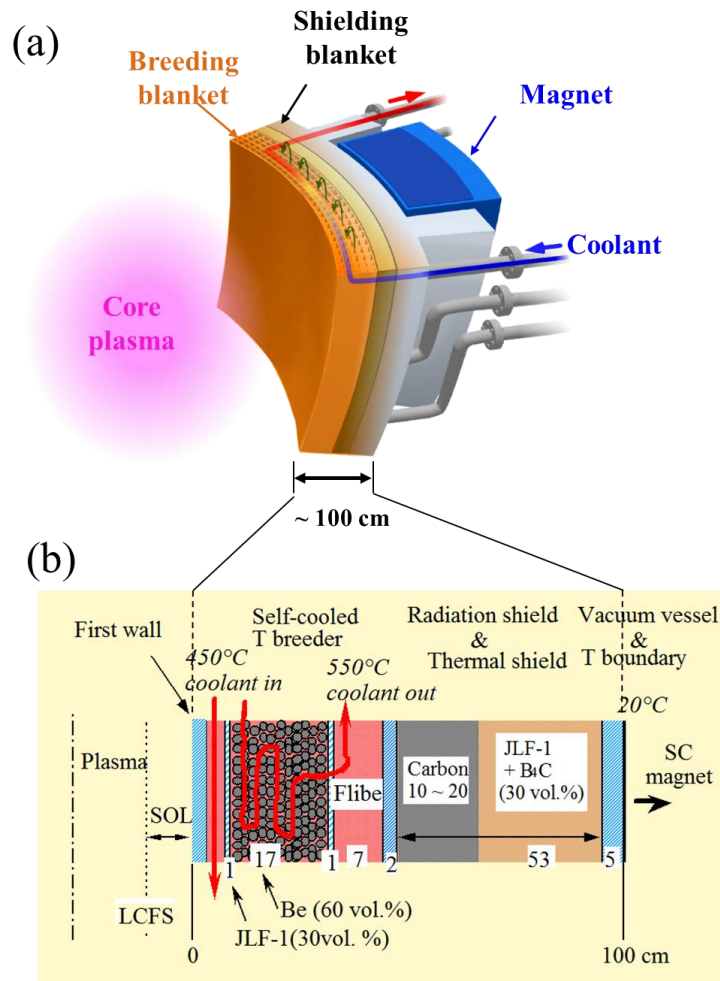


Figure 1.3 (a) A module of the FFHR2 outboard blanket and (b) a schematic diagram of the blanket structure [26].

Reduced activation ferritic steels (RAFSs) such as F82H are the candidate materials for the first wall of reactors, due to the following advantages: (1) reduced activation: after operation to 45 MWa/m^2 in FFHR and 100 years cooling, the surface dose rate of the RAFSs is less than $10 \text{ } \mu\text{Sv/h}$, which satisfies the shallow land disposal limits [27]; (2) swelling resistance: $1 \text{ vol.}/100\text{dpa}$ as compared with $1 \text{ vol.}/10\text{dpa}$ in stainless steels [28] and (3) relatively high thermal conductivity, which allows a relatively thick first wall design [29].

From the viewpoint of efficient heat exchange, the blanket operational temperature should be close to the maximum temperature at which the structural material can maintain its strength. For RAFSs, the operational temperature would be around $500 \text{ } ^\circ\text{C}$. Shown in Fig. 1.4 is the relation between stresses and the wall thickness [30]. The sum of thermal stress and stress arising from internal pressure has a minimum value at $\sim 5 \text{ mm}$, which is considered to be the optimum thickness in this design configuration. Table 1.1 shows some of the parameters for the breeding blanket concepts [31]. It can be found that in most of the recent reactor studies, including FFHR, the first wall is designed to be 5 mm or even less, although these concepts employ various first wall materials such as vanadium alloy (V-alloy) and silicon-carbide-fiber-reinforced silicon carbide composites (SiC_f/SiC).

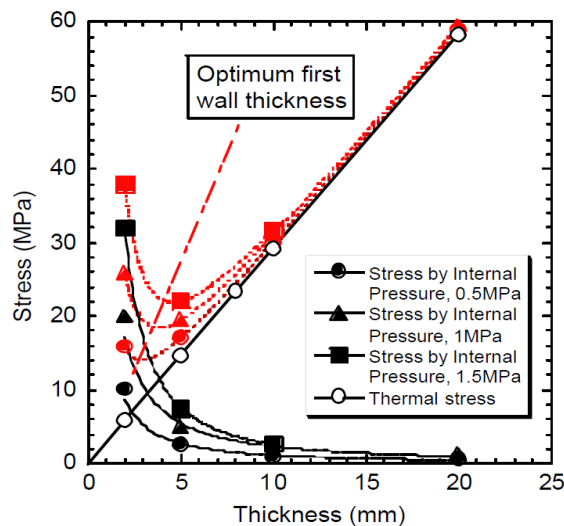


Figure 1.4 Stresses in the first wall as a function of thickness [30].

Table 1.1 Some of the breeding blanket concepts (re-edited from [31])

	He cooled pebble bed	Water cooled pebble bed	Water cooled Pb-17Li	Self-cooled FLiBe	Self-cooled Li	He cooled Li	He cooled pebble bed
Device	Tokamak DEMO	Tokamak DEMO	Tokamak DEMO	Helical FFHR-2	Tokamak	Tokamak LAR design	Tokamak
Tritium breeder	Li Ceramics	Li ₂ TiO ₃	Pb-17Li	FLiBe	Li	Li	Li ₄ SiO ₄
Structural material	ODS steel, RAFS	F82H, ODS RAFS	EUROFER RAFS	RAFS V-Alloy	V-Alloy	V-Alloy (W coating)	SiC _f /SiC
Fusion power (GW)	3.6	2.3	3.6	1		5.3	4.5
Neutron load (MW/m ²)	4.4 (max)	5.0 (max)	6.6 (max)	1.7 (ave)	10 (max)	11 (max)	3.5 (max)
Surface heat load (MW/m ²)	0.8 (max)	1.0 (max)	1.2 (max)	0.1 (ave)	2 (max)	2.73 (max)	0.6 (max)
FW thickness (mm)	5	3	4	5	4	1.5+1(W), tubing	3
FW temperature (°C)	630	~600	590	750	754	697	913
Coolant	He	H ₂ O	H ₂ O	FLiBe	Liq. Li	He	He
Pressure	8 Mpa	25 MPa	15.5 MPa	0.6 Mpa	0.5 MPa	15 MPa	8 MPa
Ref.	[32]	[33]	[32]	[30]	[34]	[35]	[36]

1.3. Hydrogen isotopes permeation issues

As shown in Fig. 1.3 (b), the first wall will be exposed to edge plasma at elevated temperatures on the one hand, and also it will be in contact with a liquid breeder or coolant, either one of which contains bred tritium on the other hand. One then predicts that the first

wall will be subjected to hydrogen isotopes penetration in the two opposite directions. From the edge plasma side, deuterium and tritium flow into the blanket by the mechanism referred to as PDP (for plasma-driven permeation), and from the blanket bred tritium flows into the plasma side by GDP (for gas-driven permeation), as shown in Fig.1.5.

It is important to note that (1) PDP necessitates an isotope separation capability in the tritium recovery loop of a reactor, which then complicates the entire fuel recycle system; and (2) GDP, acting as fueling, may cause an edge plasma density rise.

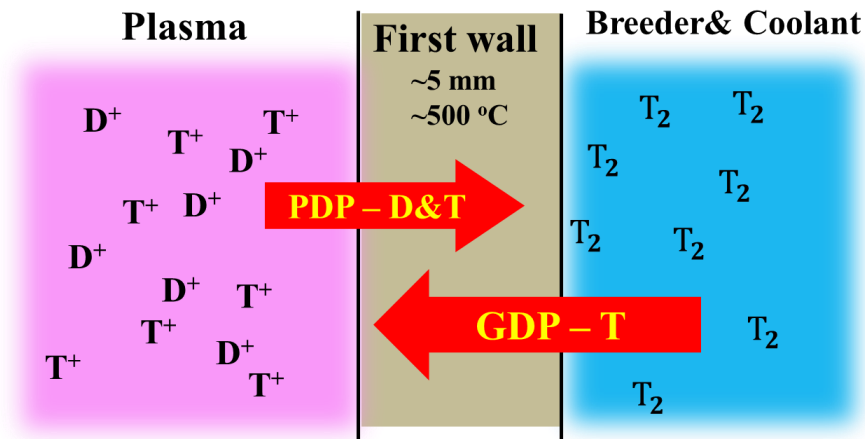


Figure 1.5 PDP and GDP of hydrogen isotopes through the first wall

The behavior of hydrogenic particles implantation-driven permeation through a membrane has been investigated by researchers for decades. Some permeation experiments were performed using ion gun facilities, in which case the ion energies were several to tens of keV and the ion fluxes were usually lower than $10^{15} \text{ cm}^{-2}\text{s}^{-1}$. Here such kind of permeation behavior is referred to as ion-driven permeation (IDP), to differentiate from plasma-driven permeation, which has relatively lower implantation energies. In those IDP experiments the membrane materials included pure iron, stainless steel, nickel, vanadium, tungsten and iron+coatings. Membrane thicknesses varied from 10 μm to 500 μm and target temperatures were kept between room temperature and 900 $^{\circ}\text{C}$, as summarized in Table 1.2.

Table 1.2 A summary of some of the IDP experiments.

Material	Sample Temperature (K)	Incident Flux (cm ⁻² s ⁻¹)	E _{ion} (eV)	Membrane Thickness (mm)	Permeation Flux (cm ⁻² s ⁻¹)	Ref.
SUS316L	670	5.70×10 ¹⁴	100-2000	0.05	8.55×10 ⁹ ~1.71×10 ¹⁰	[37]
Ni	300-1073	4.00×10 ¹⁴	30k	0.01	<3×10 ¹²	[38]
				0.02	<2×10 ¹²	
				0.05	<1×10 ¹²	
				0.1	<4×10 ¹¹	
Ni	373-1273	0.2-1.1×10 ¹⁵	1-2.5k	0.122 and 0.124	10 ¹⁰ ~<10 ¹³	[39]
Pure Fe	295-610	0.3-6×10 ¹³	750~3000	0.1	0-2×10 ¹²	[40]
Pd coating +Fe				10nm+0.1	No	
Fe+ Pd coating				0.1+10nm	0-9×10 ¹²	
Au coating +Fe				10nm+0.1	0~2×10 ¹²	
Fe	~400	10 ¹⁴ (100eV) 10 ¹⁵ (2000eV)	100-2000	0.1	<4×10 ¹³	[41]
W	598-660	4×10 ¹⁴ -1×10 ¹⁵	100-2000	0.025	<8×10 ¹⁰	[42]

Literature data show that the temperature dependence of permeation fluxes differed from material to material. For SS316L [37,43] and nickel [44,45], the permeation flux ratios would become larger as the temperature increased. However, conflict trends were reported for pure iron [39,40] and tungsten [42,46] in different papers, which may be resulted from different experimental conditions, e.g., ion implantation energies. The effects of incident energy were also investigated. For some materials, e.g., SS316L [38], nickel [39] and tungsten [39,40], permeation flux increased as the incident energy increased. However, it should be noted that the ion energy effect may be not the same if the permeation regime changes, which is

possible due to the variation of incident energy and sample temperature [47]. One example is that the ion energy dependence became not noticeable at very high energy range, e.g., several keV, or at high temperatures [37,39]. For most of these experiments, the permeation flux ratios were proportional to the incident fluxes [37,39-43].

These IDP experiments provide a large amount of data on hydrogen isotopes permeation through materials, which can be good references for researchers. Based on these data, several models are proposed to explain the permeation behavior, including implantation, diffusion and surface recombination, which will be introduced in detail in Chapter 2. However, it should be pointed out that the ion fluxes were too low and the incident energies were too high in these IDP experiments, making them not comparable with the PWI conditions for the first wall in a fusion reactor.

Generally, the edge plasma density in the scrape-off layer (to be referred to as SOL) of a magnetic fusion device is of the order of 10^{13} cm^{-3} and the cross-field diffusion coefficient is typically of the order of $10^3 \text{ cm}^2\text{s}^{-1}$. Assuming that the thickness of SOL is a few cm, the cross-field particle flux to the first wall may be estimated to be of the order of $10^{16} \text{ H cm}^{-2}\text{s}^{-1}$. A similar order estimate can be obtained from the cross-field transport scaling law observed in Alcator C-Mod [48]. From 1980s, researchers started to investigate plasma-driven permeation issues using low energy, high flux plasmas, which is more relevant to the reactor plasma-wall interaction (PWI) conditions. Those data as summarized in Table 1.3.

Membrane bias effects were investigated in some of these works. The permeation fluxes were found to decrease if the bias voltages were higher than 50 V or more [50,53,55,56], which suggests that the PDP flux ratio is not directly related to the ion implantation range, and the surface condition may play an important role. After long-time plasma bombardment, a variation of the steady stage permeation flux was measured under the same bias voltage [50,56]. This change was attributed to the modification of upstream surface composition, which decides the recombination coefficient. For nickel [54] and Kovar [56], the permeation flux ratios increased as the temperatures increased. But a transition point at 480K was found for SUS304, which was interpreted as a shift from diffusion limited-regime to

recombination-limited regime [51]. It must be noted that although RAFSs are the candidate first wall materials for fusion power reactors, *PDP data on RAFSs are quite limited in the existing database.*

Table 1.3 A summary of some of the PDP experiments.

Material	Sample Temperature (K)	Incident Flux ($\text{cm}^{-2}\text{s}^{-1}$)	E_{ion} (eV)	Membrane Thickness (mm)	Permeation Flux ($\text{cm}^{-2}\text{s}^{-1}$)	Ref.
SUS304	683	8.8×10^{16}	20		1.5×10^{15}	[49]
SUS304	673	6.8×10^{16}	20-40	0.25	3.2×10^{14}	[50]
			150		$\sim 2 \times 10^{13}$	
SUS304	$\sim 400-673$	$\text{Ne} < \sim 5 \times 10^{10} \text{ cm}^{-3}$	< 10	0.01	6.3×10^{14} (at 480K)	[51]
Ni	523	$\text{Ne} < \sim 5 \times 10^{10} \text{ cm}^{-3}$	< 10	0.02	$\sim 9 \times 10^{14}$	[52]
				0.05	$\sim 6 \times 10^{14}$	
				0.2	$\sim 2 \times 10^{13}$	
Ni & Va	1073	$\text{Ne} = \sim 5 \times 10^{10} \text{ cm}^{-3}$	few-250	0.1	$< 2 \times 10^{17}$	[53]
Ni	473-773	3×10^{16}	100	0.3	$< 5 \times 10^{13}$	[54]
Nb	983	3×10^{15} and $(5-10) \times 10^{16}$ hot atoms	few-200	0.3	$< 3.5 \times 10^{15}$	[55]
Kovar	773	$\sim 5.7 \times 10^{16}$	20	0.25	6.10×10^{13}	[56]
TiB ₂ +Kovar				0.015+0.25	1.50×10^{13}	
Nb and Nb/Pd	775-975	2.5×10^{16}	10~100	0.025 and 0.1	$< 6.25 \times 10^{15}$	[57]

As described at the beginning of this section, for those blankets employing liquid breeder to serve as a coolant as well (self-cooled breeder), the first wall is to be exposed to tritium bred in blankets, depending upon its dissociation pressure, which may result in GDP. Shown in Fig.1.6 are the equilibrium tritium partial pressures in lithium and lithium compounds at a temperature of 800 K [58]. For FLiBe, which is the candidate breeder for a FFHR reactor [30], the tritium dissociation pressure is $\sim 10^4$ Pa at a (T/M) concentration of ~ 0.1 ppm.

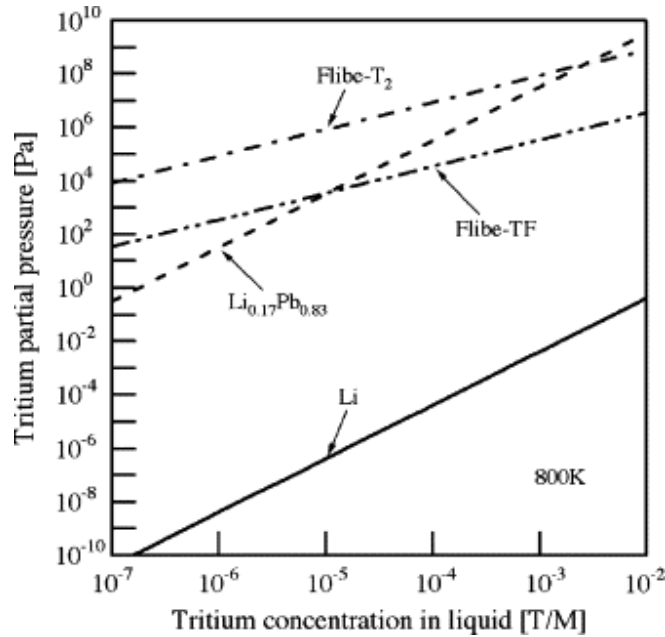


Figure 1.6 Equilibrium tritium partial pressures in lithium and lithium compounds [58].

Shown in Table 1.4 are some experimental data on gas-driven permeation for various metals. Compared with the database of PDP, the data on hydrogen isotopes GDP through metals are much more comprehensive and updated. Hydrogen transport parameters in several kinds of RAFSs and vanadium alloys are also available. Those GDP experiments were performed with a driving pressure of 10^2 - 10^5 Pa at a temperature of 322-1073 K. Some specific aspects such as trapping [59] and coating [63] were also investigated. In general, studies of RAFSs report relatively consistent transport properties of hydrogen isotopes.

However, due to the limitation of GDP setups, the surface recombination process is difficult to address in these studies.

Table 1.4 A summary of some of the GDP experiments.

Material	Thickness	Gas	Pressure	Temperature	E_p	E_D	E_s	Ref.
	mm		Pa	K	eV	eV	eV	
F82H	0.5-0.8	D ₂	$5 \times 10^2 - 10^5$	373-743	0.42	0.14	0.28	[59]
F82H	0.4	H ₂	$10^3 - 10^5$	373-723	0.41	0.15	0.27	[60]
F82H	1	D ₂	$10^2 - 10^3$	573-873	0.50*	0.12	0.38	[61]
F82H(oxidized)					0.42*	0.08	0.34	
F82H	0.85	T ₂	$8 \times 10^2 - 5.3 \times 10^3$	490-1000	0.42	0.08	0.34	[62]
		D ₂			0.43	0.083	0.35	
F82H	1	D ₂	$10^2 - 10^3$	573-873	0.46	0.081	0.37	[63]
		H ₂			0.43	0.083	0.34	
Batman	0.5-0.8	D ₂	$5 \times 10^2 - 10^5$	373-743	0.43	0.16	0.26	[59]
MANET II	0.5	D ₂	$3 - 10^5$	633-743	0.44	0.14	0.28	[64]
Commercial MANET	1 or 1.59	H ₂	$2.7 \times 10^2 - 10^5$	523-873	0.45	0.16	0.28	[65]
Commercial 316L			$1.33 \times 10^2 - 10^5$		0.66	0.47	0.19	
Fe	0.5	H ₂	$2.8 \times 10^3 - 10^5$	342-619	0.35	0.07	0.28*	[66]
Fe	1.33	H ₂	$4.3 \times 10^2 - 6.2 \times 10^4$	322-779	0.37	0.07	0.30*	[67]
		D ₂			0.38	0.08	0.30*	
Fe	0.2-0.4	H ₂	$10^4 - 10^5$	473-1073	0.35	0.11	0.24	[68]
Ni					0.57	0.46	0.11	
VCr6Ti5	1	H ₂	$10^2 - 10^3$	423-1073	0.44	0.17	0.25	[69]

* Estimated value from diffusion and solution coefficients

In Table 1.4, the terms E_P and E_D mean the activation energy for permeation and diffusion, respectively. E_S is the heat of solution. The detailed physical meaning of them will be explained in Chapter 2. Generally speaking, small activation energy indicates a relatively small temperature dependence of the coefficients, which can explain the different GDP behavior of RAFSs and stainless steel.

In summary, although the parameters such as permeability, diffusivity and solubility have been measured for some of the RAFSs [59-65], significant error can be made in predicting hydrogen isotope permeation flux through the first wall. Literature data on hydrogen transport parameters for RAFSs are limited because all these data are taken only from GDP experiments and the surface recombination process under plasma exposure is not sufficiently investigated. Some of the PDP experiments were run more than 20 years ago and the researchers' estimations on the edge plasma parameters and operation temperatures of the first wall were not quite accurate. From the viewpoint of fusion engineering, most target materials in those experiments cannot be used as structural material in a fusion reactor. More efforts are needed to establish the database of hydrogen isotopes PDP through RAFSs.

1.4. Objectives of this work

Evaluation of hydrogen isotopes permeation through the first wall is extremely important to the fusion system design work. This PhD thesis research aims (1) to understand the physical mechanisms driving hydrogen isotopes permeation processes; (2) to demonstrate experimentally hydrogen transport phenomena that are predicted for the first wall of a fusion power reactor and (3) to establish a database on hydrogen transport parameters for designing fusion power reactors.

1.5. Outline of the thesis

The thesis is arranged as follows: after this introduction chapter, some theories and models on hydrogen isotopes transport through solids will be briefly reviewed in Chapter 2. In Chapter 3, studies on hydrogen gas- and plasma-driven permeation through a reduced activation steel alloy F82H in a laboratory-scale steady-state plasma device: VEHICLE-1 will be presented. The experimental results of PDP through F82H in a medium size spherical tokamak QUEST will be shown in Chapter 4. Chapter 5 includes the hydrogen (H) bi-directional permeation experiments and theoretical calculations. Studies on multiple hydrogen isotopes (D/T) bi-directional permeation through the first walls of reactors will be presented in Chapter 6, followed by a summary of the whole thesis.

Reference

- [1] J. A. Wesson, *Tokamaks*, Clarendon Press, Oxford, 3rd edition, 2004.
- [2] M. Kikuchi, *Frontiers in fusion research*, Springer-Verlag, London, 2011.
- [3] K. Miyamoto, *Plasma physics and controlled nuclear fusion*, Springer-Verlag, Berlin, 2005.
- [4] J. D. Lawson, *Some criteria for a power producing thermonuclear reactor*. Proc. Phys. Soc. B 70 (1957) 6.
- [5] <http://www.efda.org/jet/>.
- [6] <http://www-jt60.naka.jaea.go.jp/>.
- [7] <http://www.lhd.nifs.ac.jp/>.
- [8] <https://fusion.gat.com/global/DIII-D>.
- [9] <http://www.ipp.mpg.de/16195/asdex>.
- [10] <http://english.hf.cas.cn/ic/ip/east/>.
- [11] G.S. Lee et al., *Design and construction of the KSTAR tokamak*, Nuclear Fusion 41 (2001)1515.
- [12] K. Hanada et al., *Steady-State Operation Scenario and the First Experimental Result on QUEST*, Plasma Fusion Research 5 (2010) S1007.
- [13] <http://www.iter.org>.
- [14] Y. Shimomura, *ITER towards the construction*, Fusion Engineering and Design 74 (2005) 9.

- [15] K. Tobita et al., *Compact DEMO, SlimCS: design progress and issues*, Nuclear Fusion 49 (2009) 075029.
- [16] D. Maisonnier et al., *DEMO and fusion power plant conceptual studies in Europe*, Fusion Engineering and Design 81 (2006) 1123.
- [17] F. Najmabadi et al., *The ARIES-AT advanced tokamak, Advanced technology fusion power plant*, Fusion Engineering and Design 80 (2006) 3.
- [18] A. Sagara et al., *Conceptual design activities and key issues on LHD-type reactor FFHR*, Fusion Engineering and Design 81 (2006) 2703.
- [19] Y. Wang et al., *Overview of fusion energy science research in China*, Paper presented at the 16th International Conference on Fusion Reactor Materials, Beijing, China, Oct. 20th -26th, 2013.
- [20] Y. K. M. Peng et al., *Fusion Nuclear Science Facility (FNSF) Before Upgrade to Component Test Facility (CTF)*, Fusion Science and Technology 60 (2011) 441.
- [21] S. Pfalzner, *An introduction to inertial confinement fusion*, Taylor & Francis, New York, 2006.
- [22] <https://lasers.llnl.gov>.
- [23] O. A. Hurricane et al., *Fuel gain exceeding unity in an inertially confined fusion implosion*, Nature 506 (2014) 343.
- [24] T. Tanabe, *Tritium issues to be solved for establishment of a fusion reactor*, Fusion Engineering and Design 87 (2012) 722.
- [25] D. Fasel et al., *Availability of lithium in the context of future D-T fusion reactors*, Fusion Engineering and Design 75–79 (2005) 1163.
- [26] NIFS research report, NIFS-MEMO-64, 2013, in Japanese.

- [27] A. Sagara, et al., *Materials design and related R&D issues for the force-free helical reactor (FFHR)*, Journal of Nuclear Materials 258–263 (1998) 2079.
- [28] N. Baluc et al., *On the potentiality of using ferritic/martensitic steels as structural materials for fusion reactors*, Nuclear Fusion 44 (2004) 56.
- [29] A. Hishinuma, et al., *Current status and future R&D for the reduced-activation ferritic/martensitic steels*, Journal of Nuclear Materials 258–263 (1998) 193.
- [30] A. Sagara, et al., *Studies on FLiBe blanket designs in helical reactor FFHR*, Fusion Technology 39 (2001) 753.
- [31] Ueda et al., *PSI issues at plasma facing surfaces of blankets in fusion reactors*, Journal of Nuclear Materials 313–316 (2003) 32.
- [32] L. Giancarli et al., *Candidate blanket concepts for a European fusion power plant study*, Fusion Engineering and Design 49&50 (2000) 445.
- [33] S.Konishi et al., *DEMO plant design beyond ITER*, Fusion Engineering and Design 63-64 (2002) 11.
- [34] Y. Gohar et al., *High power density self-cooled lithium–vanadium blanket*, Fusion Engineering and Design 49–50 (2000) 551.
- [35] C.P.C. Wong et al. *A helium-cooled blanket design of the low aspect ratio*, Fusion Engineering and Design 48 (2000) 389.
- [36] L.V. Boccaccini et al., *Advanced helium cooled pebble bed blanket with SiC_f/SiC as structural material*, Fusion Engineering and Design 49–50 (2000) 491.
- [37] H. Nakamura et al., *Implantation driven permeation behavior of deuterium through stainless steel type 316L*, Journal of Nuclear Materials 258-263 (1998) 1050.

- [38] T. Tanabe et al., *Hydrogen-ion-driven permeation at high temperatures*, Journal of Nuclear Materials 128 & 129 (1984) 641.
- [39] T. Nagasaki et al., *Simultaneous ion and gas driven permeation of deuterium through nickel*, Journal of Nuclear Materials 151(1988) 189.
- [40] W. M. Shu et al., *Coating effect on plasma-driven permeation of hydrogen in iron*, Fusion Engineering and Design 28 (1995) 131.
- [41] W. M. Shu, *Ion-driven permeation of deuterium in Fe-Ti alloys*, Journal of Alloys and Compounds 196 (1993) 213.
- [42] H. Nakanura et al., *Tritium permeation behavior implanted into pure tungsten and its isotope effect*, Journal of Nuclear Materials 297 (2001) 285.
- [43] B.L. Doyle, D.K. Brice, *The influence of displacement damage on deuterium permeation in 316 stainless steel*, Journal of Nuclear Materials 145-147 (1987) 288.
- [44] K. Yamaguchi et al., *Simultaneous ion- and gas-driven permeation of hydrogen isotopes through first wall material*, Fusion Engineering and Design 10 (1989) 337.
- [45] T. Tanabe et al., *Hydrogen-ion-driven permeation at high temperatures*, Journal of Nuclear Materials 128 & 129 (1984) 641.
- [46] H.T. Lee et al., *Ion-driven permeation of deuterium through tungsten under simultaneous helium and deuterium irradiation*, Journal of Nuclear Materials 415 (2011) S696.
- [47] B.L. Doyle, *A simple theory for maximum H inventory and release: A new transport parameter*, Journal of Nuclear Materials 111/112 (1982) 628.
- [48] B. LaBombard et al., *Cross-field plasma transport and main-chamber recycling in diverted plasmas on Alcator C-Mod*, Nuclear Fusion 40 (2000) 2041.

- [49] R. A. Kerst and W.A. Swansiger, *Plasma driven permeation of tritium in fusion reactors*, J. Journal of Nuclear Materials 122&123, (1984) 1499.
- [50] R. A. Causey et al., *The effect of surface composition on plasma driven permeation of deuterium through 304 stainless steel*, Journal of Nuclear Materials 122&123 (1984) 1547.
- [51] M. Takizawa et al., *Surface condition effects on plasma driven permeation*, Journal of Nuclear Materials 248 (1997) 15.
- [52] M. Takizawa et al., *Estimation of permeation probability in plasma driven permeation*, Fusion Engineering and Design 39–40 (1998) 923.
- [53] A. I. Livshits et al., *Plasma driven superpermeation of hydrogen through group Va Metals*, Journal of Applied Physics 84 (1998) 2558.
- [54] R.A. Causey et al., *Plasma-driven permeation of deuterium in nickel*, Journal of Nuclear Materials 145-147 (1987) 284.
- [55] A. Busnyuk et al., *Membrane bias effects on plasma-driven permeation of hydrogen through niobium membrane*, Journal of Nuclear Materials 290–293 (2001) 57.
- [56] R. A. Kerst et al., *Comparison of plasma and gas driven permeation of deuterium through titanium diboride*, Journal of Nuclear Materials 135 (1985) 77.
- [57] A.A. Skovoroda et al., *Plasma-driven superpermeation of hydrogen through Nb membranes: bulk effects*, Journal of Nuclear Materials 306 (2002) 232.
- [58] S. Fukada et al., *Tritium recovery system for Li–Pb loop of inertial fusion reactor*, Fusion Engineering and Design 83 (2008) 747.
- [59] E. Serra et al., *Influence of traps on the deuterium behaviour in the low activation martensitic steels F82H and Batman*, Journal of Nuclear Materials 245 (1997) 108.

- [60] E. Serra et al., *Hydrogen behaviour in aged low activation martensitic steel F82H for fusion reactor applications*, Materials Science and Technology 14 (1998) 573.
- [61] A Pisarev et al., *Surface effects in diffusion measurements: deuterium permeation through Martensitic steel*, Physica Scripta T94 (2001) 121.
- [62] E. Dolinsky et al., *Permeation of deuterium and tritium through the martensitic steel F82H*, Journal of Nuclear Materials 307-311 (2002) 1484.
- [63] T.V. Kulsartov et al., *Investigation of hydrogen isotope permeation through F82H steel with and without a ceramic coating of $\text{Cr}_2\text{O}_3\text{-SiO}_2$ including CrPO_4 (out-of-pile tests)*, Fusion Engineering and Design 81 (2006) 701.
- [64] E. Serra et al., *Influence of the surface conditions on permeation in the deuterium-MANET system*, Journal of Nuclear Materials. 240 (1997) 215.
- [65] K.S. Forcey et al., *Hydrogen transport and solubility in 316L and 1.4914 steels for fusion reactor applications*, Journal of Nuclear Materials 160 (1988) 117.
- [66] R. F. Miller et al., *Permeation of hydrogen through alpha iron*, Metallurgical Transactions A, 6A (1975) 117.
- [67] N. R. Quick et al., *Hydrogen and deuterium in iron, 49–506°C*, Acta Metallurgica 26 (1978) 903.
- [68] Y. Yamanishi et al., *Hydrogen permeation and diffusion through pure Fe, pure Ni and Fe-Ni alloys*, Transactions of the Japan Institute of Metals 24 (1983) 49.
- [69] O.G. Romanenko et al., *Hydrogen gas driven permeation through vanadium alloy VCr6Ti5*, Journal of Nuclear Materials 233-237 (1996) 376.

Chapter 2

Theories on hydrogen isotopes transport through solids

In Chapter 1 the phenomena of hydrogen isotopes plasma- and gas-driven permeation through the first wall of a magnetic fusion reactor have been introduced. The databases of gas-, ion- and plasma-driven permeation experiments have been briefly reviewed as well. To understand those data taken in wide ranges of temperature, hydrogen gas pressure and implantation flux, and also to set the scene for the following research report chapters, this chapter reviews some of the physical mechanisms involved in the interaction of hydrogenic particles with solids, their diffusion and trapping in the solids, and the surface recombination allowing them to be released. In the latter part of the chapter, the steady state permeation models and hydrogen isotope effects are shown.

2.1. Entering and release of hydrogen isotopes in solids

2.1.1. Reflection and implantation

When energetic hydrogen atoms or ions impinge on the first walls, a fraction of them are reflected in a time of $\leq 10^{-12}$ s [1]. The particle reflection coefficient R_N is defined as the number of all backscattered particles N divided by the number of incident particles N_0 . As shown in Fig. 2.1, the particles backscattered have distributions in energy E , exit polar angle β , exit azimuthal angle φ and charge state q_i , depending on the incident energy E_0 and angle α , which may be described by [1,2]:

$$f(E_0, \alpha; E, \beta, \varphi, q_i) \quad (2.1)$$

Then R_N can be obtained by integrating the distributions:

$$R_N(E_0, \alpha) = \sum_i \int_0^{E_0} dE \int_0^{\pi/2} d\beta \int_0^{2\pi} d\varphi f(E_0, \alpha; E, \beta, \varphi, q_i) \sin \beta \quad (2.2)$$

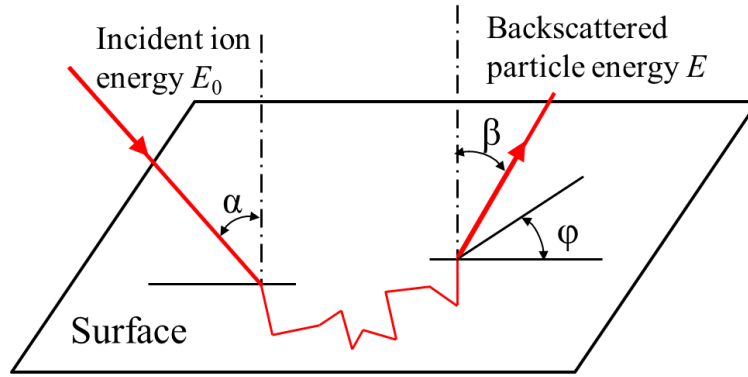


Figure 2.1 Backscattering of an ion with incident energy E_0 from the surface of a solid (re-plot from [1].)

The particles which are not backscattered are implanted into the walls. These particles will be slowed down by transferring energy to the target electrons (electronic stopping), or by interaction with the target atom core (nuclear stopping). The mean range of implantation ions may be calculated by [3]:

$$\bar{d} = \frac{1}{n} \int_0^{E_0} \frac{dE}{S(E)} \quad (2.3)$$

where E_0 is the incident energy, n is the particle number and $S(E)$ is the total stopping cross section from electronic and nuclear stopping.

Based on the binary collision approximation (BCA) [4], several Monte Carlo simulation codes have been developed for plasma-wall interaction applications, for example, TRIM [5], ACAT [6] and EDDY [7]. Shown in Fig.2.2 are the calculation results for reflection coefficient of hydrogenic particles on pure iron surface by these codes. The calculated reflection coefficient decreases as an increase of implantation energy when E_0 is larger than 10 eV. Figure 2.3 shows one calculation on hydrogen implantation profile in iron by SRIM2008 [8] and EDDY. In general, the calculation results given by these codes are in good consistency.

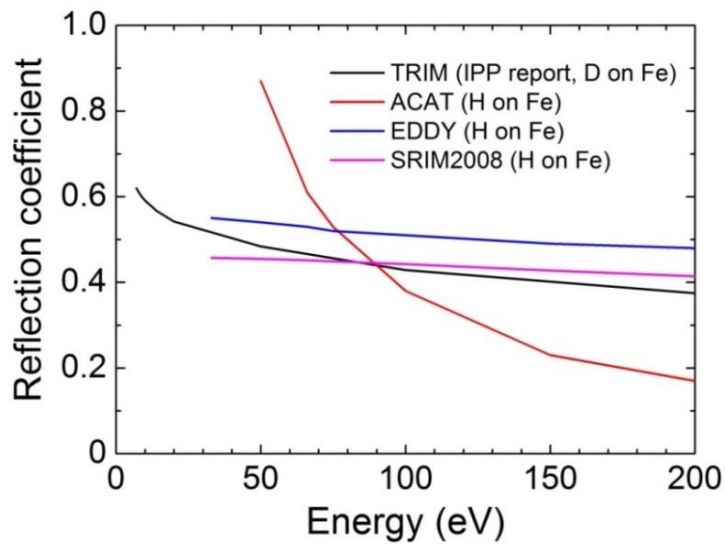


Figure 2.2 Particle reflection coefficient of hydrogen on iron estimated by the Monte Carlo codes. For the IPP report, see [5].

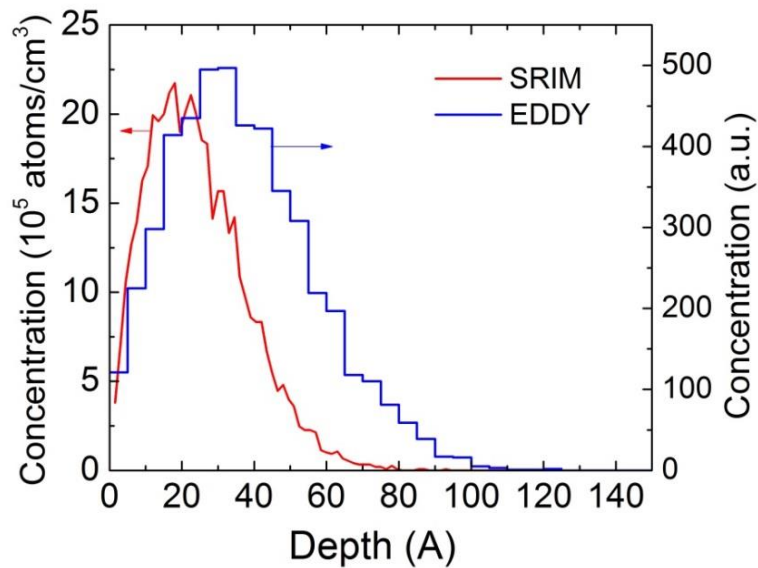


Figure 2.3 Calculated hydrogen implantation profile in iron by SRIM2008 and EDDY codes. The implantation energy is 100 eV.

2.1.2. Solution

For hydrogen gas and solids in thermodynamic equilibrium, the hydrogen solubility in metal is proportional to the square root of the partial pressure of the gas (Sieverts' law [9]) and the bulk concentration C can be given by:

$$C = S \cdot \sqrt{p}, \quad (2.4)$$

with S donating the solubility expressed by [3]:

$$S = S_0 \exp\left(-\frac{U_s}{kT}\right), \quad (2.5)$$

where U_s is the enthalpy of solution, which is positive for endothermal hydrogen-solid system and negative for exothermal case.

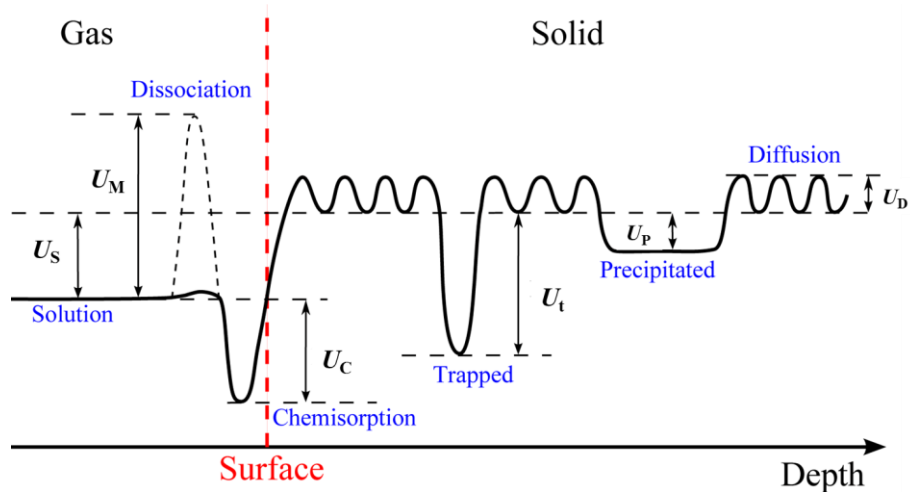


Figure 2.4 Schematic energy diagram for hydrogen in metals. (Re-plot from [3]).

U_s , U_C , U_t and U_P are the enthalpies of solution, chemisorption, trapping and precipitation. U_M is dissociation energy and U_D is the activation energy for diffusion.

2.1.3. Diffusion and trapping

The dissolved hydrogen atoms may migrate in the host lattice, or be trapped by defects and impurities in the lattice. Figure 2.4 shows a schematic energy diagram for hydrogen in metals. It can be seen that the trapping sites expose a higher binding energy than regular solution sites. The behavior of one-dimensional hydrogen transport through a solid with trapping sites can be described by the following equations [10]:

$$\frac{\partial C(x,t)}{\partial t} = D(T) \frac{\partial^2 C(x,t)}{\partial x^2} - \frac{\partial C_t(x,t)}{\partial t} + G(x,t) \quad (2.6)$$

$$\frac{\partial C_t(x,t)}{\partial t} = D(T) \frac{C(x,t)C_t^e(x,t)}{\lambda^2} - C_t(x,t)\nu_0 \exp(-U_t / kT) \quad (2.7)$$

$$C_t^e(x,t) = C_t^0(x) - C_t(x,t) \quad (2.8)$$

where $C(x,t)$ and $C_t(x,t)$ are the concentrations of mobile and trapped atoms as a function of position x and time t ; D is the diffusion coefficient; T is the temperature; $G(x,t)$ is the hydrogen implantation profile; $C_t^0(x)$ and $C_t^e(x)$ are the concentrations of intrinsic and empty trapping sites, respectively; λ is the mean distance between trapping sites; ν_0 is the jumping frequency; k is Boltzman's constant and U_t is the de-trapping energy. Equation (2.6) indicates that trapping sites introduced by neutron or energetic particle bombardment will only affect the initial transient permeation behavior.

The diffusion coefficient D can be derived from the "random walk" model, in which case D is given as [14]:

$$D = D_0 \exp\left(-\frac{U_D}{kT}\right) \quad (2.9)$$

where D_0 is the pre-exponential containing the jumping frequency and lattice structure information, and U_D is the activation energy for diffusion.

2.1.4. Surface recombination

Hydrogen is released from the surface of a solid via the recombination of dissolved atoms to a hydrogen molecule. The recombination flux (i.e. re-emission flux) J_- is proportional to the square of the bulk concentration C at the surface [3]:

$$J_- = K_r \cdot C^2 \quad (2.10)$$

with the recombination coefficient K_r .

Based on the idealized energy diagram shown in Fig 2.4, several models for estimating K_r have been proposed (see Ref. [11], [12] and [13]). Baskes [11] gave a simplified method to calculate the recombination coefficient and the K_r is given as:

$$K_r = \frac{K_0}{\sqrt{T}} \exp\left(-\frac{U_K}{kT}\right) \quad (2.11)$$

where U_K is the activation energy of recombination and $U_K = U_D + U_S$ when $U_D + U_S \geq 0$; and $U_K = 2U_S$ when $U_D + U_S < 0$. K_0 is a pre-factor which is related to the solubility, diffusivity and surface sticking coefficient:

2.2. Steady state permeation models

The steady state permeation flux J_+ controlled by diffusion is generally given by Fick's first law [14]:

$$J_+ = -D \frac{\partial C}{\partial x} \quad (2.12)$$

For gas-driven permeation, the steady state GDP flux through a thin membrane can be obtained by combining Eq. (2.4) and (2.12):

$$J_+ = DS \frac{\sqrt{P_{up}} - \sqrt{P_{down}}}{L} = \Phi \frac{\sqrt{P_{up}} - \sqrt{P_{down}}}{L} \quad (2.13)$$

where L is the membrane thickness, P_{up} and P_{down} are the hydrogen pressures at the upstream side and the downstream side, respectively. Note here that usually $P_{up} \gg P_{down}$ holds. Here $\Phi = DS$ is usually defined as the permeability of hydrogen through a solid.

For plasma-driven permeation, three regimes are considered [15,16]: (1) diffusion-limited release of hydrogen from both the upstream and downstream surfaces (to be referred to as the DD regime); (2) recombination-limited release of hydrogen from the upstream surface and diffusion-limited release of hydrogen from the downstream surface (to be referred to as RD regime) and (3) recombination-limited release of hydrogen for both surfaces (to be referred to as RR regime).

The rate controlling process can be characterized by the dimensionless parameter W [15]:

$$W = \frac{d}{D} (J_0 K_r)^{1/2}. \quad (2.14)$$

Shown in Fig. 2.5 (a) is the normalized hydrogen concentrations as a function of W , assuming the ratio of the implantation range and the membrane thickness $\alpha = d/L = 10^{-6}$, and the surface conditions for the front surface and back surface are the same ($\beta = K_r/K_l = 1$). C_R , C_0 and C_L are the hydrogen concentrations at the implantation range, front surface and back surface, respectively.

The overall hydrogen transport is controlled by the slowest process and the parameter W may be regarded as a competition between diffusion and recombination. For $W > 1$, which is possible when hydrogen is deeply implanted and diffusion is slow compared with surface recombination, the concentration is peaked at the implantation range d ($C_R > C_0$, C_L , as shown in Fig.2.5(b)). This regime is the DD-regime. For $\beta\alpha < W < 1$, $C_R \approx C_0$ and $C_L \approx 0$, indicating recombination-limited behavior at the upstream surface and diffusion-limited

behavior at the downstream surface. If $W < \beta\alpha$, the hydrogen concentration is uniform throughout the membrane and PDP is in the RR regime.

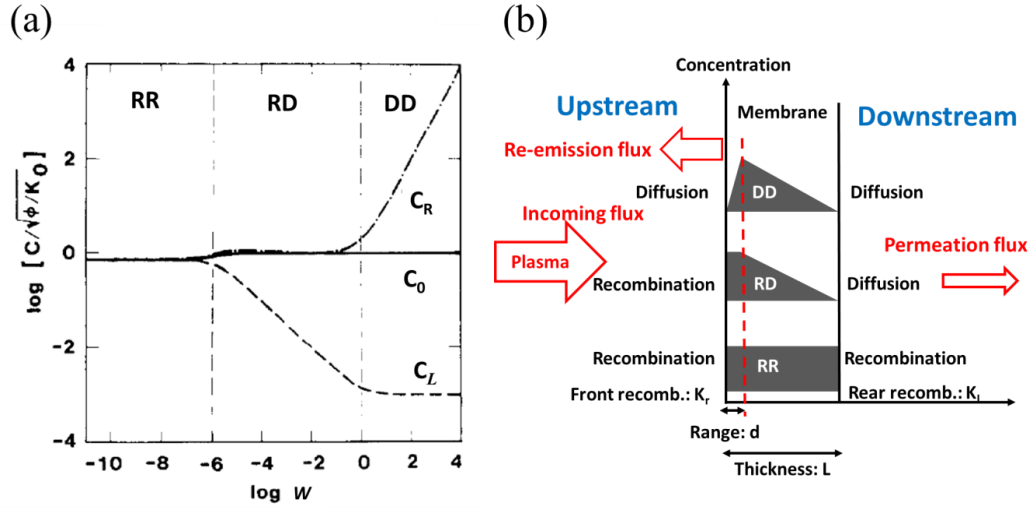


Figure 2.5 (a) normalized hydrogen concentrations as a function of W (re-edit from [15]) and (b) hydrogen concentration profiles for the three regimes.

The steady state hydrogen plasma-driven permeation flux J_+ is given by the following formulae:

$$J_+ = \frac{d}{L} J_0 \quad (\text{for DD regime}) \quad (2.15)$$

$$J_+ = \frac{D}{L} \sqrt{\frac{J_0}{K_r}} \quad (\text{for RD regime}) \quad (2.16)$$

$$J_+ = \frac{K_l}{K_r + K_l} J_0 \quad (\text{for RR regime}) \quad (2.17)$$

It should be pointed out that:

- (1) In the DD regime, J_+ is not related to the surface recombination coefficients;
- (2) In the RD regime, J_+ is only affected by the upstream surface recombination coefficient, but not the downstream surface condition. Meanwhile, only in this regime J_+ is proportional to the square root of the implantation flux J_0 .
- (3) In both DD and RD regimes, J_+ is inversely proportional to the membrane thickness L . In contrast, J_+ is not affected by L in RR regime.

2.3. Isotope effects

For D-T fusion reactor studies, isotope effects must be taken into account because both deuterium and tritium are the fuels. Isotope effects on hydrogen transport can be divided into two classes [17], i.e. intrinsic effects and synergistic effects. The former class is related to the differences in the transport properties of each of the individual isotopes, for example, the isotope dependence of the diffusivity, the heat of transport and trap strength. The latter class is due to the competition of the various isotopes for traps and the coupling of isotopes through the process of surface recombination.

Taking into account the isotope effects, the one-dimensional hydrogen transport process described in (2.6)-(2.8) can be modified as [18]:

$$\frac{\partial C^j(x,t)}{\partial t} = D_j(T) \frac{\partial^2 C^j(x,t)}{\partial x^2} - \sum_i \frac{\partial C_t^{ij}(x,t)}{\partial t} + G_j(x,t) \quad (2.18)$$

$$\frac{\partial C_t^{ij}(x,t)}{\partial t} = D_j(T) \frac{C^j(x,t) C_t^{ei}(x,t)}{\lambda^2} - C_t^{ij}(x,t) \nu_0 \exp(-U_t^i / kT) \quad (2.19)$$

$$C_t^{ei}(x,t) = C_t^{0i}(x) - \sum_j C_t^{ij}(x,t), \quad (2.20)$$

where $C^j(x,t)$ and $C_t^{ij}(x,t)$ are the concentrations of mobile j^{th} species and trapped j^{th} species in the i^{th} trapping site; D_j is the diffusion coefficient of the j^{th} species; T is the temperature; $G_j(x,t)$ is the hydrogen implantation profile of the j^{th} species; U_t^i is the de-trapping energy of the i^{th} trapping site; $C_t^{0i}(x)$ and $C_t^{ei}(x)$ are the concentrations of intrinsic and empty i^{th} trapping sites, respectively.

The isotope effects have been included into some of the hydrogen transport codes like TMAP [18] and DIFFUSE [19], the latter of which has been utilized to analyze the bi-directional permeation behavior under some of the reactor-relevant conditions in this thesis work. More details are presented in Chapter 6.

2.4. Summary

In this chapter, the physical mechanisms involved in the hydrogen permeation process are briefly introduced. When hydrogenic particles impinge on solids, a fraction of them will be immediately reflected. For those hydrogenic atoms implanted into the solid, they will either transport in the lattice of solids, or be trapped by impurities and defects. Finally, the mobile atoms will be released as molecules by surface recombination.

The theories on hydrogen isotopes transport through solids have been well developed and some hydrogen transport case can be analytically or numerically solved. This thesis work tries to utilize these theories to explain the observations in various permeation experiments. Using the equations describing the transient and steady state hydrogen transport behavior, the permeation properties of various materials can be evaluated and the transport parameters such as Sieverts' constant, diffusion and recombination coefficients can be measured.

The steady state PDP models show the relation between the implantation flux J_0 and the permeation flux J_+ in different regimes, which indicate the potential methods to suppress J_+ . Taking the RD regime as an example, one would consider either increasing the front surface coefficient or increasing the membrane thickness to reduce J_+ for the first wall made by a certain material. However, as pointed out in Chapter 1, thermo-mechanical stresses would not allow us to consider thick first wall designs. This leads us to the use of permeation barrier and the modification of the plasma-facing surfaces, which are presented in detail in Section 3.6 of Chapter 3.

Reference

- [1] B. Behrigh and W. Eckstein, *Physics of plasma-wall interaction in controlled fusion devices*, Plenum Press, New York, 1986, p. 413–438.
- [2] R.A. Langley et al., *Data compendium for plasma-surface interactions*, Nuclear Fusion 24 (1984) S9.
- [3] Möller and J. Roth, *Physics of Plasma-Wall Interaction in Controlled Fusion Devices*, Plenum Press, New York, 1986, p. 439–494.
- [4] M.T. Robinson and I. M. Torrens, *Computer simulation of atomic-displacement cascades in solids in the binary-collision approximation*, Physical Review, B9 (1974) 5008.
- [5] W. Eckstein, IPP-Report, IPP 9/132, 2002.
- [6] Y. Yamamura and Y. Mizuno, *Low-energy sputterings with the Monte Carlo program ACAT*, IIPJ-AM-40, Institute of Plasma Physics, Nagoya University, 1985.
- [7] J. Kawata and K. Ohya, *Ion backscattering and sputtering of plasma-irradiated carbon and tungsten surfaces in an oblique magnetic field*, Japanese Journal of Applied Physics, 34 (1995) 6237.
- [8] J. F. Ziegler et al., *SRIM – The stopping and range of ions in matter (2010)*, Nuclear Instruments and Methods in Physics Research Section B, 268 (2010) 1818.
- [9] C.K. Gupta, *Chemical metallurgy: principles and practice*, Wiley-VCH, Weinheim, 2003.
- [10] K. L. Wilson and M. I. Baskes, *Deuterium trapping in irradiated 316 stainless steel*, Journal of Nuclear Materials 76 & 77 (1978) 291.
- [11] M.I. Baskes, *A calculation of the surface recombination rate constant for hydrogen isotopes on metals*, Journal of Nuclear Materials 92 (1980) 318.

- [12] M. A. Pick and K. Sonnenberg, *A model for atomic hydrogen-metal interactions - application to recycling, recombination and permeation*, Journal of Nuclear Materials 131 (1985) 208.
- [13] P. M. Richards, *Surface-limited hydrogen release and uptake in metals*, Journal of Nuclear Materials 152 (1988) 246.
- [14] J. Crank, *The Mathematics of Diffusion*, 2nd edition, Clarendon Press, Oxford, London, 1975.
- [15] B. L. Doyle, *A simple theory for maximum h inventory and release: A new transport parameter*, Journal of Nuclear Materials 111&112 (1982) 628.
- [16] D. K. Brice and B.L. Doyle, *Steady state hydrogen transport in solids exposed to fusion reactor plasmas: part I: Theory*, Journal of Nuclear Materials 120 (1984) 230.
- [17] D. K. Brice, *Steady state hydrogen transport in solids exposed to fusion reactor plasmas, part III: Isotope effects*, Journal of Nuclear Materials 122&123 (1984) 1531.
- [18] G.R. Longhurst, *TMAP7: tritium migration analysis program, user manual*, Idaho National Laboratory, INEEL/EXT-04-02352, 2004.
- [19] M. I. Baskes, *DIFFUSE83*, Sandia Report SAND83-8231.

Chapter 3

Hydrogen gas- and plasma-driven permeation through a reduced activation steel alloy F82H

Gas- and plasma-driven permeation through a reduced activation steel alloy: F82H has been systematically investigated using a steady state laboratory-scale plasma device: VEHICLE-1 [1]. Hydrogen transport parameters have been measured from both GDP and PDP for F82H. The surface condition effects on plasma-driven permeation have been investigated as well. Based on the results, evaluation of hydrogen isotopes permeation and inventory in the first wall would be possible for reactor design studies.

3.1. VEHICLE-1 linear plasma facility and the permeation experimental setup

Figure 3.1 shows (a) a picture and (b) a schematic diagram of the linear plasma facility: VEHICLE-1 (the Vertical and Horizontal positions Interchangeable test stand for Components and Liquids for fusion Experiments) [1]. The VEHICLE-1 facility employs a 1 kW 2.45 GHz electrical cyclotron resonance (ECR) plasma source which can generate steady state plasmas. These plasmas are magnetized at around 300 G. For well-diagnosed experiments, VEHICLE-1 is installed with a movable Langmuir probe, a digital CCD camera, an optical spectrometer, a total and partial pressure gauges for plasma characterization, and equipped with an infrared pyrometer, thermocouples and a resistive heater for temperature measurements and control, respectively.

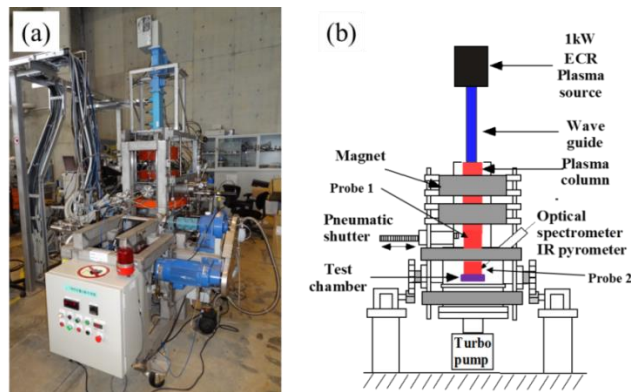


Figure 3.1 (a) The VEHICLE-1 facility and (b) a schematic diagram of the device.

Shown in Fig.3.2 is a schematic diagram of the GDP and PDP setup in VEHICLE-1. For GDP experiments, hydrogen is introduced from a gas cylinder into the closed volume, shown by the shaded area in Fig.3.2, up to $P_{H_2} = 10^4$ - 10^5 Pa. An absolute pressure gauge has been used to measure the H_2 pressure at the high pressure side, while hydrogen permeation is detected by a quadrupole mass spectrometer (QMS) in the VEHICLE-1 test chamber (to be referred to as QMS I). A resistive heater is set beneath the membrane to control the temperature. For PDP experiments, the gate valve is open and the shaded area in Fig.3.2 is kept in high vacuum. Then plasma is produced in VEHICLE-1 and the hydrogen permeation flux due to PDP can be measured by another QMS (to be referred to as QMS II). The plasma density is of the order of 10^{10} cm^{-3} , the electron temperature is $\sim 3 \text{ eV}$. The ion bombarding energy is controlled by a negative bias applied to the membrane, relative to the VEHICLE-1 machine ground.

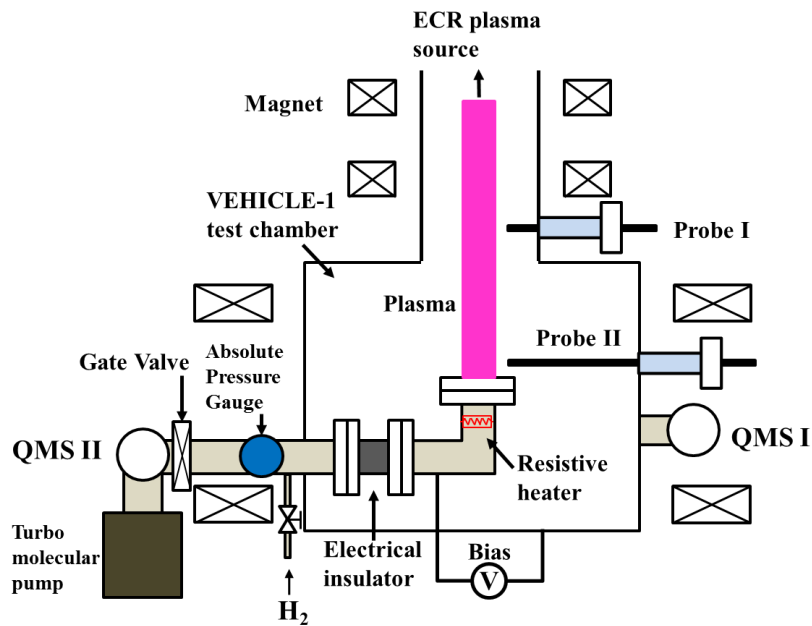


Figure 3.2 A schematic diagram of the gas-driven and plasma-driven permeation setup in VEHICLE-1. Two QMSs have been installed so that PDP, GDP and bi-directional permeation experiments can be performed.

3.2. Characterization of hydrogen plasmas in VEHICLE-1

The plasma densities and electron temperatures measured by the Langmuir probe are shown in Fig. 3.3 as a function of ECR power and in Fig.3.4 as a function of hydrogen neutral gas pressure, respectively. For the ECR power dependence measurements, the hydrogen pressure was maintained at ~ 0.2 Pa in these measurements. The electron density increases with increasing ECR power, which, however, is not the case with the electron temperature. In Fig.3.4, the ECR power is fixed at 200 W. The plasma density increases with increasing hydrogen gas pressure while the electron temperature shows an opposite trend.

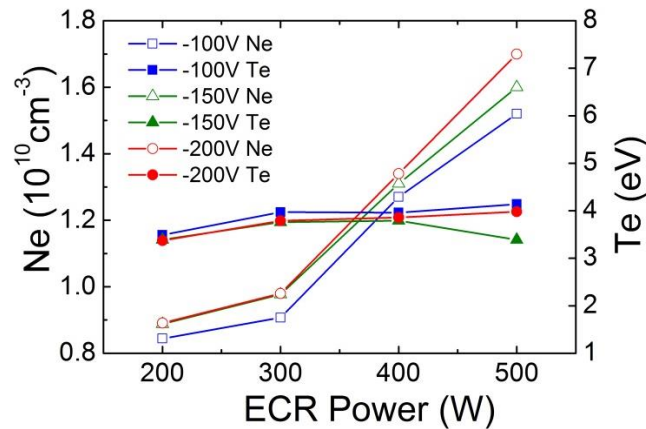


Figure 3.3 Plasma density and electron temperature as a function of ECR power.

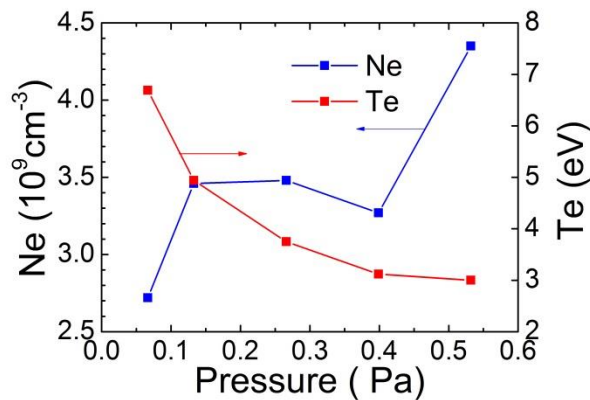
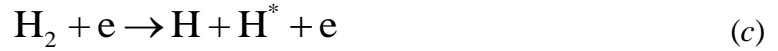


Figure 3.4 Plasma density and electron temperature as a function of hydrogen pressure.

The ion species mix of the hydrogen plasmas is estimated using a zero-dimensional model. This model includes not only the rate balance equations for H^+ , H_2^+ , H_3^+ and H atoms, as some researchers did in their work [2], but also the rate balance equation for H^- , whose concentration should not be ignored for plasmas with an electron temperature lower than 3 eV [3]. In the present study, the following reactions are considered:



The rate balance equations describing the concentrations of the ion and atom species N_j are:

$$\begin{aligned} \frac{\partial N_1}{\partial t} = & N_{\text{H}} N_{\text{e}} S_{\text{a}} + N_{\text{H}_2} N_{\text{e}} S_{\text{f}} + N_2 N_{\text{e}} S_{\text{h}} + N_{\text{H}_2} N_{\text{e}} S_{\text{m}} \\ & + 2N_2 N_{\text{e}} S_{\text{i}} - N_1 N_{\text{-}} S_{\text{o}} - N_{\text{H}_2} N_1 S_{\text{d}} - N_1 / \tau_1 \end{aligned} \quad (3.1)$$

$$\begin{aligned} \frac{\partial N_2}{\partial t} = & N_{\text{H}_2} N_1 S_{\text{d}} + N_{\text{H}_2} N_{\text{e}} S_{\text{e}} + N_3 N_{\text{e}} S_{\text{k}} - N_2 N_{\text{e}} S_{\text{g}} \\ & - N_2 N_{\text{e}} S_{\text{h}} - N_2 N_{\text{e}} S_{\text{i}} - N_2 N_{\text{H}_2} S_{\text{j}} - N_2 / \tau_2 \end{aligned} \quad (3.2)$$

$$\frac{\partial N_3}{\partial t} = N_{\text{H}_2} N_2 S_{\text{j}} - N_3 N_{\text{e}} S_{\text{k}} - N_3 N_{\text{e}} S_{\text{l}} - N_3 / \tau_3 \quad (3.3)$$

$$\frac{\partial N_{\text{-}}}{\partial t} = N_{\text{H}_2} N_{\text{e}} S_{\text{m}} - N_{\text{-}} N_{\text{e}} S_{\text{n}} - N_1 N_{\text{-}} S_{\text{o}} - N_{\text{-}} / \tau_{\text{-}} \quad (3.4)$$

$$\begin{aligned} \left(\frac{R_w}{R_p} \right)^2 \frac{\partial N_{\text{H}}}{\partial t} = & 2N_{\text{H}_2} N_{\text{e}} S_{\text{b}} + 2N_{\text{H}_2} N_{\text{e}} S_{\text{c}} + N_{\text{H}_2} N_1 S_{\text{d}} + N_2 N_{\text{e}} S_{\text{f}} \\ & + 2N_2 N_{\text{e}} S_{\text{g}} + N_2 N_{\text{e}} S_{\text{h}} + N_2 N_{\text{H}_2} S_{\text{j}} + N_3 N_{\text{e}} S_{\text{k}} \\ & + N_3 N_{\text{e}} S_{\text{l}} + 2N_1 N_{\text{-}} S_{\text{o}} + N_{\text{e}} N_{\text{-}} S_{\text{n}} - N_{\text{H}} N_{\text{e}} S_{\text{a}} \\ & + RN_1 / \tau_1 + RN_3 / \tau_3 \\ & - 2v N_{\text{H}} (R_w / R_p^2)(1 - R) / (1 - R + \eta) \end{aligned} \quad (3.5)$$

where N_1 , N_2 , N_3 , $N_{\text{-}}$, N_{H_2} and N_{H} are the densities of H^+ , H_2^+ , H_3^+ , H^- , H_2 molecules and H atoms, respectively; η is wall energy loss factor; τ_i is ion confinement time, R is the atom reflection coefficient; R_p and R_w are the radii of plasma column and chamber wall, respectively. The last term in Eq. (3.5) means H atom loss by sticking on the wall and $v/(1 - R + \eta)$ is an approximation of the velocity of H atoms after taking into account energy loss after wall reflection [2]. The reaction rate coefficients $S_{\langle \text{e} \rangle}$ used here are from reference [4].

Hydrogen molecules are regarded as the particle source C in this model, which is consistent with the ECR discharge conditions in VEHICLE-1. The rate balance equation for H_2 molecules is:

$$\begin{aligned} \frac{\partial N_{H_2}}{\partial t} = & N_3 N_e S_l - N_{H_2} N_e S_b - N_{H_2} N_e S_c - N_{H_2} N_e S_e \\ & - N_{H_2} N_e S_f - N_3 N_e S_m - N_{H_2} N_1 S_d + C \end{aligned} \quad (3.6)$$

Solving the rate balance equations (3.1) - (3.6) numerically together with the electrical neutrality condition:

$$N_e = N_1 + N_2 + N_3 - N_-, \quad (3.7)$$

the densities of the species N_j can be obtained.

Shown in Fig.3.5 is a calculation result using the zero-dimensional model. In this calculation, the electron density is set at $1 \times 10^{10} \text{ cm}^{-3}$ and the atom reflection coefficient R is assumed to be 0.9. The ion confinement time τ_i for H^+ is estimated to be $\sim 200 \mu\text{s}$ according to the plasma parameters and dimension of the VEHICLE-1 facility. The ion confinement time for other species are estimated by assuming τ_i is proportional to the square root of ion mass. The electron temperature and density data used in the calculation are taken by Langmuir probe measurements. For ECR discharges in laboratory-scale facilities, usually $T_e \gg T_i$ holds. The ion temperature is assumed to be 0.1 eV, which is the lower temperature limit of available database [4].

The modeling results indicate that H_3^+ is the dominant ion species at the electron temperature and neutral hydrogen gas pressure ($\sim 0.1 \text{ Pa}$) in our experiments. The concentration of H^+ increases as the increase of electron temperature and becomes the dominant species when the electron temperature is higher than 4 eV.

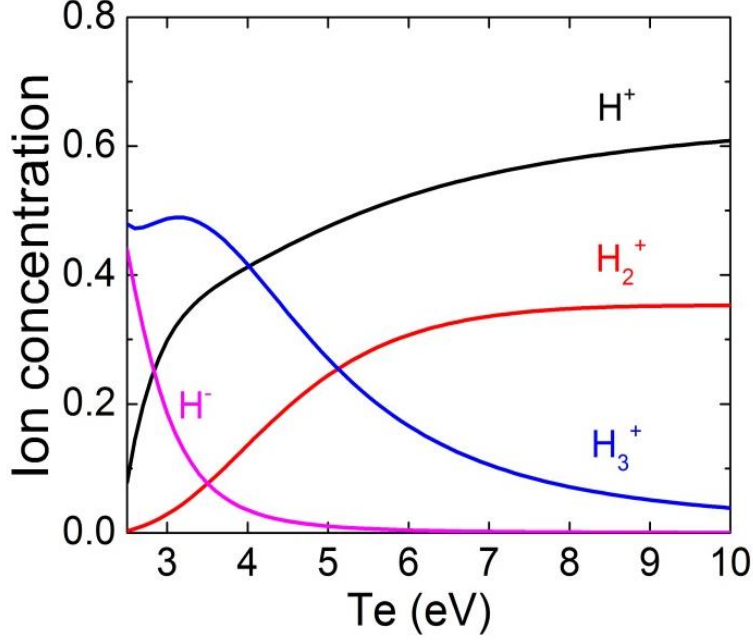


Figure 3.5 Estimation of the ion species mix using the zero-dimensional model.

Then the net implantation flux J_0 into a membrane at a certain bias voltage can be expressed in the following manner:

$$J_0 = \sum_{j=1}^3 \frac{(1 - R_{Nk}) j N_k}{2} \sqrt{\frac{k_B (T_e + T_i)}{m_{H_j^+}}} \quad (3.8)$$

where k_B is the Boltzmann constant, T_e and T_i ($T_i \approx 0$) are the electron and ion temperatures, respectively, and R_{Nk} is the particle reflection coefficient calculated from the Monte Carlo program, SRIM (See Fig.2.2 in Chapter 2). The net implantation flux is estimated to be of the order of $10^{15} \sim 10^{16}$ H/cm²/s for VEHICLE-1 hydrogen plasmas.

As presented in Section 1.3 of Chapter 1, the cross-field particle flux to the first wall of a fusion power reactor has been estimated to be of the order of 10^{16} H/cm²/s. It is thus believed that the plasma bombardment conditions in VEHICLE-1 are relevant to those to be seen in the first wall environment of fusion reactors

3.3. Sample preparation and analysis methods

The permeation samples are cut from the F82H plates used in the JFT-2M tokamak in JAERI (now JAEA) [5]. The samples are prepared in the same dimensions as those commercially available conflat flanges with an outer diameter of 70 mm, except that a circular area of ~35 mm in diameter inside the knife-edge is machined down to thicknesses of 0.5 mm to 5 mm to use as permeation membranes, as shown in Fig.3.6 (a) and (b). Plasma-facing surfaces of the membranes are mechanically polished and then cleaned in an ultrasonic bath. SUS304 membranes prepared in the same way are also used in some of the experiments as a reference material.

For the PDP experiments, the plasma-facing side of the membrane is covered by a stainless steel mask which has a 35 mm diameter hole. Although the diameter of the cylindrical plasma column is ~70 mm, only the central membrane area of the sample is exposed to the plasma, as shown in Fig.3.6 (c) and (d).

The membrane surface before and after permeation experiment is analyzed by optical microscope, scanning electron microscope (SEM), energy dispersive X-ray spectroscopy (EDX) and X-ray photoelectron spectroscopy (XPS) as a routine procedure. For the XPS analysis, Ar⁺ sputtering at 4 kV is utilized so that the depth profile can be obtained. The sputtering rate for F82H has been calibrated using long-time sputtering and a crater profile analysis method [6].

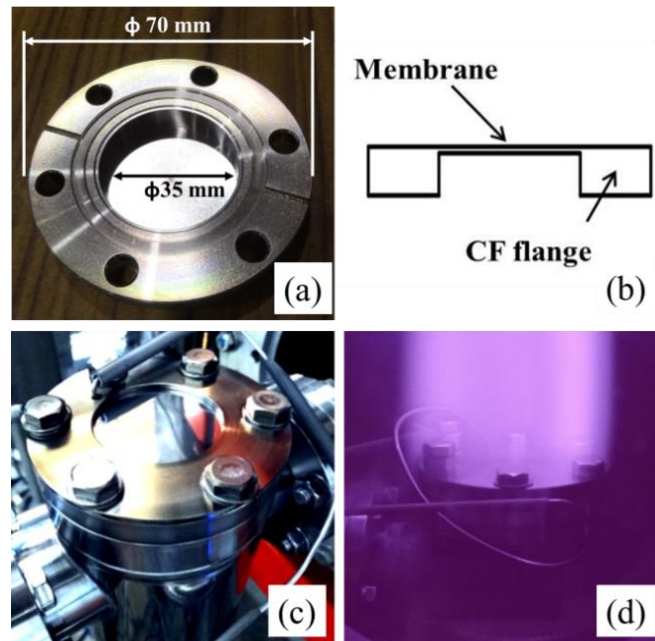


Figure 3.6 (a) A picture of the permeation membrane sample with dimensions; (b) a schematic diagram of the permeation membrane; (c) a sample installed with a mask and (d) a sample exposed to hydrogen plasma.

3.4. Gas-driven permeation

Figure 3.7 shows the GDP flux through a 5 mm thick F82H membrane. The steady state sample temperature is around 500 °C. The upstream driving pressure is set at $\sim 10^4$ Pa, which is relevant to the tritium dissociation pressure from FLiBe at 527 °C and at a (T/M) concentration of ~ 0.1 ppm [7]. The steady state gas-driven permeation flux is measured to be $\sim 1 \times 10^{15}$ H cm⁻²s⁻¹.

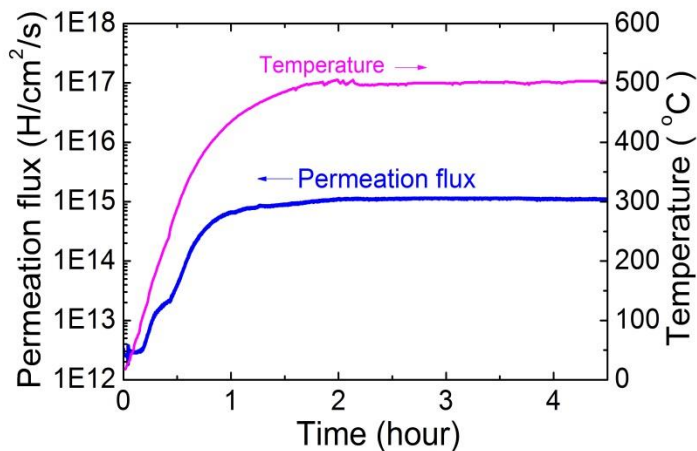


Figure 3.7 Hydrogen GDP breakthrough curve for a 5 mm F82H membrane at a surface temperature of ~500 °C.

The steady state GDP data have been taken for F82H membranes at temperatures between ~245 °C and ~510 °C. Shown in Fig.3.8 are the GDP permeation fluxes as a function of upstream hydrogen pressure, from which one can find a linear relation between the GDP flux and the square root of upstream pressure at all the temperatures examined in this study.

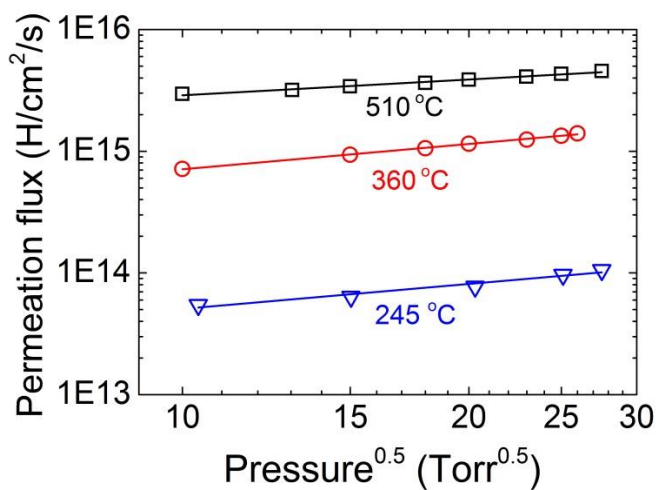


Figure 3.8 Steady state hydrogen GDP fluxes through a 1 mm thick F82H membrane at temperatures of ~245 °C, ~360 °C and ~510 °C.

Notice that the experimental data lines don't appear to intersect the zero point at $P_{up} = 0$, which is presumably due to the desorption of residual hydrogen from previous experiments.

Shown in Fig.3.9 are the steady state permeation fluxes taken from GDP experiments on 1, 2 and 5 mm thick F82H membranes under an upstream pressure of $\sim 10^4$ Pa and a sample temperature of 500°C . The data suggest that the permeation flux is inversely proportional to the membrane thickness.

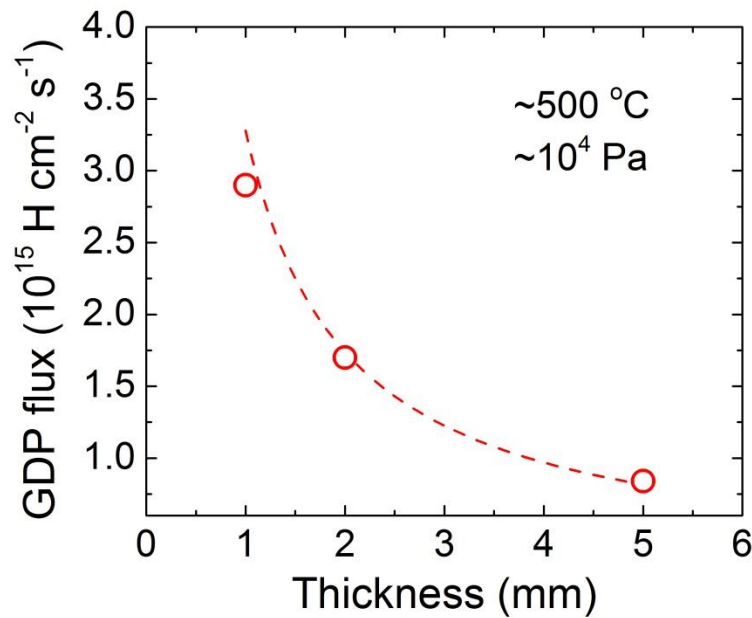


Figure 3.9 Steady state hydrogen GDP flux through F82H membranes at $\sim 500^\circ\text{C}$ with an upstream pressure of $\sim 10^4$ Pa.

All the experimental data agree with the theoretical prediction for the steady state diffusion-limited GDP flux given by Eq. (2.13), assuming downstream pressure $P_{down}=0$:

$$J_+ = DS \frac{\sqrt{P_{up}}}{L} = \Phi \frac{\sqrt{P_{up}}}{L}, \quad (3.9)$$

where Φ [$\text{mol}\cdot\text{cm}^{-1}\cdot\text{s}^{-1}\cdot\text{Pa}^{-1/2}$] is the permeability and $\Phi = DS$. *Gas-driven permeation through F82H under all the experimental conditions examined in this work is diffusion-limited.*

The measurement of the steady state GDP flux will lead to the permeability and Sieverts' constant. Shown in Fig. 3.10 is the evaluated hydrogen permeability for SUS304 from 445 to 510 °C. In this temperature range, the permeability P [$\text{mol}\cdot\text{cm}^{-1}\cdot\text{s}^{-1}\cdot\text{Pa}^{-1/2}$] is expressed as:

$$P = 9.6 \times 10^{-10} \exp\left(\frac{-0.62 \text{ [eV]}}{kT}\right), \quad (3.10)$$

which is close to the literature data for SUS304 given by Katsuta et al. [8].

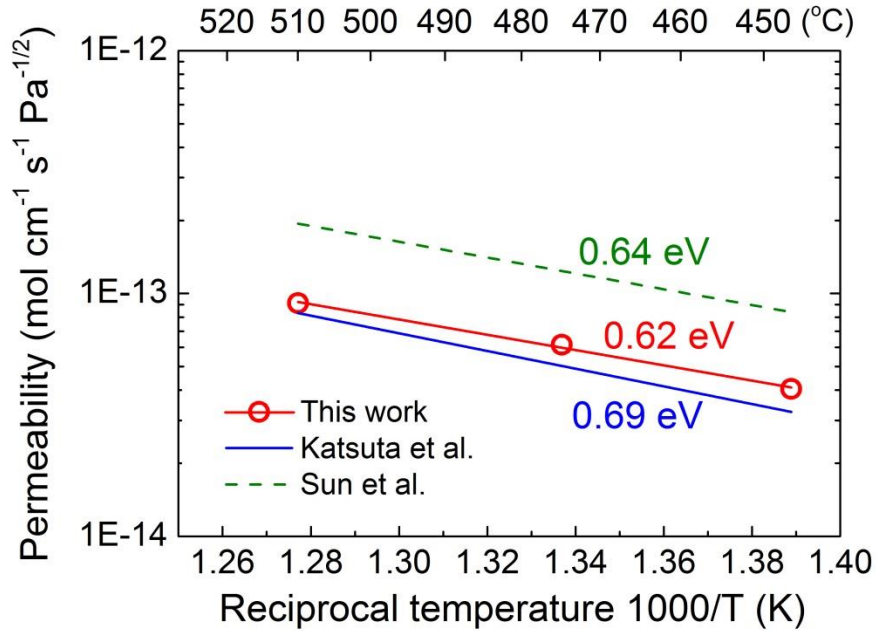


Figure 3.10 Hydrogen isotopes permeability through SUS304. Katsuta's data [8] and Sun's [9] data are shown for comparison.

Shown in Fig. 3.11 are the results of hydrogen permeability measurements for F82H from 165 to 520 °C. The permeability P from the present experiments is given by:

$$P = 2.3 \times 10^{-10} \exp\left(\frac{-0.39 \text{ [eV]}}{kT}\right). \quad (3.11)$$

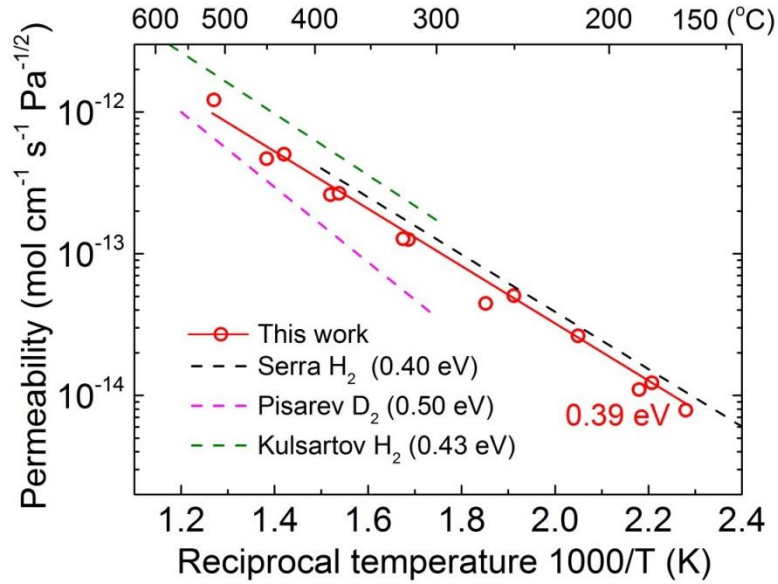


Figure 3.11 Hydrogen isotopes permeability through F82H. Serra's [10], Pisarev's [11] and Kulsartov's [12] data are shown for comparison.

The diffusion coefficient D [$\text{cm}^2 \cdot \text{s}^{-1}$] can be measured from the transient permeation behavior. A time dependent expression for the hydrogen permeation flux $J_+(t)$ through a membrane is possible to obtain for the case where the input hydrogen pressure is instantaneously increased from zero to p [Pa] and where the initial concentration throughout the membrane is zero [13]:

$$J_+(t) = \frac{DC_0}{L} \times \left[1 + 2 \sum_{n=1}^{\infty} (-1)^n \exp\left(-D \frac{n^2 \pi^2}{L^2} t\right) \right], \quad (3.12)$$

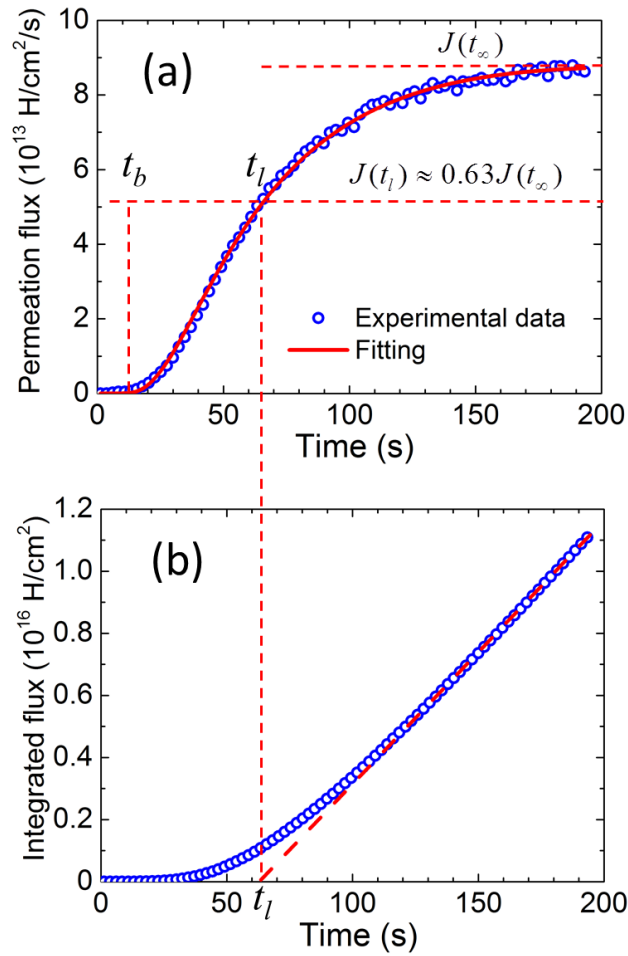


Figure 3.12 An example of diffusivity measurement: (a) fitting the transient GDP flux curve and (b) time lag from time-integrated GDP flux. In this case, the F82H membrane thickness is 1 mm and the temperature is 250 °C. The upstream hydrogen pressure is 3.3×10^4 Pa. The lag time is measured to be ~63 s.

where $C_0 = S \cdot p^{1/2}$ is concentration by Sieverts' law; S [mol·cm⁻³·Pa^{-1/2}] is Sieverts' constant and L [cm] is the membrane thickness. The diffusion coefficient can be obtained by fitting the transient permeation flux data, as shown in Fig. 3.12(a).

Diffusivity can also be estimated either by measuring the time lag $t_l=L^2/6D$, at which a line fitted to the asymptotic region of the time-integrated flux curve intersects the time axis (Fig.3.12(b)), or by measuring the breakthrough time $t_b\approx L^2/15.3D$ [14]. All of the above-mentioned three methods can be used to obtain D , depending on the experimental data conditions. For example, if the transient curve is not available, D can be measured from the steady state data by time lag method. On the other hand, breakthrough time measurement would be useful when the permeation flux cannot reach steady state.

Shown in Fig. 3.13 is the evaluated hydrogen permeability for SUS304 from 445 to 510 °C. The diffusion coefficient D [$\text{cm}^2\cdot\text{s}^{-1}$] has been measured to be:

$$D = 5.5 \times 10^{-3} \exp\left(\frac{-0.57 \text{ [eV]}}{kT}\right). \quad (3.13)$$

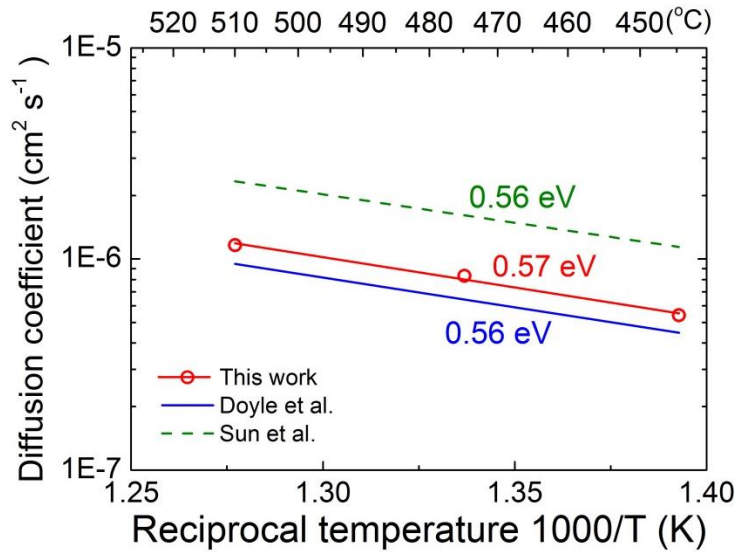


Figure 3.13 Hydrogen isotopes diffusion coefficients measured for SUS304. Sun’s data [9] and Doyle’s data [20] are shown for comparison.

Sieverts' constant (solubility) S [$\text{mol}\cdot\text{cm}^{-3}\cdot\text{Pa}^{-1/2}$] for SUS304 can be obtained by $S=P/D$ as:

$$S = 1.8 \times 10^{-7} \exp\left(\frac{-0.05 \text{ [eV]}}{kT}\right). \quad (3.14)$$

The small value for the heat of solution indicates a relatively weak temperature dependence for the solubility of hydrogen in SUS304.

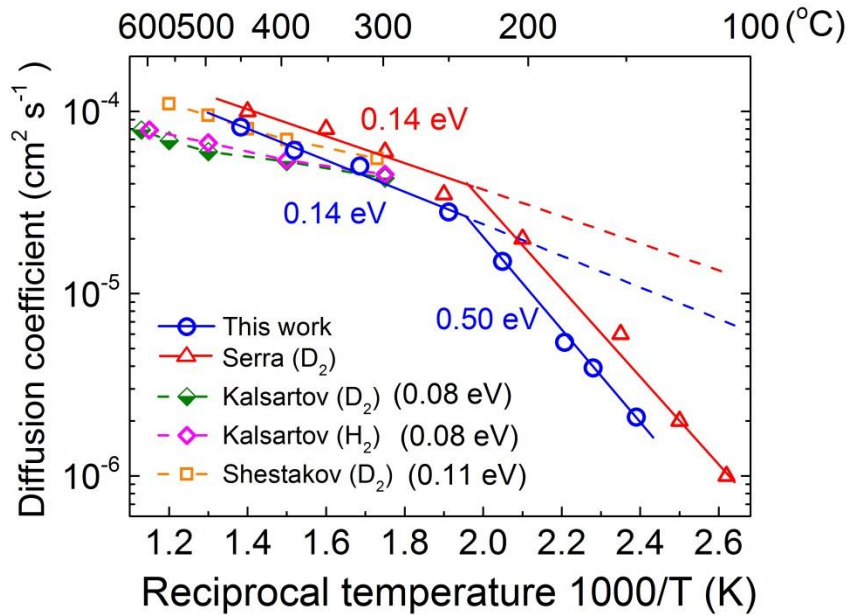


Figure 3.14 Hydrogen isotopes diffusion coefficients measured for F82H. Serra's [10], Kalsartov's [12] and Shestakov's [17] data are shown for comparison.

The diffusion coefficient for F82H has been evaluated in a temperature range of 150-450 °C, as shown in Fig. 3.14. Literature data for F82H are also shown for a comparison. A breaking point around ~250 °C has been reported in other works as well when measuring D for high chromium martensitic/ferritic steels [10,15]. A possible reason for the breaking point

is the trapping effect. In the presence of trapping sites, the diffusion process is described by Eq. (2.6) in Chapter 2:

$$\frac{\partial C(x,t)}{\partial t} = D(T) \frac{\partial^2 C(x,t)}{\partial x^2} - \frac{\partial C_t(x,t)}{\partial t} + G(x,t), \quad (2.6)$$

which indicates that the initial transient permeation behavior is affected by trapping, and as a result, the measurement of effective diffusivity D_{eff} may be affected as well. Oriani [16] gave the relation between D_{eff} and the lattice diffusivity D_L for the low trap coverage case:

$$D_{\text{eff}} = D_L [1 + N_T / N_L \exp(-U_t / kT)]^{-1}, \quad (3.15)$$

where U_t is the trapping energy; N_L and N_T are the density of lattice and trapping sites, respectively. It follows from Eq. (3.12) that D_{eff} is lower than D_L at low temperatures, but $D_{\text{eff}} \approx D_L$ when the temperature is high enough, which is in accord with our experimental result.

In fusion reactors, blankets are required to operate at elevated temperatures for efficient heat exchange. For example, the operation temperature for the first wall made of F82H is ~ 500 °C [18]. The diffusion coefficient D at temperatures >250 °C from the present work can be expressed by

$$D = 7.5 \times 10^{-4} \exp\left(\frac{-0.14 \text{ [eV]}}{kT}\right). \quad (3.16)$$

Then, Sieverts' constant S for F82H can be given as following:

$$S = 3.1 \times 10^{-7} \exp\left(\frac{-0.25 \text{ [eV]}}{kT}\right). \quad (3.17)$$

3.5. Plasma-driven permeation

Figure 3.15 shows the PDP flux through a 5 mm thick F82H membrane with a polished surface. The plasma is produced with a hydrogen gas pressure of ~ 0.2 Pa. The ECR power and bias are set at 550 W and -100 V, respectively. Under such discharge condition, the electron temperature and density are measured by the Langmuir probe to be 3.5 eV and $3 \times 10^{10} \text{ cm}^{-3}$, respectively. At 500 °C, the steady state permeation flux has been found to be $\sim 3 \times 10^{13} \text{ H/cm}^2/\text{s}$.

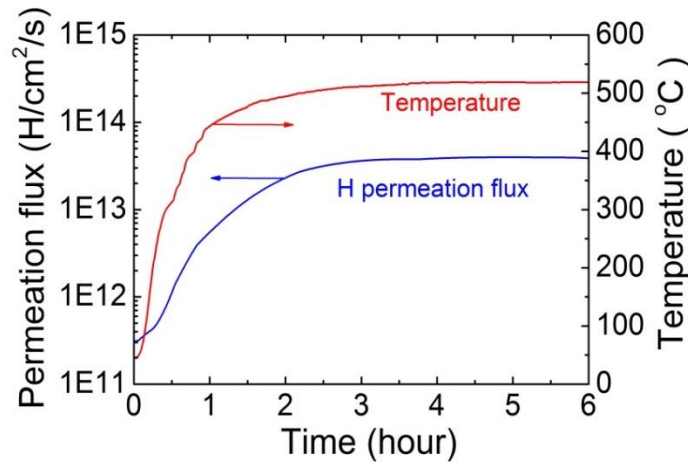


Figure 3.15 Hydrogen PDP breakthrough curve for a 5 mm F82H membrane at a surface temperature of ~ 500 °C

Shown in Fig. 3.16 are the hydrogen permeation data taken from PDP experiments on 1, 2 and 5 mm thick F82H membranes at surface temperatures of ~ 220 °C and ~ 500 °C. For these experiments, the electron density and temperature are measured to be 3 eV and $1 \times 10^{10} \text{ cm}^{-3}$. Using Eq. (3.8), the net implantation flux J_0 has been estimated to be $\sim 5 \times 10^{15} \text{ H/cm}^2/\text{s}$, which suggests a permeation flux ratio J_+/J_0 to be of the order of $10^{-4} - 10^{-3}$.

The steady state permeation fluxes through F82H are inversely proportional to the membrane thickness under all the temperatures examined. Recombination-limited release may be assumed for the upstream surface in this study because the implantation depth is only

several nm at a bias of -100 V [19] and the possibility of DD-limited regime can be excluded as well by the measured permeation flux ratios. That's to say, *hydrogen plasma-driven permeation through F82H in the present study is in the recombination-diffusion limited regime.*

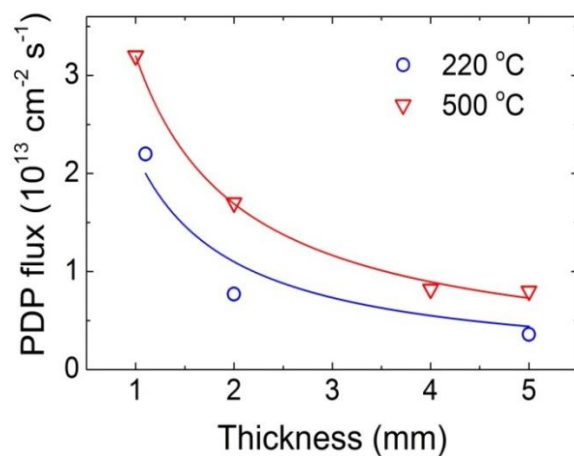


Figure 3.16 Steady state hydrogen PDP fluxes through F82H membranes at ~220 °C and ~500 °C.

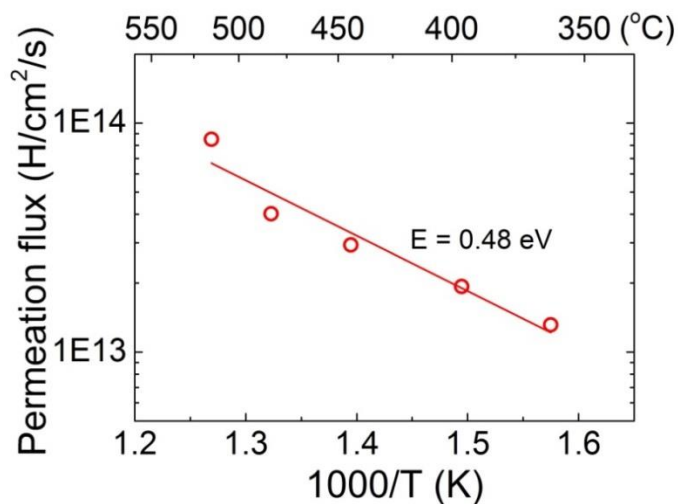


Figure 3.17 Temperature effect on steady state hydrogen PDP fluxes through F82H.

Hydrogen PDP fluxes through F82H membranes have also been measured as a function of temperature. Shown in Fig. 3.17 is the temperature dependence of PDP flux for a 1 mm thick F82H membrane. From the Arrhenius plots the permeability enthalpy, U_p , is estimated to be 0.48 eV. For PDP taking place in the RD-regime, U_p can be related to energies for surface recombination (U_K) and diffusion (U_D) as follows: $U_p \approx U_D - 0.5U_K = 0.48$ eV. Using the available U_D for F82H (0.14 eV), a negative U_K is obtained, indicating that the recombination coefficient K_r may decrease at elevated temperatures.

As introduced in Chapter 2, for hydrogen PDP taking place in the RD-regime, the steady state permeation flux J_+ [$\text{atoms}\cdot\text{cm}^{-2}\cdot\text{s}^{-1}$] is inversely proportional to the square root of the upstream recombination coefficient Kr :

$$J_+ = \frac{D}{L} \sqrt{\frac{J_0}{K_r}}, \quad (2.16)$$

i.e., when D and L are known, Kr can be obtained from the measurements of J_+ and J_0 .

Recombination coefficient Kr is extremely sensitive to the surface condition. For example, the reported data for stainless steel span several orders of magnitude [20]. Surface effects on hydrogen PDP through F82H have been separately investigated and the details are shown in the next section. In this study, the membrane is polished and analyzed by energy dispersive X-ray spectroscopy to make sure no major impurities are left on the surface. Prior to hydrogen PDP experiments, argon plasma bombardment is conducted for 10 minutes at -50V so as to remove surface contamination from air exposure. Having surface conditioning done, Kr is assumed to be evaluated from a relatively “clean” surface.

To validate the experimental method, evaluation of Kr for SUS304 has been performed and compared with literature data. Shown in Fig. 3.18 are the Kr [$\text{cm}^4\cdot\text{s}^{-1}$] data taken for SUS304, which can be expressed as following:

$$K_r = 2.9 \times 10^{-20} \exp\left(\frac{-0.26 \text{ [eV]}}{kT}\right) \quad (3.18)$$

The experimental results are in good agreement with literature data, which means the method used in this research is valid for the evaluation of other first wall candidate materials.

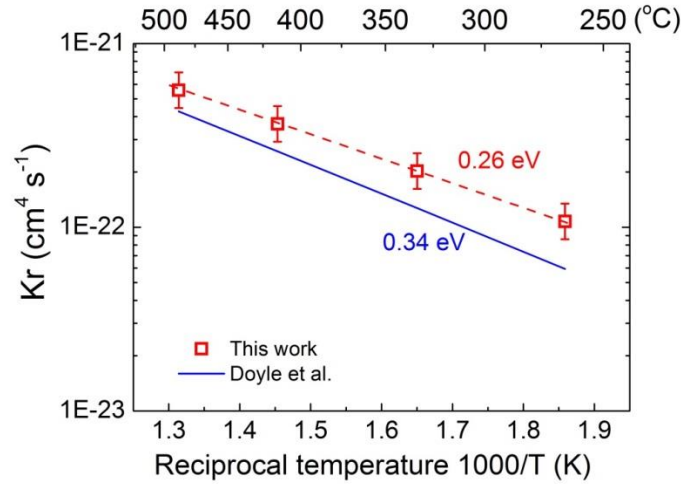


Figure 3.18 Hydrogen recombination coefficients K_r for SUS304.

Doyle's data [20] are shown for comparison.

Then the same evaluation method is applied to F82H. Shown in Fig.3.19 are the K_r data from the present work:

$$K_r = 4.8 \times 10^{-21} \exp\left(\frac{0.48 \text{ [eV]}}{kT}\right) \quad (3.19)$$

The experimental error mainly comes from the measurement of the implantation flux. To allow a comparison, recombination coefficients for α -Fe [21,22] and F82H [23] are also shown in Fig. 3.19. It can be seen that the measured K_r for F82H decreases at elevated temperatures, which is similar to the trend for α -Fe. This result is opposite to Hirata's

theoretical calculation [23], in which case the hydrogen transport parameters of DIN 1.4914 are used as the input data.

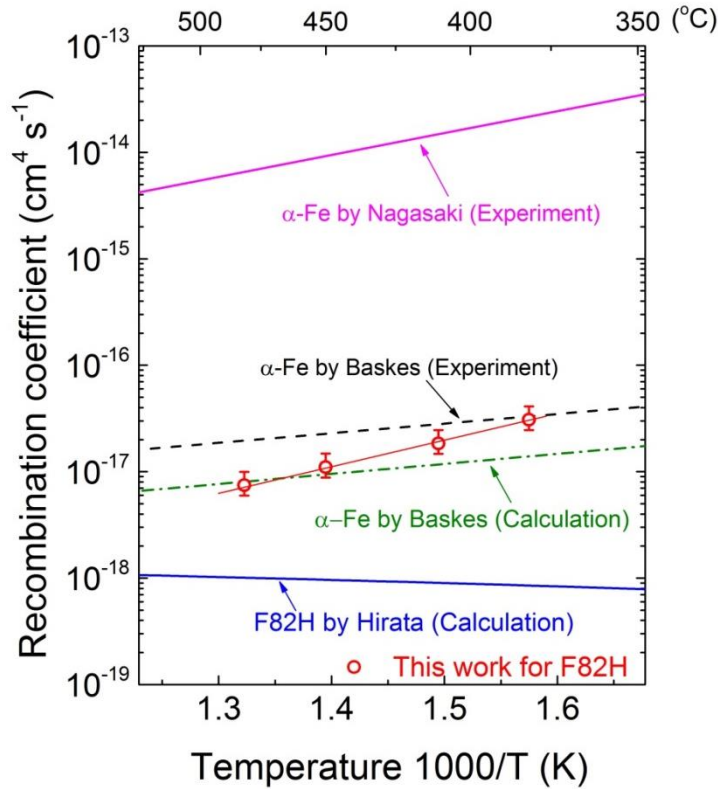


Figure 3.19 Hydrogen recombination coefficients K_r for F82H. The data for α -Fe [21,22] and F82H [23] are shown for comparison.

Using the steady state PDP model and the transport parameters measured by the present experiments, plasma exposure-induced hydrogen permeation flux and average concentration in a first wall made of bare F82H can be estimated under various blanket conditions. It must be pointed out that the hydrogen inventory discussed here is the dynamic inventory from solution, and the retention caused by trapping is not included. Shown in Fig. 3.20 is the calculation result for a 5 mm thick wall with a net implantation flux of 10^{16} atoms \cdot cm $^{-2}\cdot$ s $^{-1}$.

The permeation flux is calculated by Eq. (2.16) and the average concentration \bar{C} (atom·cm⁻³) is given by [24]:

$$\bar{C} \approx (J_0/K_r)^{1/2}(1+W)/2, \quad (3.20)$$

where W is the permeation parameter defined by Eq. (2.14). Notice that in this temperature range, the hydrogenic inventory in F82H tends to be larger at higher temperatures.

The hydrogenic PDP flux and inventory around 500 °C have been estimated to be $\sim 1.0 \times 10^{13}$ atoms·cm⁻²·s⁻¹ and 1.3×10^{16} atoms·cm⁻², respectively, which means hydrogen isotope PDP through a 1000 m² first wall would be ~ 22 g/day tritium and ~ 14 g/day deuterium, assuming a 50% T and 50% D particle composition.

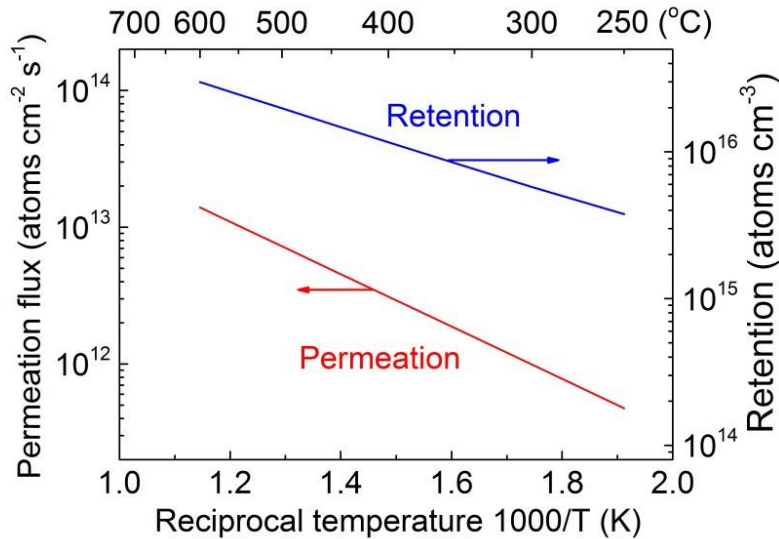


Figure 3.20 Calculations of the steady state tritium PDP flux and retention for a 0.5 cm thick F82H first wall. A net implantation flux of 10^{16} atoms·cm⁻²·s⁻¹ is assumed.

3.6. Surface effects on plasma-driven permeation

Under reactor operational conditions, the plasma-facing side of the first wall would not be as smooth and clean as those polished samples used in laboratories. The wall will be either covered by contaminations, or eroded by plasma bombardment, depending upon the local plasma conditions [25]. Although it is well known that plasma-driven permeation is affected by the surface conditions of membranes [26-33], more detailed study on this issue is still needed, especially concerning the surface area effects.

In the present work, two aspects on surface effects on hydrogen PDP are separately examined: one is because of surface contamination; and the other is due to the variation in surface area.

3.6.1. Models on surface modification effects on PDP

In this section, some possible mechanisms related to the surface condition effects on plasma-driven permeation are briefly reviewed, including both contamination and area effects. The validity of these theoretical models is shown in Section 3.6.2.

3.6.1.1. Surface contamination effects on PDP

As indicated in Section 3.5, hydrogen PDP through F82H under current experimental conditions takes place in the RD limited regime, i.e., recombination-limited at the front surface and diffusion-limited inside the bulk, as shown in Fig. 3.21 (a). Steady state permeation can be expressed by the following equations:

$$J_0 = J_- + J_+ \quad (3.21)$$

$$J_- = K_r \cdot C_s^2 \quad (2.10)$$

$$J_+ = D \cdot C_s / L \approx \frac{D}{L} \sqrt{\frac{J_0}{K_r}} \quad (2.16)$$

where J_0 is the net implantation flux, J_- is the recombination release (i.e. reemission) flux from the upstream surface, J_+ is the permeation flux, C_s is the front surface hydrogen concentration and K_r is the recombination coefficient of the plasma-facing surface.

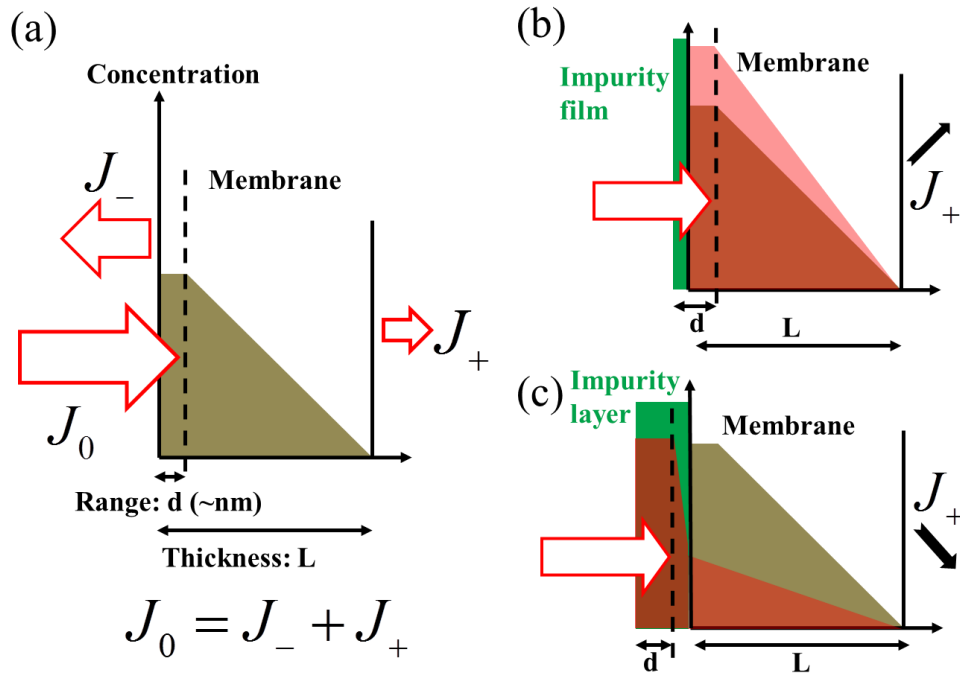


Figure 3.21 Plasma-driven permeation takes place in the RD-limited regime for (a) a clean surface, (b) a contaminated surface with thin film and (c) a contaminated surface with thick impurity layer.

Some literature data suggest that the hydrogen PDP flux J_+ is enhanced when the plasma-facing surface is contaminated [27-30]. That is because recombination release J_- is suppressed by the presence of impurity film, as shown in Fig. 3.21 (b). However, it is also true that if the contaminated layer is thick enough to act as a second layer for diffusion, hydrogen PDP will be suppressed (Fig. 3.21 (c)) [31,32]. The latter case is of interest from the fusion engineering point of view as it suggests a potential measure to reduce hydrogen PDP through the first wall in a reactor.

3.6.1.2. Surface area effects on PDP

The surface of plasma-facing walls can be modified significantly by plasma bombardment. Surface morphologies such as bubbles [34], coral-like structures and cones [25] may be formed, depending on the plasma conditions, material property, temperature and impurity seeding, etc. Those micron scale structures will change the plasma exposure area and result in higher hydrogen release at the front surface. Considering particle conservation and surface reflection, the net implantation fluxes can be expressed as $J_0 = J_p \cdot (1-R_0)$ for a polished surface and $J_1 = J_p \cdot A_0/A_1 \cdot (1-R_1)$ for a modified surface, where J_p is the ion incident flux, A_0 and A_1 are the surface areas for a polished surface and a modified surface, respectively, and R_0 and R_1 are the corresponding particle reflection coefficients, as shown in Fig. 3.22. Using Eq. (3), the steady state permeation flux ratio J_{1+}/J_{0+} of the two cases can be given as:

$$J_{1+} / J_{0+} \propto \sqrt{A_0 / A_1} \quad (3.22)$$

i.e., the permeation flux is inversely proportional to the square root of surface area.

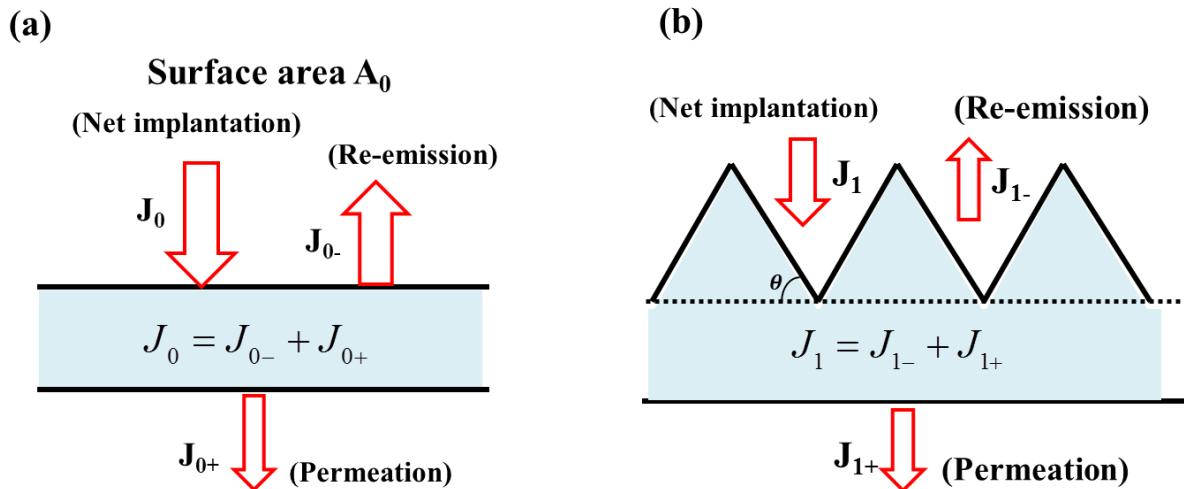


Figure 3.22 Schematic diagrams of the surface area effects on plasma-driven permeation.

3.6.2. Surface condition effects experiments

3.6.2.1 Surface contamination effects observed in VEHICLE-1

In VEHICLE-1, the contamination effects have been investigated by introducing oxide layers on F82H. These samples are exposed to hydrogen plasmas with an electron density of $\sim 5 \times 10^9 \text{ cm}^{-3}$ and a temperature of $\sim 3.5 \text{ eV}$. A bias of -50 V is applied onto the membrane flange, relative to the VEHICLE-1 machine ground. The hydrogen PDP behavior with/without surface oxidation is shown in Fig.3.23. After oxidation, it takes a longer time for the permeation flux to reach steady state, suggesting a lower effective diffusion coefficient for the oxidized samples. For the 270 min (4.5 h) oxidation case, the steady-state permeation flux is lower by a factor of ~ 1.5 than that of a “clean” membrane.

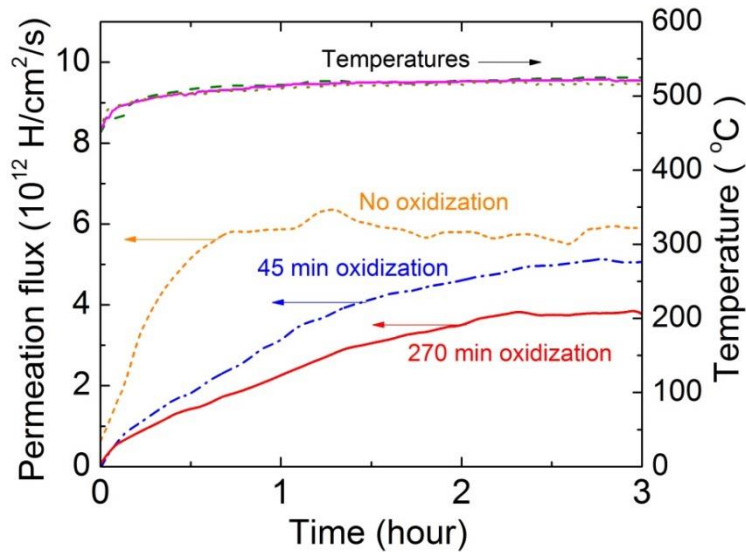


Figure 3.23 Hydrogen PDP through clean and oxidized F82H membranes at a temperature around 520 °C.

Figure 3.24 shows the XPS analysis results for (a) a polished surface before PDP, (b) a surface after 0.75 h oxidization and (c) a surface after 0.75 h oxidization and 3 h plasma exposure. Notice that the implantation range of hydrogen particles in iron is less than several

nm at an implantation energy of <50 eV [35], while the thickness of the oxide layer is tens of nm, which should be thick enough to act as a second layer for diffusion, as illustrated in Fig.3.21 (c). Plasma exposure can reduce the impurity layer thickness by chemical sputtering, which has been observed by measuring the water partial pressure in the plasma side during the PDP experiments (Fig.3.24 (d)). However, the XPS results indicate that the surface oxides would never be depleted completely under current experimental conditions (as shown in Fig.3.24 (c)), and as a result, the steady state PDP through these oxidized membranes is lower than a polished one.

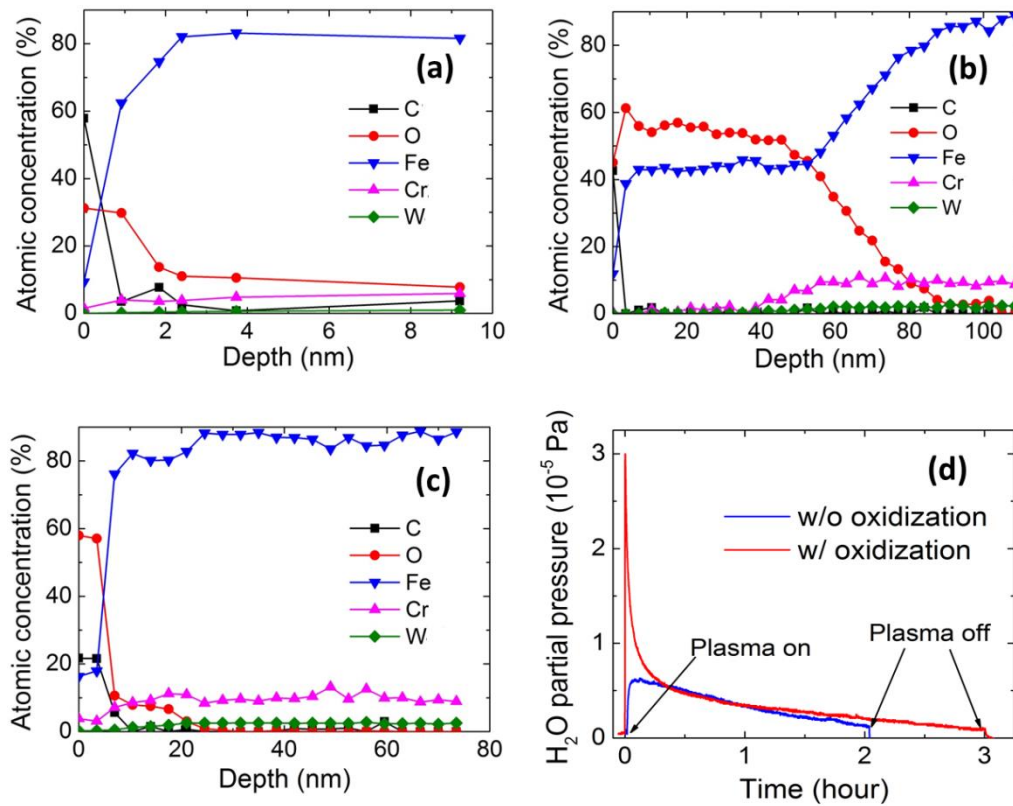


Figure 3.24 XPS results for (a) a polished surface, (b) a surface oxidized at ~450 °C by oxygen gas at $\sim 1.3 \times 10^{-2}$ Pa for 0.75 h, (c) a surface after 0.75 h oxidation and 3 h plasma exposure and (d) water partial pressure measurements at the plasma side in the PDP experiments for oxidized and clean samples, respectively..

3.6.2.2. Surface area effects on PDP

Shown in Fig. 3.25 (a) are the hydrogen PDP data taken from 1 mm thick F82H with polished and cone-covered surfaces at ~ 530 °C. The surface morphologies by SEM for the polished and plasma-modified sample are shown in Fig. 3.25 (b) and Fig. 3.25 (c), respectively. Compared with the polished surface, the steady state PDP flux for the plasma modified surface has been found to decrease by a factor of ~ 1.7 , indicating a surface area ratio of $A_1/A_0 = \sim 2.8$. A similar effect was observed for deuterium PDP through stainless steel whose surface was modified by molybdenum-seeded plasma bombardment in PISCES [25].

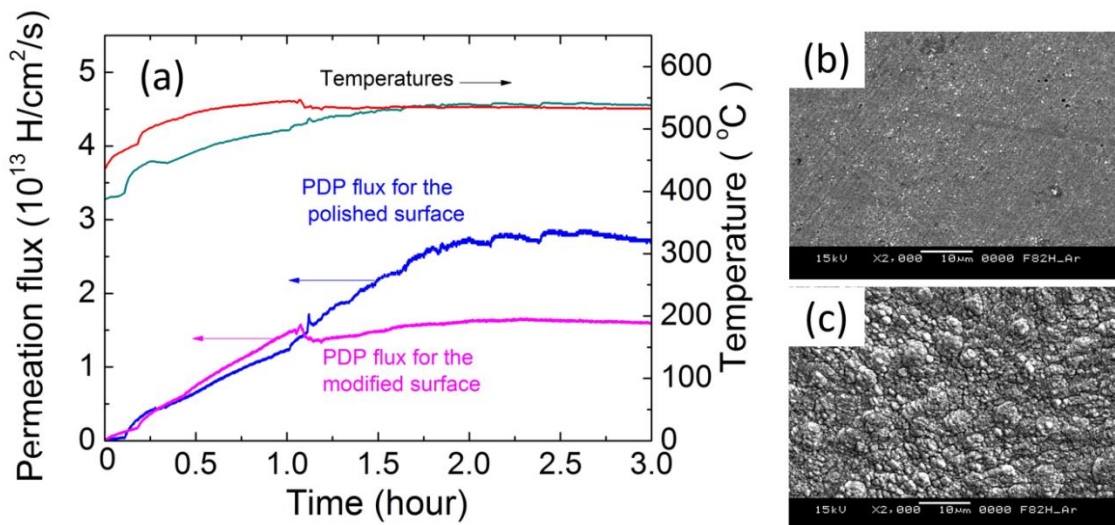


Figure 3.25 (a) Hydrogen PDP behavior through F82H before and after cone formation. (b) The surface morphology by SEM for the polished sample and (c) the surface morphology by SEM for a plasma-modified sample.

To further verify the area effects model proposed in Section 3.6.1.2, PDP experiments have been performed using samples with well controlled surface morphology. In these experiments, the electron density and temperature are around ~ 3.5 eV and $\sim 1.2 \times 10^{10}$ cm⁻³, respectively. A negative bias voltage of -100 V is applied. The sample membranes are heated

up to a steady state temperature of ~ 500 °C by resistive heater radiation and plasma bombardment.

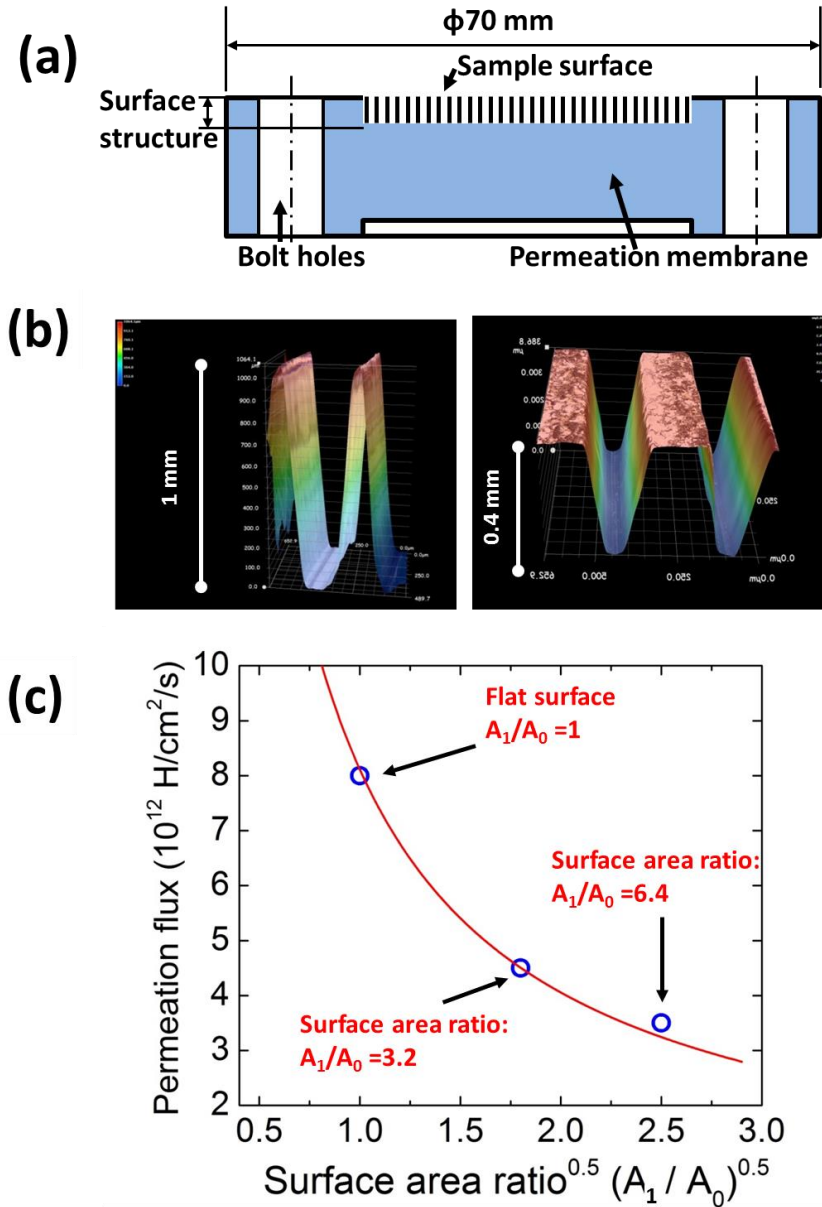


Figure 3.26 (a) A schematic diagram of the modified permeation sample membrane; (b) 3D figures observed by an optical microscope and (c) measured PDP fluxes as a function of the square root surface area.

Figure 3.26 (a) shows a schematic diagram of the surface-modified permeation membrane. The first 1 mm or 0.4 mm of the 5 mm thick F82H membrane is machined into V-shape grooves to increase the surface area. From the dimension measurements by a microscope (as shown in Fig. 3.26 (b)), the areas of the modified surfaces are measured to be larger by a factor of ~6.4 and ~3.2 than a flat one, respectively. The effective thickness of the modified sample membrane is between 4 and 5 mm. Equation (3.22) suggests that when plasma-driven permeation is in the RD limited regime, the steady state permeation flux is inversely proportional to the square root of surface area.

Shown in Fig.3.26 (c) are the PDP flux measurement results. The measured steady state permeation flux has been found to be inversely proportional to the square root of surface area, which is in excellent agreement with the model prediction.

3.7. Discussion

3.7.1. Comparison of the PDP behavior for F82H and SUS304

The vacuum chamber walls of most current fusion experimental devices are made by stainless steel. To allow a comparison, plasma-driven permeation through SUS304 has been studied as well. Figure 3.27 shows the PDP fluxes through 1 mm thick F82H and SUS304 membranes. For these experiments, the plasma density is of the order of 10^{10} cm^{-3} , the electron temperature is ~3 eV and the net implantation flux is estimated to be around $5 \times 10^{15} \text{ H} \cdot \text{cm}^{-2} \cdot \text{s}^{-1}$.

At ~220 °C, the steady state permeation flux for F82H has been measured to be $2.2 \times 10^{13} \text{ H} \cdot \text{cm}^{-2} \cdot \text{s}^{-1}$, which is about one order of magnitude larger than that of SUS304. For diffusion-limited hydrogen permeation, the steady state PDP flux is proportional to the diffusion coefficient D . The diffusion coefficient of F82H is about 3 orders of magnitude higher than that of stainless steel at ~220 °C [20]. Generally, the diffusion distance is of the order of \sqrt{Dt} . Using the diffusion coefficient data, the diffusion distances are estimated to be 7.6 mm for

F82H and 0.1 mm for SUS304 at 220 °C in a time scale of 1.6×10^4 s, the duration of the PDP experiments.

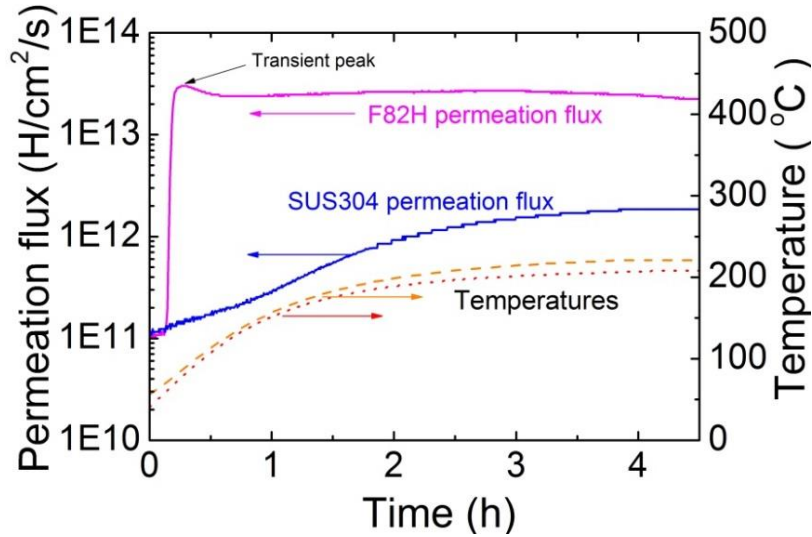


Figure 3.27 Hydrogen PDP through 1 mm thick F82H and SUS304 membranes.

A transient peak has been observed for F82H in this experiment, reaching a maximum PDP flux of $\sim 3.0 \times 10^{13} \text{ H} \cdot \text{cm}^{-2} \cdot \text{s}^{-1}$. The transient peak was usually attributed to the following reasons: (1) changes in surface recombination coefficient due to sputtering or deposition of contaminations (e.g., Causey et al. [27]); (2) changes in surface recombination coefficient and diffusivity due to ion-induced surface defects (e.g., Winter et al. [36]).

In the present work, the sample has been pre-conditioned by Ar-plasma, which means the surface is relatively “clean” before the PDP experiments. On the other hand, the incident energy is not high enough ($< 100 \text{ eV}$) to make significant damage to the sample. The transient peak may be due to the recombinative desorption of the residual hydrogen atoms together with those penetrating through the membrane, as shown in Fig. 3.28. After the residual hydrogen atoms are depleted, the permeation flux is decreased.

Such a behavior has not been found for SUS304, which has a much smaller hydrogen diffusion coefficient in this temperature range. The “residual atom-assisted” desorption process is not significant for the 1 mm thick SUS304 membrane at 220 °C because the arriving rate of the penetrating hydrogen atoms is too slow and the residual atoms may be released in a relatively mild way.

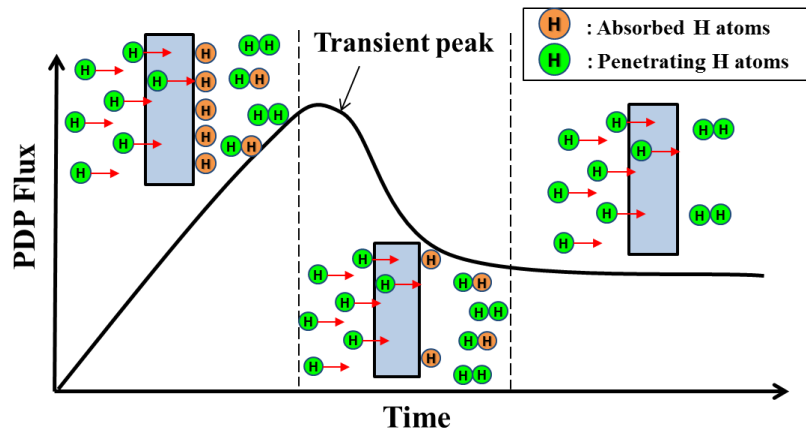


Figure 3.28 A schematic diagram for the possible mechanism of the transient peak.

3.7.2. Compound surface condition effects on PDP

In Section 3.6, the surface contamination and surface area effects have been investigated separately. Notice that these two surface effects are independent on each other, which means these two effects may be multiplied. The surface area modified sample with 1 mm deep groove (shown in Fig. 3.26) has been oxidized at ~500 °C for 4.5 h and then exposed to hydrogen plasma again. The oxygen pressure is $\sim 1.3 \times 10^{-2}$ Pa.

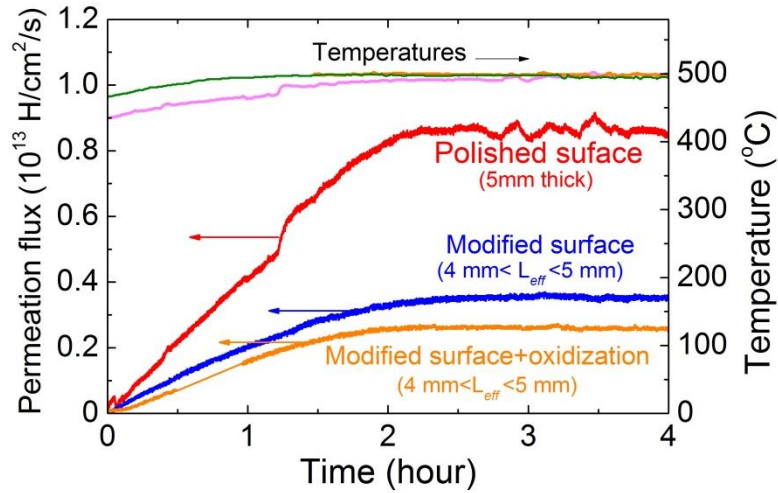


Figure 3.29 The compound surface condition effects on PDP.

Figure 3.29 shows that a further reduction of hydrogen permeation has been observed. The steady-state permeation flux has been found to be lower than that of the sample before oxidization by a factor of 1.4, which is in good agreement with the separate surface contamination effect experimental data shown in Fig. 3.23. Compared with the clean and polished surface, the overall permeation flux has been found to be reduced by a factor of ~ 3.2 .

3.7.3. Comparison of hydrogen PDP and GDP through F82H.

Shown in Fig. 3.30 are the hydrogen PDP and GDP fluxes at ~ 500 °C through a 5 mm F82H membrane with a polished surface, measured in separate experiments. The hydrogen implantation flux and energy for PDP are 2×10^{16} H/cm²/s and 100 eV, respectively. The gas pressure for GDP is $\sim 10^4$ Pa, which is relevant to the FLiBe breeder condition. It has been found that the steady state hydrogen permeation flux from GDP is overwhelmingly larger than that from PDP, which suggests that tritium may flow into the vacuum chamber by gas-driven permeation and increase the first wall recycling.

Using the data taken in the separate PDP and GDP experiments, the hydrogen recycling rate has been estimated to be $R = 1.025$. Assuming a first wall area of 3000 m² for a large-

scale DEMO reactor (the FFHRd1 case [18]), the uncontrollable gas fueling rate is to be $\sim 6 \times 10^4$ Pa l/s, which is certainly not desirable from the point of view of achieving high-confinement via plasma-wall boundary control, i.e. reduced edge particle recycling.

However, it should be pointed out that the hydrogen gas pressure used in the GDP experiment is the equilibrium tritium partial pressures in FLiBe at 800 K, as shown in Fig. 1.6. The actual tritium pressure would be related to the breeder flow rate, the tritium recovery rate and the breeder temperature, etc. Further details on this bi-directional issue are presented in Chapter 5 and Chapter 6.

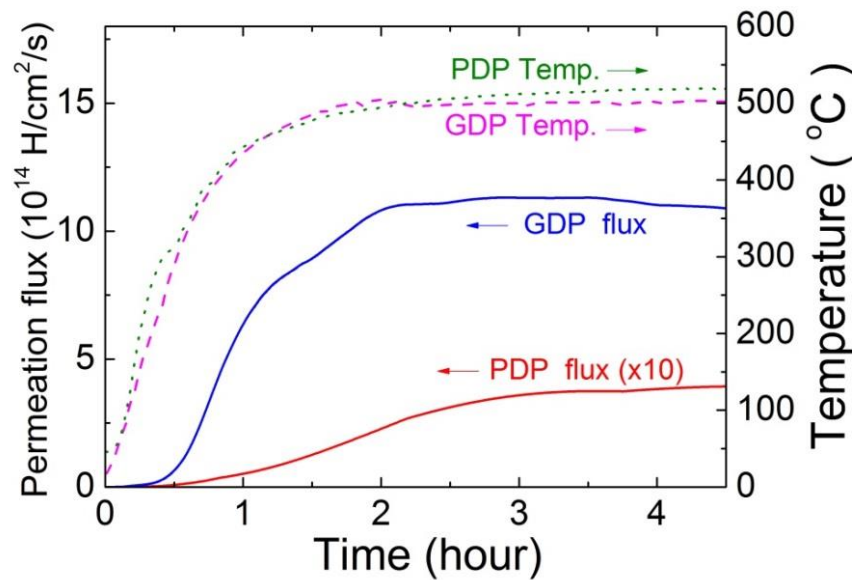


Figure 3.30 Hydrogen PDP and GDP behavior through a 5 mm thick F82H at ~ 500 °C.

3.8. Summary

Gas- and plasma-driven permeation through a reduced activation steel alloy F82H has been investigated using a steady state laboratory-scale plasma device: VEHICLE-1. The hydrogen transport parameter data taken for SUS304 have been found to be in good agreement with the literature data, which means that the experimental setup on VEHICLE-1 is valid for the evaluation of other first wall candidate materials.

Hydrogen transport parameters like permeability, diffusion coefficient, Sieverts' constant and recombination coefficient have been measured for F82H. Both GDP and PDP have been found to be diffusion-limited under all the conditions examined in the present study.

The surface effects on hydrogen PDP have been investigated from two aspects: surface contamination and morphology. Thick surface impurity film has been found to act as a second layer for diffusion and reduce the permeation. A decrease in steady state permeation flux has been measured when increasing plasma-facing surface area, which is in agreement with the theoretical prediction, i.e., the steady state permeation flux is inversely proportional to the square root of surface area. Experiments indicate that the permeation flux can be further reduced by simultaneous surface oxidization and machining

From these separate GDP and PDP experiments, one would expect that gas-driven permeation would dominate hydrogen isotopes transport through the first wall for blankets employing self-cooled breeders that exhibit relatively high dissociation pressures of tritium. Such tritium back-flow into the vacuum chamber may result in an unwanted increase in edge plasma density. When bi-directional PDP and GDP take place simultaneously, the permeation behavior may be affected by isotope effect as well (See section 2.3 in Chapter 2). Further investigation on the bi-directional permeation issue has been done and the results are presented in Chapter 5 and Chapter 6.

Reference

- [1] Y. Hirooka et al., *A new versatile facility: Vehicle-1 for innovative PFC concepts evaluation and its first experiments on hydrogen recycling from solid and liquid lithium*, Journal of Nuclear Materials 337-339 (2005) 585.
- [2] E. M. Hollmann et al., *Measurement and modeling of molecular ion concentrations hydrogen reflex-arc discharge*, Physics of Plasmas 9 (2002) 4330.
- [3] A. Tonegawa et al., *Observation of molecular assisted recombination via negative ions formation in a divertor plasma simulator, TPDSHEET-IV*, Journal of Nuclear Materials 313- 316 (2003) 1046.
- [4] R. K. Janev et al., *Elementary Processes in Hydrogen–Helium Plasmas*, Springer-Verlag, Berlin Heidelberg (1987).
- [5] H. Kimura et al., *Progress of advanced material tokamak experiment (AMTEX) program on JFT-2M*, Fusion Engineer and Design 56–57 (2001) 837.
- [6] A. Konishi, master thesis, in Japanese, 2013.
- [7] S. Fukada et al., *Tritium recovery system for Li–Pb loop of inertial fusion reactor*, Fusion Engineer and Design 83(2008) 747.
- [8] K. Katsuta and K. Furukawa, *Hydrogen and deuterium transport through type 304 stainless steel at elevated temperatures*, Journal of Nuclear Science and Technology, 18 (1981) 143.
- [9] X. Sun et al., *Hydrogen permeation behaviour in austenitic stainless steels*, Materials Science and Engineering, A114 (1989) 179.
- [10] E. Serra et al., *Influence of traps on the deuterium behaviour in the low activation martensitic steels F82H and Batman*, Journal of Nuclear Materials 245 (1997) 108.

- [11] A. Pisarev et al., *Surface effects in diffusion measurements deuterium permeation through Martensitic steel*, Physica Scripta T94 (2001) 121.
- [12] T.V. Kulsartov et al., *Investigation of hydrogen isotope permeation through F82H steel with and without a ceramic coating of Cr₂O₃–SiO₂ including CrPO₄ (out-of-pile tests)*, Fusion Engineer and Design 81 (2006) 701.
- [13] J. Crank, *The Mathematics of Diffusion*, 2nd edition, Clarendon Press, Oxford, London, 1975.
- [14] M. A. V. Devanathan and Z. Stachurski, *The adsorption and diffusion of electrolytic hydrogen in palladium*, Proceedings of the Royal Society A 270 (1962) 90.
- [15] K.S. Forcy et al., *The diffusivity and solubility of deuterium in a high chromium martensitic steel*, Journal of Nuclear Materials 240 (1997) 118.
- [16] R. A. Oriani, *The diffusion and trapping of hydrogen in steel*, Acta Metallurgica 18 (1970) 147.
- [17] V. Shestakov et al., *Gas driven deuterium permeation through F82H martensitic steel*, Journal of Nuclear Materials 307-311 (2002) 1494.
- [18] A. Sagara, et al., *Design activities on helical DEMO reactor FFHR-d1*, Fusion Engineering and Design 87 (2012) 594.
- [19] J. F. Ziegler et al., *SRIM – The stopping and range of ions in matter (2010)*, Nuclear Instruments and Methods in Physics Research Section B, 268 (2010)1818.
- [20] Möller and J. Roth, *Physics of Plasma-Wall Interaction in Controlled Fusion Devices*, Plenum Press, New York, 1986, p. 439–494.
- [21] T. Nagasaki et al, *Ion-driven permeation and surface recombination coefficient of deuterium for ion*, Journal of Nuclear Materials 202 (1993) 228.

- [22] M.I. Baskes, *A calculation of the surface recombination rate constant for hydrogen isotopes on metals*, Journal of Nuclear Materials 92 (1980) 318.
- [23] S. Hirata et al., JAEA report, JAERI-M-91-081.
- [24] B.L. Doyle, *A simple theory for maximum H inventory and release: a new transport parameter*, Journal of Nuclear Materials 111&112 (1982) 628.
- [25] Y. Hirooka et al., *Materials surface modification by plasma bombardment under simultaneous erosion and redeposition conditions*, Nuclear Instruments and Methods in Physics Research Section B23 (1987) 458.
- [26] H. Zhou et al., *Hydrogen plasma-driven permeation through a reduced activation ferritic steel alloy F82H*, Fusion Science and Technology T63 (2013) 361.
- [27] R. A. Causey et al., *The effect of surface composition on plasma driven permeation of deuterium through 304 stainless steel*, Journal of Nuclear Materials 122&123 (1984) 1547.
- [28] A. I. Livshits et al., *Plasma driven superpermeation of hydrogen through group Va metals* Journal of Applied Physics 84 (1998) 2558.
- [29] O. V. Ogorodnikova, et al., *Tritium permeation through the first wall of the EU-HCPB Blanket*, Fusion Engineer and Design 49-50 (2000) 921.
- [30] M. Takizawa et al., *Surface condition effects on plasma driven permeation*, Journal of Nuclear Materials 248 (1997) 15.
- [31] Y. Hirooka and H. Zhou, *Laboratory experiments and modeling on bi-directional hydrogen isotopes permeation through the first wall of a magnetic fusion DEMO reactor*, Fusion Science and Technology 66 (2014) 63.
- [32] Y. Hatano et al, *Influence of surface impurities on plasma-driven permeation of deuterium through nickel*, Vacuum Science and Technology, A16 (1998) 2078.

- [33] H. Zhou et al., *Bi-directional hydrogen permeation through F82H under DEMO-relevant conditions*, Plasma and Fusion Research 8 (2013) 2402065.
- [34] R. A. Causey, *Hydrogen isotope retention and recycling in fusion reactor plasma-facing components*, Journal of Nuclear Materials 300 (2002) 91.
- [35] J. F. Ziegler et al., *SRIM - The stopping and range of ions in matter (2010)*, Nuclear Instruments and Methods in Physics Research, B12 (2010) 1818.
- [36] J. Winter et al., *Permeation probes for the characterization of the atomic hydrogen flux to a tokamak wall*, Journal of Nuclear Materials 111/112 (1982) 243.

Chapter 4

Plasma-driven permeation through F82H in QUEST

As presented in the previous chapter, hydrogen transport parameters like permeability, diffusion coefficient and surface recombination coefficient have been measured for F82H. Using this well-investigated material as a permeation probe, it's possible to measure the incoming hydrogen flux to the first wall in a fusion device. Presented in this chapter are the results of the measurements using an F82H permeation probe in the QUEST spherical tokamak during conditioning steady state discharges heated with 2.45 GHz and 8.2 GHz electron cyclotron resonance (ECR). In these proof-of-principle experiments, the F82H permeation probe shows a good sensitivity to the variation of plasma parameters.

4.1. QUEST spherical tokamak

QUEST (Q-shu University Experiment with Steady State Spherical Tokamak, as shown in Fig 4.1) is a medium size spherical tokamak (ST) which aims to achieve the steady state operation of ST with the capability to attain high β rather than conventional tokamaks [1]. The major radius and the minor radius of QUEST are $R = 0.68$ m and $a = 0.36$ - 0.4 m, respectively [2].

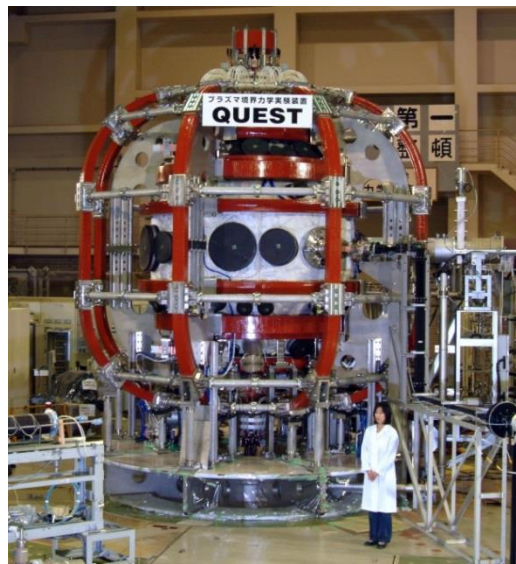


Figure 4.1 The QUEST spherical tokamak [3].

The vacuum chamber of QUEST is made of stainless steel 304 L with a wall thickness of 8-12 mm. The chamber radius and height are ~ 1.4 m and ~ 2.8 m, respectively. The total surface area of the chamber wall is ~ 35.5 m² and the volume is ~ 13 m³ including the extension ports. Outboard limiters made of tungsten are installed on the outside walls at a major radius of $R = 1.35$ m. Fuelling gas injectors are located at the outside wall and the center stack at the mid-plane. The pumping system for the QUEST chamber, which consists of a turbo-molecular pump and 3 cryopumps, has a pumping speed of 3.8 m³·s⁻¹. Hydrogen plasmas are produced using ECR with three kinds of RF sources: 2.45 GHz, 8.2 GHz and 28 GHz.

4.2. Permeation experimental setup in QUEST

In the present work, hydrogen plasma-driven permeation experiments have been performed for the low temperature, low density slab plasmas in discharge cleaning experiments using the 2.45 GHz and the 8.2 GHz sources. The slab plasma means plasmas produced in the electron cyclotron resonance region without poloidal field (i.e., no closed flux surfaces and the plasma current $I_p \approx$ a few kA, as shown in Fig. 4.2).

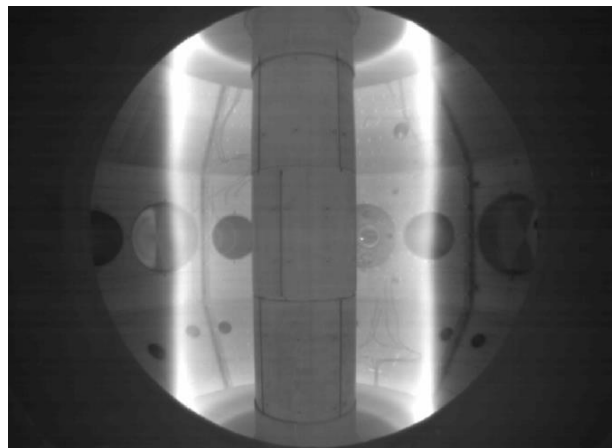


Figure 4.2 A plasma without closed flux surfaces in QUEST [2].

Shown in Fig. 4.3 are a schematic diagram of the probe position and the PDP setup in QUEST. The permeation probe has been installed near the mid-plane and the permeation membrane is 35 mm away from the outboard wall in the radial direction (Fig. 4.3 (a)). A resistive heater is set behind the sample so that the membrane temperature can be kept in a range of 240-300 °C. The temperature is measured by a thermocouple attached to the downstream surface. The hydrogen partial pressure is measured by a quadrupole mass spectrometer (QMS), which has been calibrated by a hydrogen standard leak, as shown in Fig. 4.3(b).

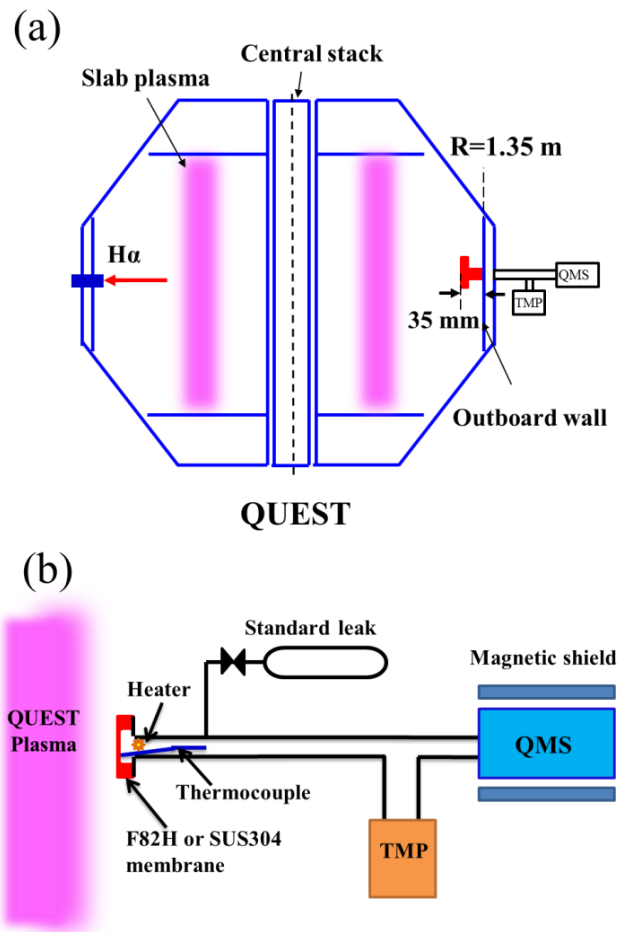


Figure 4.3 Schematic diagrams of (a) the permeation probe setup in QUEST and (b) the details of the permeation flux measurement system.

Samples made of F82H and SUS304 are prepared in the same dimensions as those commercially available conflat flanges with an outer diameter of 34 mm, except that a circular area of ~16 mm in diameter inside the knife-edge is machined down to thicknesses of 0.14 to 0.5 mm, as shown in Fig.4.4. The samples are also cut from the F82H plates used in the JFT-2M tokamak at JAERI (now JAEA) [4], i.e., the sample membranes for QUEST experiments are prepared in the same way as those used in VEHICLE-1. Assuming the surface conditions of all the samples are the same, the hydrogen transport parameters taken in laboratory experiments can be used to analyze the measurement results in QUEST. The stainless steel sample is used as a comparative reference.

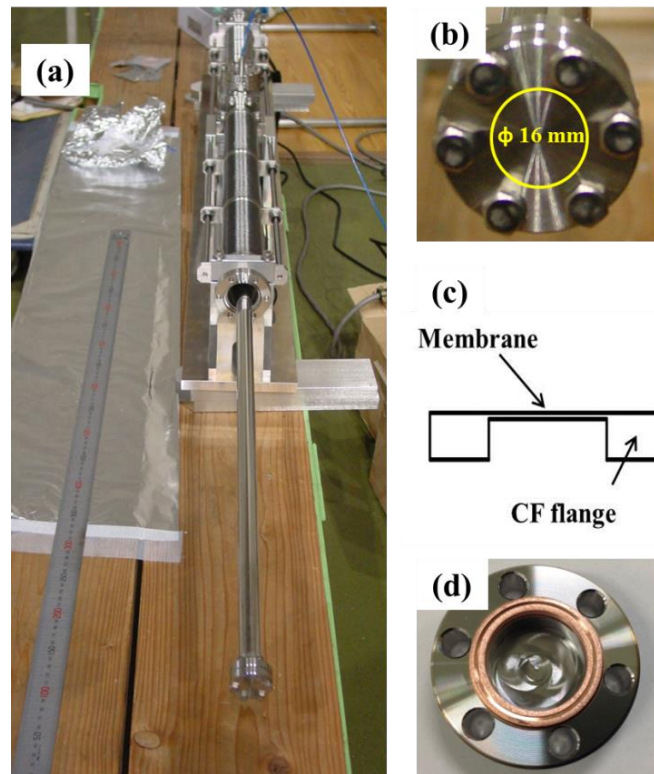


Figure 4.4 (a) The permeation probe with a flange-type sample membrane, (b) the dimension of the membrane, (c) a schematic view of the sample and (d) the downstream side of the sample membrane (with a copper gasket).

After the permeation experiments, the membrane surfaces are analyzed by energy dispersive X-ray spectroscopy (EDX) and X-ray photoelectron spectroscopy (XPS). For XPS analysis, a 4 kV Ar+ gun is used to etch the sample surfaces so that the depth profile can be obtained.

4.3. Results and discussion

4.3.1. PDP through F82H and SUS304 membranes in QUEST

Figure 4.5 shows the hydrogen PDP data through a 0.2 mm thick F82H membrane exposed to a wall conditioning 900 s discharge. The plasma is produced by the 2.45 GHz RF system with an input power of 7.5 kW and the toroidal field coil current is kept at 17 kA. The steady state permeation flux for the F82H membrane has been measured to be $\sim 2.4 \times 10^{13}$ $\text{H} \cdot \text{cm}^{-2} \cdot \text{s}^{-1}$ at ~ 270 °C.

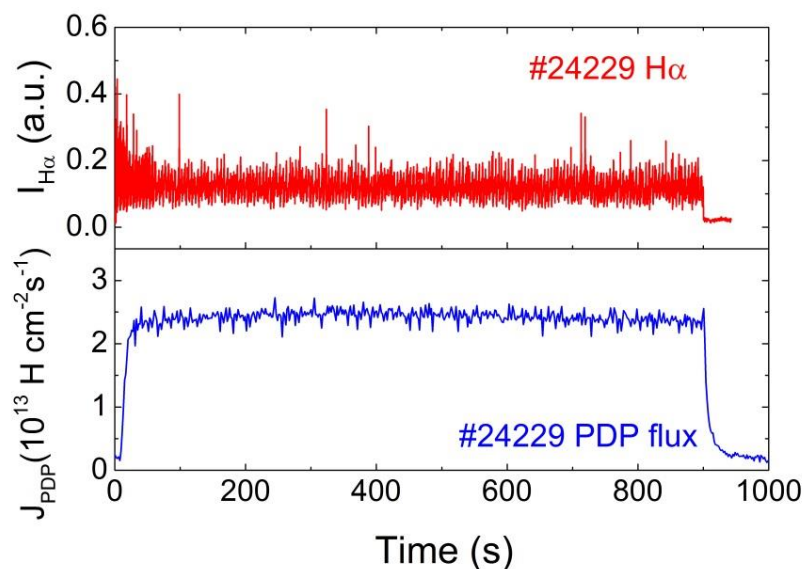


Figure 4.5 Plasma-driven permeation through a 0.2 mm thick F82H membrane at a temperature around 270 °C.

Shown in Fig.4.6 is a comparison of PDP behavior through 0.2 mm thick F82H and 0.14 mm thick SUS304 membranes. It can be seen that the permeation flux through the F82H membrane can reach steady state within 100 s. For SUS304, in contrast the permeation flux keeps increasing during the discharge, not reaching the steady state.

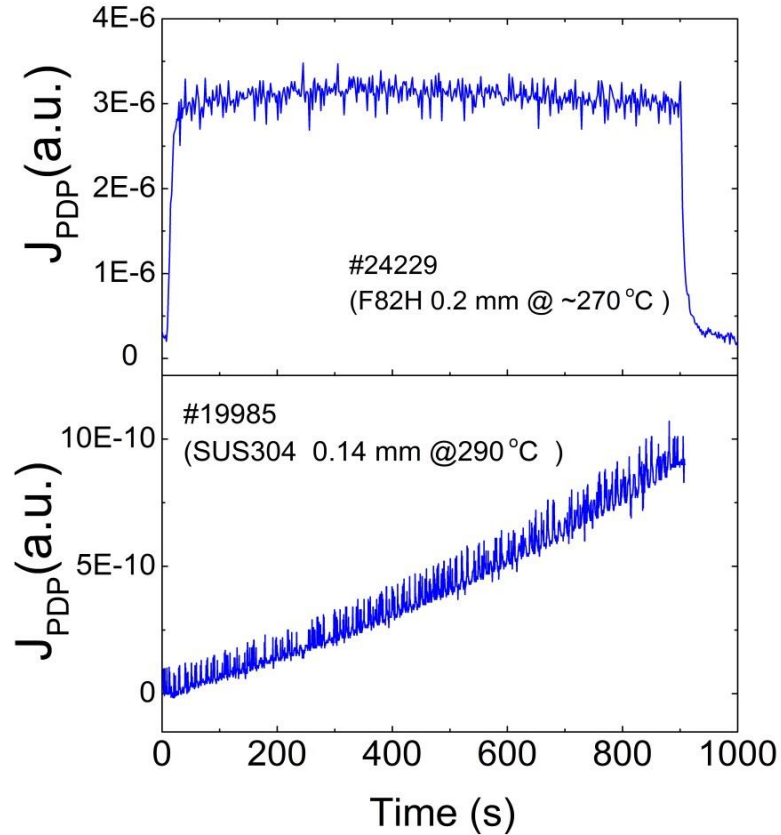


Figure 4.6 Comparison of PDP through F82H and SUS304 membranes in 900 s discharges.

Figure 4.7 shows the results of PDP through the SUS304 membrane in four continual discharges. The total exposure time is about 3600 s, but the permeation flux cannot reach steady state. These results are consistent with the experimental observation for the F82H and SUS304 membranes in VEHICLE-1, as presented in Section 3.7 of Chapter 3.

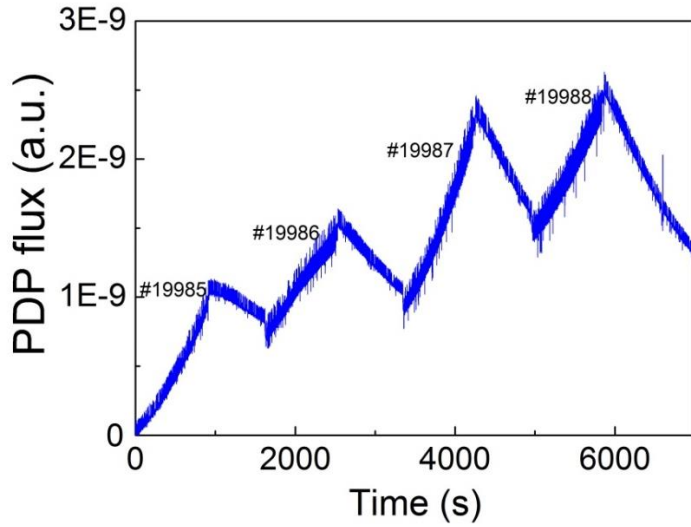


Figure 4.7 Plasma-driven permeation through a 0.14 mm thick SUS304 membrane in four continual 900 s discharges at ~ 290 °C.

As introduced in Section 2.2 of Chapter 2, three regimes are considered in the steady state plasma-driven permeation model, i.e., the diffusion-diffusion (DD) limited regime, the recombination-diffusion (RD) limited regime and the recombination-recombination (RR) limited regime. The rate controlling process can be characterized by the dimensionless parameter:

$$W = \frac{d}{D} (J_0 K_r)^{1/2}. \quad (2.14)$$

The diffusion and recombination coefficients for F82H have been calculated from the VEHICLE-1 data to be:

$$D = 7.5 \times 10^{-4} \exp\left(\frac{-0.14 \text{ [eV]}}{kT}\right) \quad (3.16)$$

and

$$K_r = 4.8 \times 10^{-21} \exp\left(\frac{0.48 \text{ [eV]}}{kT}\right) \quad (3.19)$$

respectively. Table 4.1 shows the calculation results of W in the temperature range of the PDP experiments, which indicates that PDP through the F82H is in the RD-regime ($d/L < W < 1$, where d is the implantation range and L is the membrane thickness. The surface conditions for the front surface and back surface are assumed to be the same.), i.e., recombination-limited at the front surface and diffusion-limited inside the bulk.

Table 4.1 Calculation results of W at various temperatures

Temperature (°C)	D (cm ² s ⁻¹)	Kr (cm ⁴ s ⁻¹)	W
200	2.4×10^{-5}	6.0×10^{-16}	0.1016
220	2.8×10^{-5}	3.8×10^{-16}	0.0696
240	3.2×10^{-5}	2.4×10^{-16}	0.0491
260	3.6×10^{-5}	1.6×10^{-16}	0.0356
280	4.0×10^{-5}	1.1×10^{-16}	0.0264
300	4.4×10^{-5}	7.8×10^{-17}	0.0200

Using Eq. (3.13) and the diffusivity data for stainless steel [5], the diffusion distances \sqrt{Dt} have been estimated to be 1.9 mm for F82H and 0.019 mm for SUS304 in 900 s at 290 °C, which can explain their different permeation behavior shown in Fig. 4.6. The calculation result is also in agreement with the trend that hydrogen can transport faster in bcc

metals (e.g., ferritic steels) than in fcc metals (e.g., SUS304) [6].

4.3.2. Effect of plasma heating power

Shown in Fig.4.8 are the $H\alpha$ intensity and permeation flux data for two 900 s discharges with different heating methods. The long-pulse plasmas are maintained by the 2.45 GHz RF source with a power of 4 kW. For shot #21446, additional 8.4 GHz ECR heating (25 kW, 0.4s width) is conducted throughout the discharge with a frequency of 0.1 Hz. Permeation flux measurements show that without 8.2 GHz RF heating, the steady-state PDP flux decreases by $\sim 13\%$ for F82H. Due to the lack of plasma temperature and density data, the time-integrated $H\alpha$ intensity ($Q_{H\alpha}$) is used as a measure to estimate the particle flux to the wall (J_0) [7].

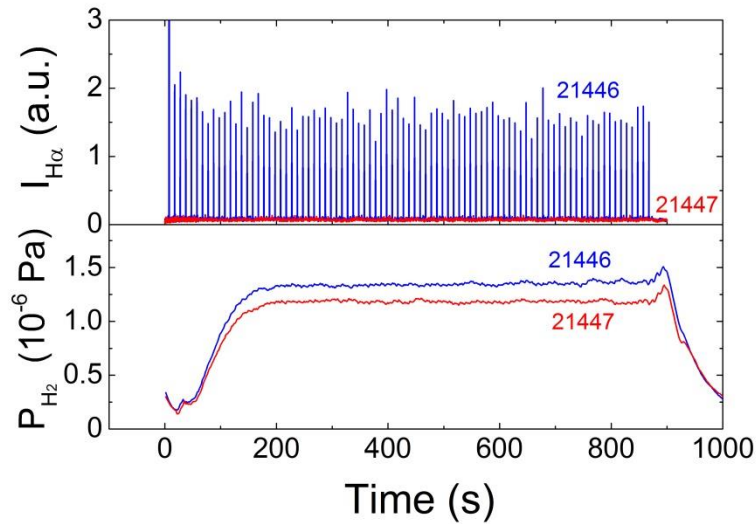


Figure 4.8 PDP through a 0.5 mm thick F82H membrane w/ and w/o the 8.2 GHz RF plasma heating source.

Figure 4.9 shows the time-integrated $H\alpha$ intensities and the PDP fluxes. At $t=900$ s, where t is the time, the value of $(Q_{H\alpha})^{1/2}$ for shot #21446 is higher than that of shot #21447 by a factor of ~ 1.41 , while the permeation flux (J_+) ratio of the two discharges is ~ 1.13 . Data roughly agree with the theoretical prediction for the permeation flux J_+ [$\text{atom}\cdot\text{cm}^2\cdot\text{s}^{-1}$] when

plasma-driven permeation takes place in the RD-regime:

$$J_+ = \frac{D}{L} \sqrt{\frac{J_0}{K_r}}, \quad (2.16)$$

i.e., the steady state permeation flux is proportional to the square root of the implantation flux.

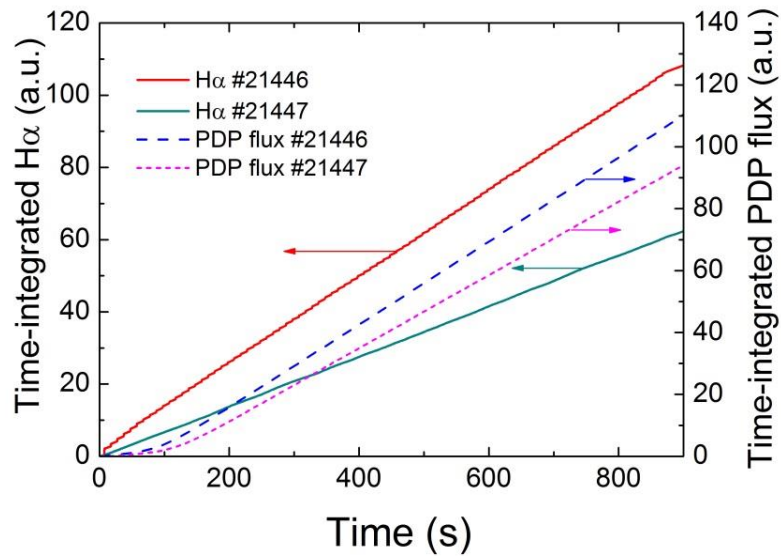


Figure 4.9 The time-integrated H α intensities and PDP fluxes for the #21446 and #21447 shots.

4.3.3. Diffusivity measurements for F82H from the PDP data taken in QUEST

The diffusivity for hydrogen through a metal can be obtained either by fitting the transient permeation curve (see Eq. (3.11) in Chapter3) or by measuring the time lag $t_l=L^2/6D$ [8] from the steady state permeation behavior. Figure 4.10 (a) and (b) shows the calculation examples for diffusion coefficient by the two methods, respectively.

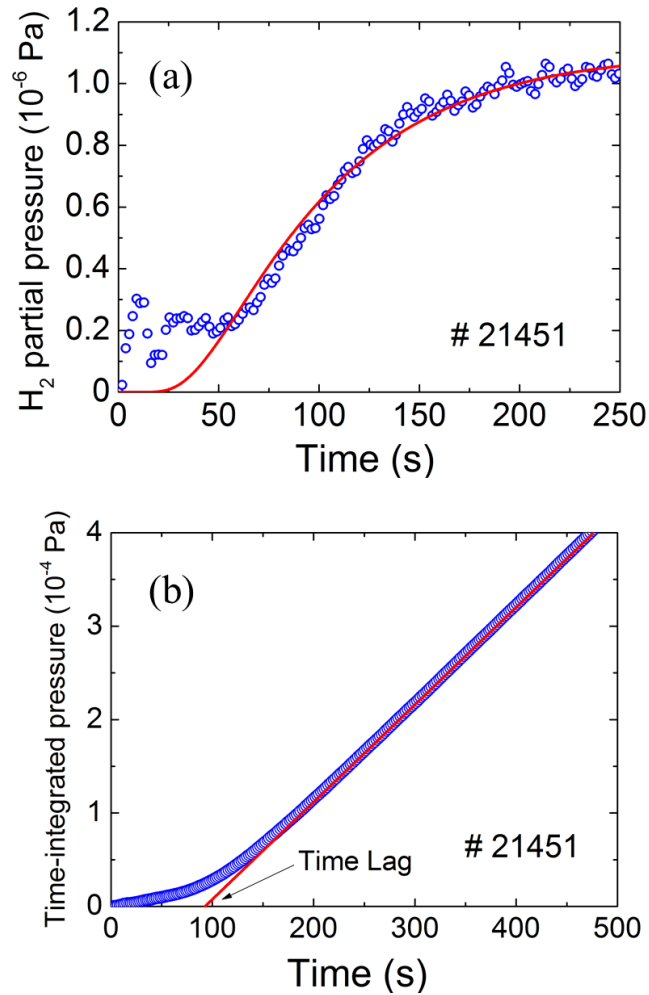


Figure 4.10 Diffusion coefficient calculations (a) by fitting the transient permeation curve and (b) by measuring the time lag for the #21451 shot.

Shown in Fig.4.11 are the effective diffusivity data measured for F82H in the PDP experiments in QUEST. The previous VEHICLE-1 data and Serra's data [9] are shown for comparison. It has been found that the diffusion coefficients estimated from the QUEST data

are lower by a factor of 3 to 4 than those taken in VEHICLE-1, although the sample membranes are essentially the same.

As presented in Section 3.6 of Chapter 3, hydrogen PDP has often been observed to be enhanced by surface contaminations because recombination release is suppressed by the presence of impurities. However, it is also true that if the contaminated layer becomes thick enough to act as a second layer for diffusion [10,11]. One possible reason for the lower measured diffusivity is that the membrane surface is contaminated during the PDP experiments in QUEST. The impurity layer with smaller hydrogen diffusion coefficient may act as a second layer for diffusion.

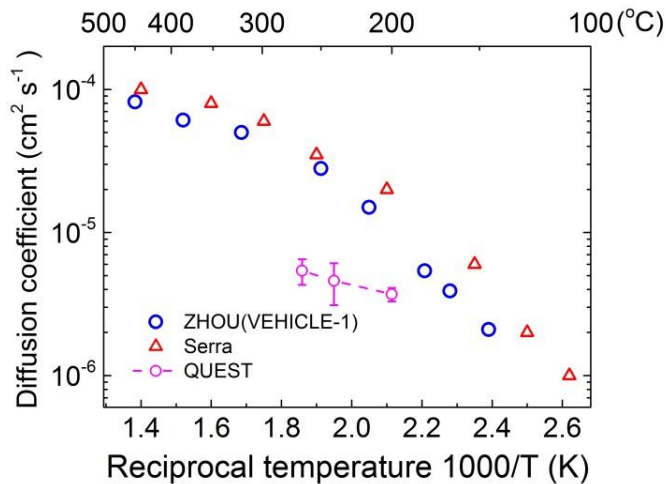


Figure 4.11 Effective diffusivity measurements for F82H in QUEST. The previous VEHICLE-1 data and Serra’s data [9] are shown for a comparison.

Figure 4.12 shows the surface analysis using X-ray photoelectron spectroscopy (XPS) for SUS304 and F82H membranes after the PDP experiments in QUEST. Impurities such as carbon, tungsten and oxygen have been detected on the membrane surface. Carbon deposition should be made during plasma exposures because contaminations from air

exposure can only affect the first several nm of the sample surface. Tungsten impurity should come from erosion and redeposition of the plasma-facing materials [12]. This conclusion can also be confirmed by the tungsten depth profile for SUS304, which does not contain any tungsten in the bulk.

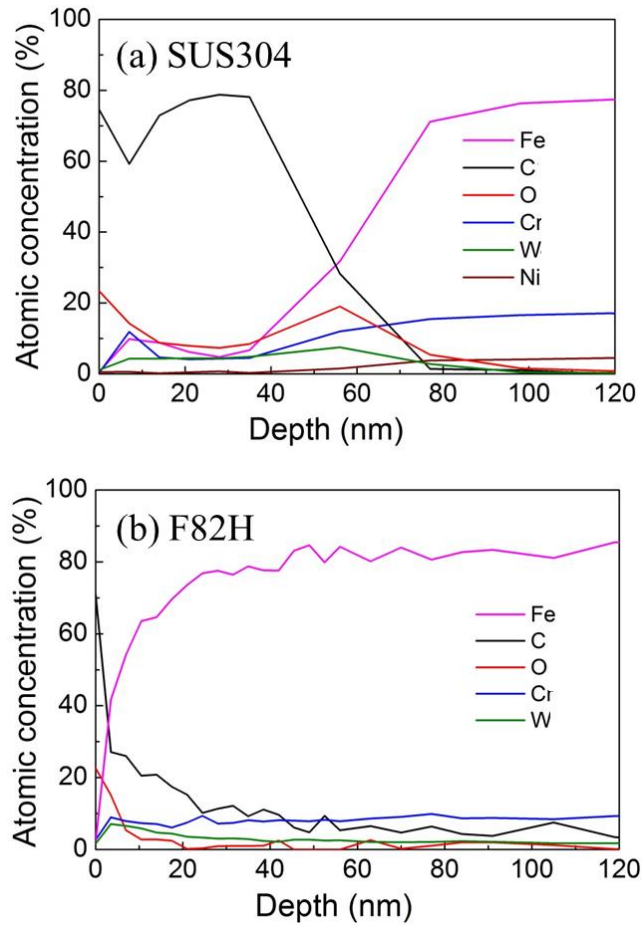


Figure 4.12 Surface composition analysis for (a) SUS304 and (b) F82H membranes after the PDP experiments in QUEST.

The thickness of the impurity layer on the F83H membrane has been estimated to be ~12 nm by XPS. A membrane composed of two sheets of thicknesses L_1 , L_2 and diffusion coefficients D_1 , D_2 has an effective diffusion coefficient D_{eff} , given by [13]:

$$L_1 / D_1 + L_2 / D_2 = L / D_{\text{eff}} \quad (4.1)$$

where L is the total thickness of the membrane. Using the diffusion coefficient data for F82H from previous experiments [19], the hydrogen diffusion coefficient in the impurity layer has been estimated to be $\sim 2 \times 10^{-10} \text{ cm}^2 \text{ s}^{-1}$. This value is close to the hydrogen diffusion coefficient for tungsten measured in the same temperature range [14], but lower than that of graphite by several orders of magnitude [15].

4.4. Summary

Plasma-driven permeation (PDP) measurements have been conducted in the QUEST spherical tokamak for F82H and SUS304. A much shorter PDP breakthrough time and higher steady-state permeation flux have been found for F82H than SUS304. The F82H permeation probe shows a good sensitivity to the variation of plasma parameters. However, the permeation flux measurements may be affected by the surface impurities accumulated in plasma discharges.

Reference

- [1] K. Hanada et al., *Steady-state operation scenario and the first experimental result on QUEST*, Proceedings of ITC18, (2008) I-18.
- [2] K. Sato et al., *Present Status of “QUEST” Project*, US-Japan WS on RF Physics in Fusion Plasma, 2010.3.8-10, San Diego.
- [3] <http://www.triam.kyushu-u.ac.jp/>
- [4] H. Kimura et al., *Progress of advanced material tokamak experiment (AMTEX) program on JFT-2M*, Fusion Engineer and Design 56–57 (2001) 837.
- [5] W. Möller and J. Roth, *Physics of Plasma-Wall Interaction in Controlled Fusion Devices*, Plenum Press, New York, 1986, p. 439–494.
- [6] J. Crank, *The Mathematics of Diffusion*, 2nd edition, Clarendon Press, Oxford, London, 1975.
- [7] S.K. Sharma et al., *Permeation measurements for investigating atomic hydrogen flux and wall pumping/fuelling dynamics in QUEST*, Journal of Nuclear Materials 420 (2012) 83.
- [8] M. A. V. Devanathan and Z. Stachurski, *The adsorption and diffusion of electrolytic hydrogen in palladium*, Proceedings of the Royal Society A 270 (1962) 90.
- [9] E. Serra et al., *Influence of traps on the deuterium behaviour in the low activation martensitic steels F82H and Batman*, Journal of Nuclear Materials 245 (1997) 108.
- [10] Y. Hirooka and H. Zhou, *Laboratory experiments and modeling on bi-directional hydrogen isotopes permeation through the first wall of a magnetic fusion DEMO reactor*, Fusion Science and Technology 66 (2014) 63.

- [11] Y. Hatano et al., *Influence of surface impurities on plasma-driven permeation of deuterium through nickel*, Journal of Vacuum Science & Technology A 16 (1998) 2078.
- [12] S.K. Sharma et al., *Analysis of PWI footprint traces and material damage on the first walls of the spherical tokamak QUEST*, Fusion Engineer and Design 87 (2012) 77.
- [13] J. Crank, *The Mathematics of Diffusion*, 2nd ed., Clarendon Press, Oxford, London, 1975.
- [14] T. Otsuka et al., *Hydrogen diffusion profile in tungsten by using a tritium imaging plate technique –determination of diffusion coefficient in W*, Physica Scripta T138 (2010) 014052.
- [15] R. Causey et al., *Tritium Barriers and Tritium Diffusion in Fusion Reactors*, in *Comprehensive Nuclear Materials*, 1st edition, Elsevier, 2012.

Chapter 5

Bi-directional hydrogen (H) permeation experiments and modeling

5.1. Introduction

Separate plasma-driven permeation and gas-driven permeation experiments have been presented in Chapter 3 and Chapter 4. For the hydrogen isotopes permeation through the first wall, a fundamental materials science question that needs to be addressed is: can plasma-driven and gas-driven permeation of hydrogen isotopes in the two counter directions actually take place under fusion reactor relevant conditions? Experiments and simulation studies have been done to answer the question. In this chapter, the data taken from the first-of-a-kind bi-directional hydrogen PDP and GDP experiments and relevant DIFFUSE-code calculation are presented.

5.2. Experimental methods

Details of the experimental setup in the steady-state linearly-magnetized ECR-plasma facility: VEHICLE-1 have already been presented in Chapter 3. For completeness, some of the important features of the bi-directional experiments will be described in this section.

Shown in Fig. 5.1 is a schematic diagram of the bi-directional permeation setup in VEHICLE-1. Different from the GDP setup shown in Fig 3.2, an orifice has been installed so that a quadrupole mass spectrometer (QMS) can measure the H_2 partial pressure in the VEHICLE-1 main chamber within the operational pressure. F82H membranes are fixed in such a way that the upstream surface is exposed to hydrogen plasma, while the other side is exposed to hydrogen gas. The sample membrane can be heated up to >500 °C by plasma bombardment and heat from a heater. The plasma-facing side of the membrane is monitored by an optical spectrometer. The electron temperature is raised up to ~ 10 eV for the improved sensitivity of H_α spectroscopy. Under such experimental conditions, if the recycling condition of the membrane surface changes, variation in H_α intensity and hydrogen partial pressure are expected to be detected. At the gas side, the hydrogen gas pressure is measured by an absolute pressure gauge.

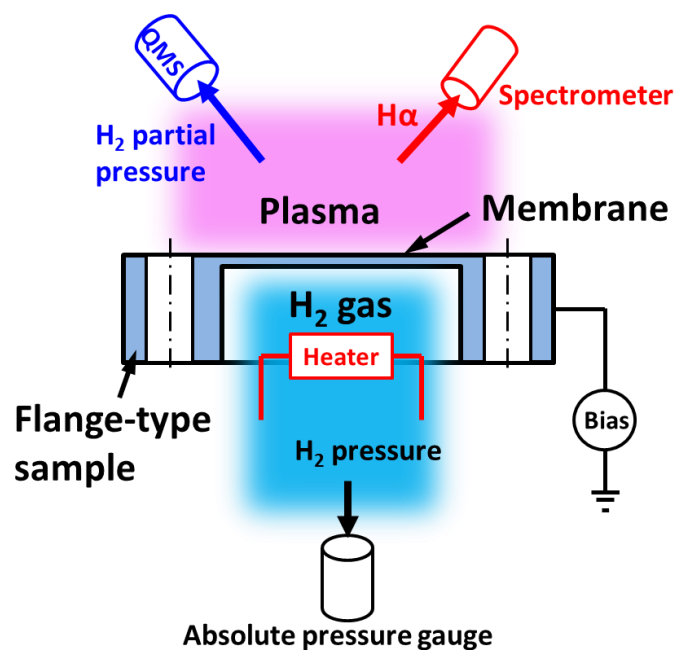


Figure 5.1 A schematic diagram of the bi-directional permeation setup in VEHICLE-1.

5.3. Hydrogen gas-driven permeation into Ar and He plasmas

As a first step to verify whether hydrogen would flow into the plasma side by gas-driven permeation through the first wall, experiments on hydrogen GDP into argon (Ar) and helium (He) background plasmas have been performed.

Shown in Fig. 5.2 are the data taken by the QMS and the visible spectroscopy for GDP hydrogen that flows into the background Ar plasma at the membrane temperatures of ~ 540 °C and ~ 490 °C on the gas-facing and plasma-facing sides, respectively. The membrane is first exposed to Ar plasma. Then hydrogen with a pressure of 9.3×10^4 Pa is introduced from a gas cylinder into the closed volume, indicated as the H₂ gas side in Fig.5.1. After the H _{α} signal becomes stable, hydrogen is pump out again. The membrane thickness is 0.6 mm and the ion bombarding energy is set at 50V.

Figure 5.3 shows the flux and H_{α} intensity for GDP hydrogen that flows into the background He plasma at the membrane temperatures of ~ 580 °C and ~ 560 °C on the gas-facing side and the plasma-facing side, respectively. The bias on the sample is set at 100V. This is to simulate the difference between H^{+} and He^{2+} , the latter of which is the species likely to be seen in the edge of DT-burning plasmas.

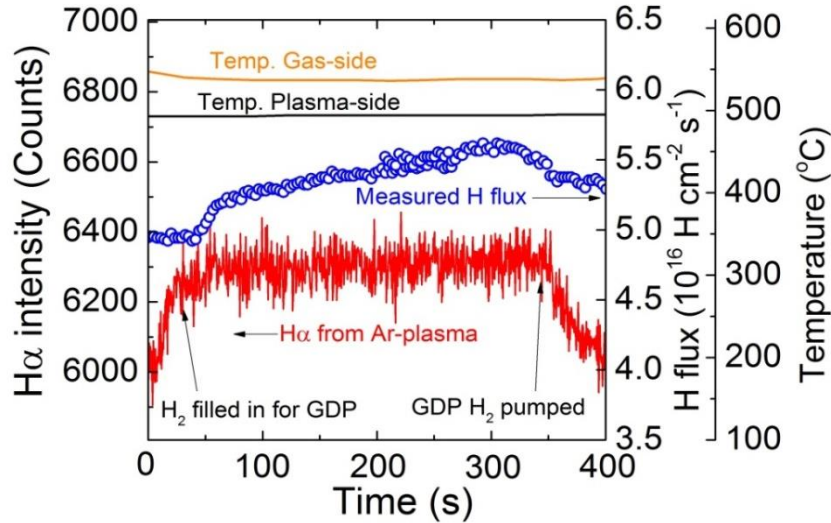


Figure 5.2 GDP flux and H_{α} -signal measured in the upstream Ar plasma side.

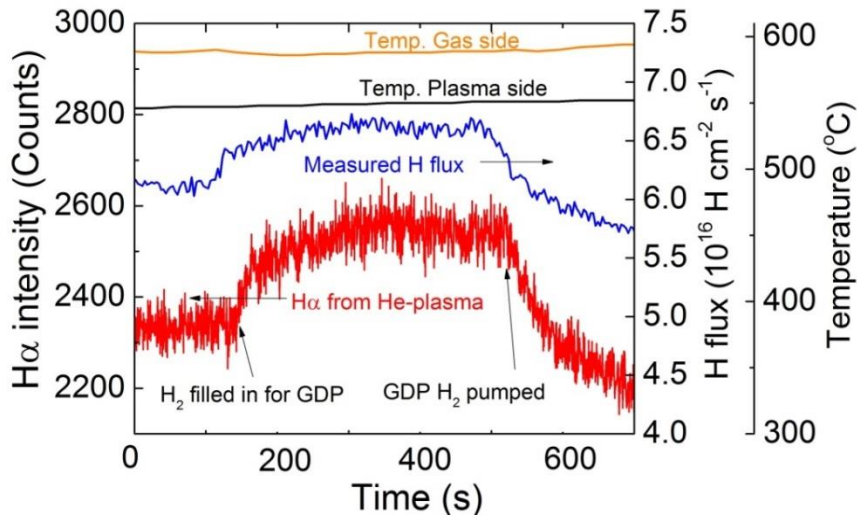


Figure 5.3 GDP flux and H_{α} -signal measured in the upstream He plasma side.

Recognize that the hydrogen permeation flux from GDP and H_{α} signal nicely keep track of each other from the initial gas fill-in to the pump-out of hydrogen at the downstream side. The GDP hydrogen flow rate in this experiment has been estimated to be $\sim 4 \times 10^{15}$ H-atoms/cm²/s for Ar background plasma and $\sim 5.2 \times 10^{15}$ H-atoms/cm²/s for He background plasma, respectively. These hydrogen permeation fluxes have been measured to be smaller than the value predicted using the hydrogen transport parameters measured for F82H in other experiments described in Chapter 3. The difference may be due to the measurement error and/or the radiation damage introduced by Ar/He ion bombardment, which has recently been observed for tungsten [1].

5.4. Hydrogen gas-driven permeation into hydrogen plasma side

Employing the same experimental conditions as described in the previous section, GDP hydrogen has been identified in the upstream hydrogen plasma, as shown in Fig.5.4. In this case, the ion bombarding energy is set at 50 V. Also, the temperatures on the gas-facing and plasma-facing sides are ~ 580 °C and ~ 550 °C, respectively. Taking into account the ion species mix in the low temperature hydrogen plasma and the particle reflection at the plasma-facing surface, the net implantation flux is estimated to be $\sim 8.5 \times 10^{15}$ H-atoms/cm²/s.

Note that the P_{H_2} and H_{α} signals keep track of each other, similar to those shown Fig. 5.2 and Fig. 5.3. Also seen here is the initial transient kick-up, which is exhibited by both P_{H_2} and H_{α} , presumably due to ion-induced desorption or thermal desorption, although the detail is unclear at this point. The GDP hydrogen flow rate in this case has been evaluated to be about 9.9×10^{15} H-atoms/cm²/s, which is in excellent agreement with the value 9.5×10^{15} H-atoms/cm²/s predicted by the GDP hydrogen transport model using parameters measured for F82H in other experiments shown in Chapter 3.

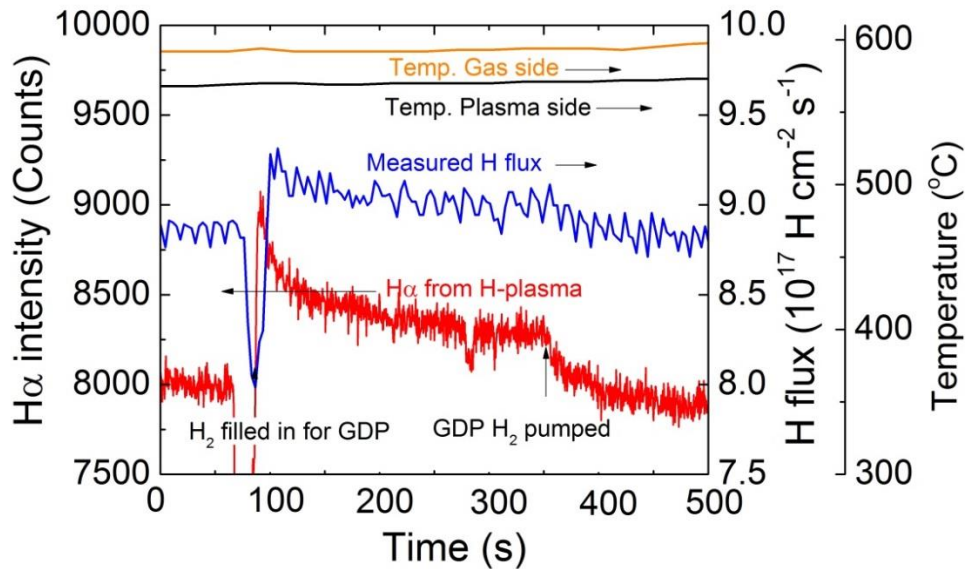


Figure 5.4 Hydrogen flux and H_{α} signals detected in the upstream hydrogen plasma in VEHICLE-1. The membrane thickness is 0.6 mm.

Edge plasmas have been found to be affected by the hydrogen GDP backflow into the plasma side. Shown in Fig. 5.5 is bi-directional hydrogen permeation through a 1 mm thick F82H membrane at a temperature of ~ 570 °C. The membrane is first exposed to hydrogen plasma, in which case only PDP takes place. Then hydrogen is introduced from a gas cylinder into the closed volume to a pressure of 10^5 Pa. After the H_{α} signal becomes stable, hydrogen is pumped out again. Langmuir probe measurements are performed before and after introducing hydrogen into the GDP volume. The plasma density is found to increase from $4.4 \times 10^9 \text{ cm}^{-3}$ to $5.7 \times 10^9 \text{ cm}^{-3}$, while the electron temperature decreases from 11.5 eV to 9.8 eV. These data indicate that GDP can take place in the opposite direction of PDP and increase in first wall recycling.

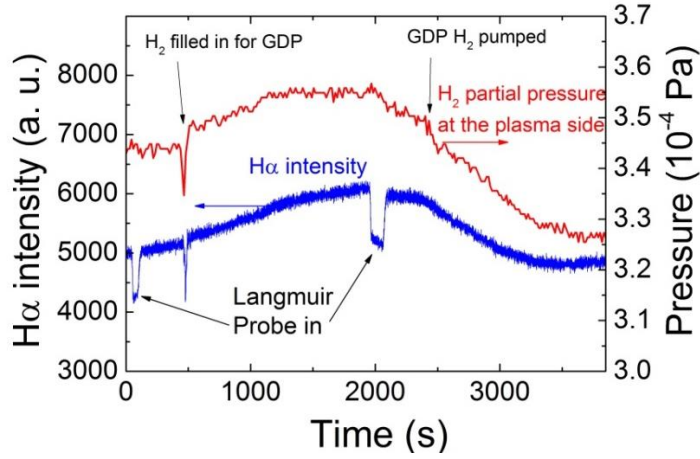


Figure 5.5 H₂ partial pressure and H_α intensity measured in the upstream hydrogen plasma in VEHICLE-1. The membrane thickness is 1 mm.

5.5. DIFFUSE-code calculation for the hydrogen GDP flow

5.5.1. DIFFUSE-code

The DIFFUSE-code [2] can predict the behavior of hydrogen PDP and GDP through a solid with trapping sites, solving numerically the following one-dimensional Fick's diffusion equations as shown in Chapter 2:

$$\frac{\partial C(x,t)}{\partial t} = D(T) \frac{\partial^2 C(x,t)}{\partial x^2} - \frac{\partial C_t(x,t)}{\partial t} + G(x,t) \quad (2.6)$$

$$\frac{\partial C_t(x,t)}{\partial t} = D(T) \frac{C(x,t)C_t^e(x,t)}{\lambda^2} - C_t(x,t)\nu_0 \exp(-U_t/kT) \quad (2.7)$$

$$C_t^e(x,t) = C_t^0(x) - C_t(x,t) \quad (2.8)$$

where $C(x,t)$ and $C_t(x,t)$ are the concentrations of mobile and trapped atoms as a function of position x and time t (See Section 2.1.3 in Chapter 2 for more details).

5.5.2. Input data and assumptions for the bi-directional permeation calculations

To simulate the hydrogen bi-directional permeation behavior, the input data for DIFFUSE-code are the same as those set in the experiments, i.e., the membrane thickness is 0.6 mm, the implantation flux from the plasma is 8.5×10^{15} H-atoms/cm²/s and the driving pressure for GDP is 9.3×10^4 Pa, the temperatures on the gas-facing and plasma-facing sides are ~ 580 °C and ~ 550 °C, respectively.

Also used as part of the code input is the information from the PDP and GDP process properties database [3], including diffusion coefficients, solubility, recombination constants, de-trapping energies, etc. for selected fusion reactor materials. Unfortunately F82H is not included in this database. It's reasonable to use α -Fe as a surrogate of F82H in the present work because F82H is an iron-base alloy and its lattice structure is similar to that of α -Fe [4,5]. The recombination coefficients for F82H and α -Fe are close to each other at a temperature around 500 °C (See Fig. 3.19 in Chapter 3). The measured permeability data (as shown in Fig. 5.6), which is a combination of diffusivity and solubility, indicate the similarity of these two materials as well.

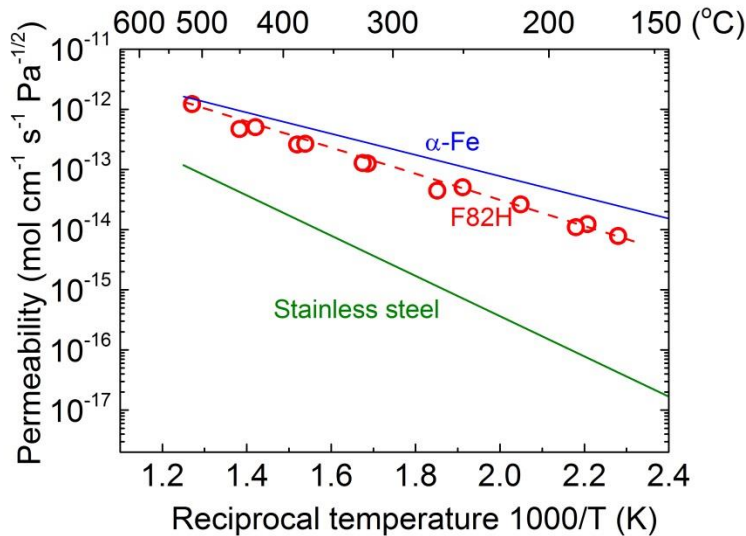


Figure 5.6 A comparison of the permeability of F82H, α -Fe and stainless steel. The permeability data for α -Fe and stainless steel are from literature [3].

5.5.3. Calculation results and discussion

Shown in Fig. 5.7 and Fig. 5.8 are the results of the DIFFUSE code executed for hydrogen PDP and GDP through a 0.6 mm thick α -Fe membrane. Figure 5.7 shows the hydrogen release flux from the plasma-facing surface. In the first 100 s, only plasma is produced. The hydrogen flux reaches $\sim 8.5 \times 10^{15}$ H-atoms/cm²/s (i.e. hydrogen recycling rate reaches $\sim 100\%$) within one second. From 100 s to 300 s, hydrogen gas is introduced at the plasma downstream side. An extra steady-state release flux of 1.3×10^{16} H-atoms/cm²/s can be observed, suggesting GDP takes place in the opposite direction of PDP. The hydrogen gas driving GDP is pumped out from $t = 300$ s and the steady-state release flux is found to decrease to the initial value in the first 100 s.

Although α -Fe is used as a surrogate of F82H for calculation, the estimated steady-state hydrogen GDP flux is relatively close to the experimental data (9.9×10^{15} H-atoms/cm²/s). These data mean the hydrogen recycling rate at the plasma-facing side of the membrane is larger than 1 under the experimental conditions examined in the present work.

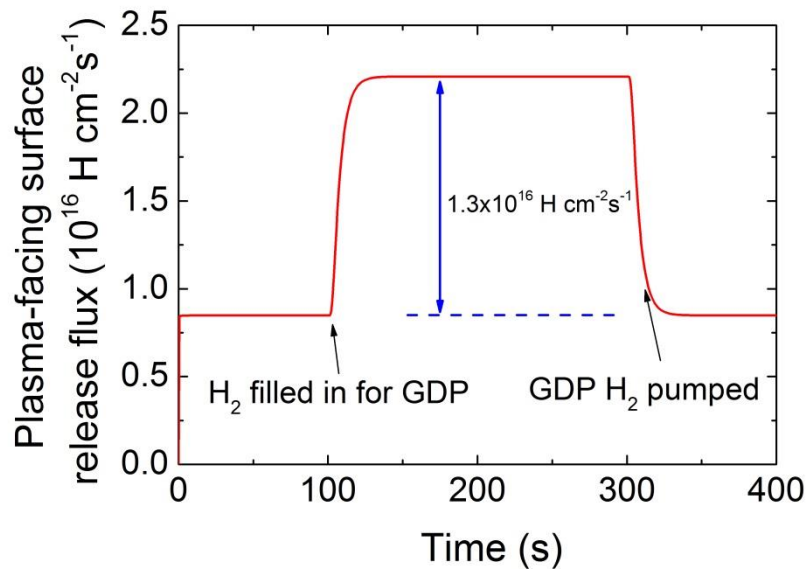


Figure 5.7 Hydrogen release flux from the plasma-facing surface.

Figure 5.8 shows the steady-state hydrogen concentration profiles for single plasma-driven permeation and bi-directional permeation. As indicated in Chapter 3, hydrogen transport inside the membranes is diffusion-limited under the current experimental conditions, which means hydrogen transport will be driven by the concentration gradient inside the membrane. For PDP-only case, the net hydrogen flow will be towards the plasma downstream side. When GDP takes place, the direction of the hydrogen concentration gradient would be reversed and the overall hydrogen transport will be towards the plasma upstream side.

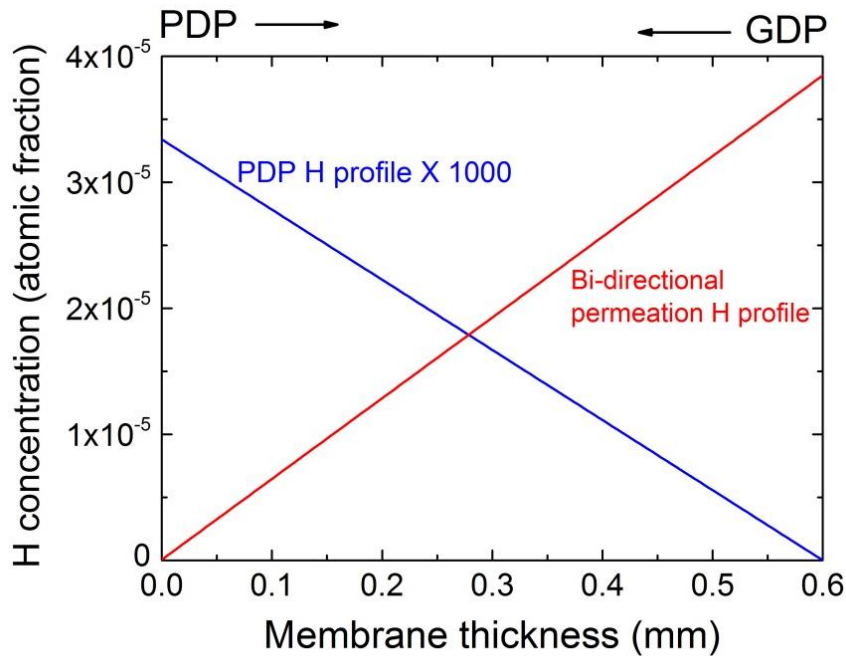


Figure 5.8 Steady-state hydrogen concentration profiles for plasma-driven permeation and bi-directional permeation. Note that the PDP hydrogen concentration profile has been enlarged by 1000 times.

5.6. Hydrogen plasma-driven permeation into hydrogen gas side

Hydrogen PDP from the plasma side to the gas side has been investigated as well. The results shown in the previous section indicate a net hydrogen flow from the gas side to the plasma side in the bi-directional permeation experiments. That means the hydrogen gas pressure at the PDP downstream will keep decreasing due to the loss of hydrogen. Then the PDP signal may be picked up from the decreasing rate of hydrogen pressure at the downstream side of the membrane. The total remaining hydrogen particle numbers in a closed volume at time t are given as $N_1(t)$ and $N_2(t)$ for the cases with and without PDP as:

$$N_0 - N_t - J_{\text{GDP}}ts + J_{\text{PDP}}ts = N_1(t) \quad (5.1)$$

$$N_0 - N_t - J_{\text{GDP}}ts = N_2(t) \quad (5.2)$$

where N_0 is the initial particle number, N_t is the number of particles trapped in the membrane, s is the surface area, J_{GDP} and J_{PDP} are the steady state GDP and PDP flux, respectively. The PDP flux can be evaluated by:

$$J_{\text{PDP}} = \frac{1}{s} \left(\frac{dN_1(t)}{dt} - \frac{dN_2(t)}{dt} \right) \quad (5.3)$$

Based on the above idea, bi-directional hydrogen permeation experiments have been performed with and without a bias of -100 V onto the sample membrane. Our previous experiments indicate that hydrogen PDP flux is much higher when the bias is applied [6]. Here the PDP flow is assumed to be negligible when the bias is off, i.e., only GDP. If a PDP flow into the gas side actually exists in the bi-directional permeation process, the decreasing rate of hydrogen gas pressure at the downstream side should be smaller than that of the GDP-only case.

Hydrogen gas is introduced into a closed volume (PDP downstream) with an initial hydrogen gas pressure of $\sim 6.93 \times 10^4$ Pa. Figure 5.9 shows the time evolution of hydrogen

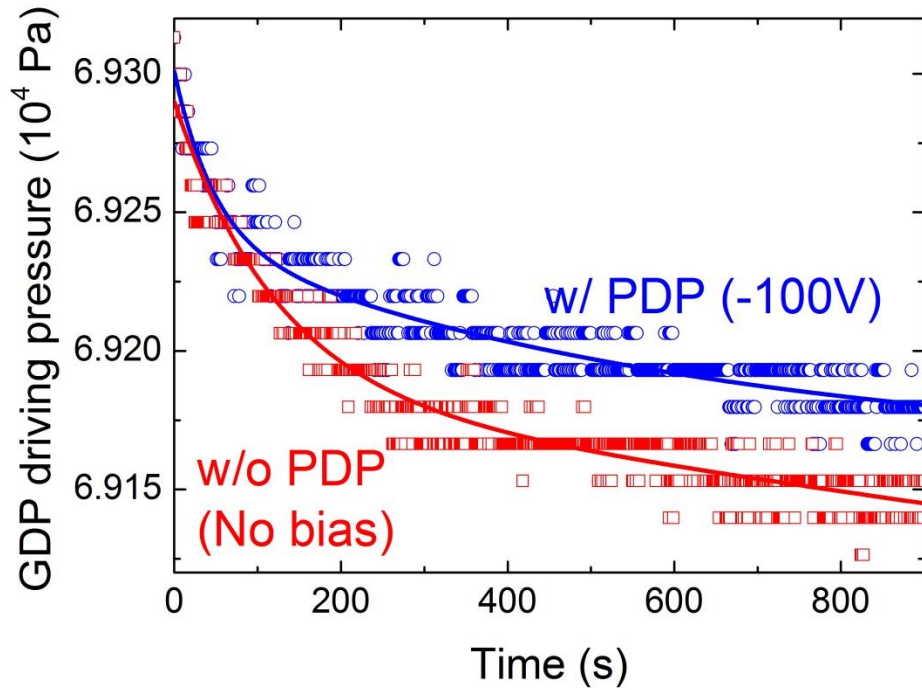


Figure 5.9 Variation of hydrogen gas pressures measured by an absolute pressure gauge at the PDP downstream side.

gas pressures for the two cases (i.e., w/ and w/o PDP). It can be seen that after the transient phases, both of the hydrogen pressures decrease, indicating hydrogen outflows to the plasma side. The difference in the two curves reflects the effect of PDP.

Using Eq. (5.3) and the steady state portion of the curves shown in Fig.5.9, the PDP flux is estimated to be $\sim 2.3 \times 10^{14}$ H/cm²/s, which is about 30% higher than theoretical prediction for the steady state PDP flux in the recombination-diffusion limited regime:

$$J_+ = \frac{D}{L} \sqrt{\frac{J_0}{K_r}} \quad , \quad (2.16)$$

where J_0 is the net implantation flux; L is the membrane thickness; D and K_r are the diffusion coefficient and surface recombination coefficient for F82H:

$$D = 7.5 \times 10^{-4} \exp\left(\frac{-0.14 \text{ [eV]}}{kT}\right) \quad (3.16)$$

$$K_r = 4.8 \times 10^{-21} \exp\left(\frac{0.48 \text{ [eV]}}{kT}\right) \quad (3.19)$$

5.7. Summary

The first-of-a-kind demonstration of hydrogen bi-directional plasma-driven permeation and gas-driven permeation has been performed. A one-dimensional code: DIFFUSE has been utilized to solve the hydrogen diffusion equations and the experimental observation has been successfully reproduced.

Gas-driven permeation has been found to take place in the opposite direction of PDP when the hydrogen gas driving pressure is high. These data suggest that for blankets employing those breeders with high tritium equilibrium pressures, GDP may dominate the overall hydrogen transport process and increase in first wall recycling. A hydrogen flow from the plasma side to the gas side has also been identified.

Unfortunately, at present deuterium cannot be used in our laboratory because of local regulation. For a fusion reactor, the edge plasma contains deuterium and tritium ions, suggesting that a clear understanding of the isotopes effects on the overall permeation behavior would be necessary for reactor design studies. This topic will be further discussed in the next chapter.

Reference

- [1] H. T. Lee et al., “*Ion-driven permeation of deuterium through tungsten under simultaneous helium and deuterium irradiation*”, *Journal of Nuclear Materials* 415, (2011) S696-S700.
- [2] M. I. Baskes, *DIFFUSE83*, Sandia Report SAND83-8231.
- [3] Möller and J. Roth, *Physics of Plasma-Wall Interaction in Controlled Fusion Devices*, Plenum Press, New York, 1986, p. 439–494.
- [4] S.H. Avner, *Introduction to physical metallurgy*. McGraw-Hill, Inc., New York, 1974, P. 257.
- [5] M. Tamura et al., *Development of potential low activation ferritic and austenitic steels*, *Journal of Nuclear Materials* 141-143 (1986) 1067-1073.
- [6] H. Zhou et al., *Hydrogen gas and plasma driven permeation in counter directions through the first wall of a DEMO reactor*, Paper presented at the 28th JSPF Annual Meeting, Kanazawa, Japan, Nov. 22nd-25th, 2011.

Chapter 6

Bi-directional hydrogen isotopes (D/T) permeation through the first walls of fusion reactors

6.1. Introduction

As mentioned earlier in this thesis, the first wall of a magnetic fusion reactor will be penetrated through by plasma-driven permeation of deuterium/tritium (D/T) from the edge plasma side, and by gas-driven permeation of tritium gas (T_2) from the blanket side. Since the isotopes effects are involved in the permeation process, new questions would be raised: (1) will hydrogen isotopes in these two flows “recognize” each other; (2) if they will, what would the resultant flows be like?

The modeling studies to address isotopes effects on bi-directional permeation are presented in this chapter. Based on all the data taken from experiments and calculations, case studies on hydrogen isotopes permeation through the first walls of magnetic fusion reactors have been performed.

6.2. Isotopes effects on permeation

Isotopes effects on hydrogen permeation have been briefly reviewed in section 2.3 of Chapter 2. In this section further details are discussed. Isotopes effects can be divided into two classes: intrinsic effects and synergistic effects [1]. The intrinsic effects are the differences in the transport properties of each of the individual isotopes, e.g., diffusivity. The synergistic effects involve the interaction of one isotope with another, i.e., the competition of the isotopes for traps and the coupling of various isotopes through the process of recombination.

6.2.1. Diffusivity and solubility

From the classical theory, the ratio of hydrogen isotopes diffusivities at a certain temperature is commonly inferred to be equivalent to the inverse ratio of the square root of the masses of the isotopes [2]:

$$\frac{D_T}{D_H} = \sqrt{\frac{m_H}{m_T}} \quad (6.1)$$

where D is the diffusivity and m is the mass of the respective isotope. Experimental data indicate that the inverse square root dependence on mass generally provides a reasonable approximation at elevated temperatures [2,3].

For the DIFFUSE-code calculation, the diffusion coefficient for the j^{th} diffusion species is given by [4]:

$$D_j(T) = D_0 M_j^{-0.5} \exp(-E_d / kT) \quad (6.2)$$

where D_0 is the pre-exponential for diffusivity, E_d is the activation energy for diffusion and M_j is the mass of the j^{th} species. The activation energy E_d is assumed to be the same for all the diffusion species.

The solubility (Sieverts' constant) S for all the hydrogen isotopes is assumed to be the same:

$$S = S_0 \exp\left(-\frac{U_s}{kT}\right). \quad (2.5)$$

The above-mentioned classical diffusion theory can be derived by quantum theories from classical considerations. If the classical theory applies, the prefactor of the hydrogen jump frequency would show the classical isotope dependence [5]. On the other hand, the isotopes effects on activation energy are neglectable. Further discussion on this topic would be beyond the scope of the present work.

6.2.2. Recombination coefficient

A widely accepted form of the recombination coefficient for diatomic molecules is given by [4]:

$$K_{jj'}(T) = \frac{4\alpha c_1}{\rho S_0^2 \sqrt{(M_j + M_{j'})T}} \exp(-U_k / kT) \quad (6.3)$$

where c_1 is the kinetic theory constant [6]; α is the sticking coefficient; ρ is the matrix density, S_0 is the pre-factor of solubility; M is the mass of hydrogenic atoms; U_k is the activation energy for recombination and $U_k = U_D - U_S$ when $U_D + U_S \geq 0$; and $U_k = -2U_S$ when $U_D + U_S < 0$.

Notice that the activation energy for recombination coefficient is related to the energy of diffusivity and the heat of solution, both of which do not show any observable isotopes effects [3,5].

6.2.3. Competition of the isotopes for traps

The third aspect of isotopes effect is the competition of the isotopes for traps. This process is described by the Eq. (2.20) given in Chapter 2:

$$\frac{\partial C^j(x,t)}{\partial t} = D_j(T) \frac{\partial^2 C^j(x,t)}{\partial x^2} - \sum_i \frac{\partial C_t^{ij}(x,t)}{\partial t} + G_j(x,t) \quad (2.18)$$

$$\frac{\partial C_t^{ij}(x,t)}{\partial t} = D_j(T) \frac{C^j(x,t) C_t^{ei}(x,t)}{\lambda^2} - C_t^{ij}(x,t) \nu_0 \exp(-U_t^i / kT) \quad (2.19)$$

$$C_t^{ei}(x,t) = C_t^{0i}(x) - \sum_j C_t^{ij}(x,t), \quad (2.20)$$

where $C^j(x,t)$ and $C_t^{ij}(x,t)$ are the concentrations of mobile j^{th} species and trapped j^{th} species in the i^{th} trapping site; D_j is the diffusion coefficient of the j^{th} species; $G_j(x,t)$ is the hydrogen implantation profile of the j^{th} species; U_t^i is the de-trapping energy of the i^{th} trapping site; $C_t^{0i}(x)$ and $C_t^{ei}(x)$ are the concentrations of intrinsic and empty i^{th} trapping sites, respectively. Although trapping sites introduced by neutron or energetic particle bombardment will not affect the steady state permeation behavior, the hydrogen isotopes retention would still be affected by trapping [4].

6.3. Modeling of bi-directional permeation involving multiple hydrogen isotopes

Presented in this section are some of the modeling results from DIFFUSE calculations to address isotopic effects on bi-directional permeation, which need to be verified experimentally, though. Simulating such complicated D/T-mixture conditions for bi-directional permeation, the following two cases have been analyzed for comparison:

Case-1: GDP-T₂ flows from both the upstream and downstream surfaces; and

Case-2: PDP-D/T and GDP-T₂ flows from the upstream and downstream surfaces, respectively.

Shown in Fig. 6.1 for Case-1 is the time evolution of the tritium concentration profiles by two GDP-T₂ flows from both the surfaces of a membrane. The assumptions used for DIFFUSE calculations are such that the thickness of a membrane made of α -Fe is 5 mm, the GDP-T₂ driving pressure is $\sim 10^4$ Pa and the membrane temperature is 527 °C. An intrinsic trap density of 1% atomic fraction and a trapping energy of 0.62 eV are assumed [7].

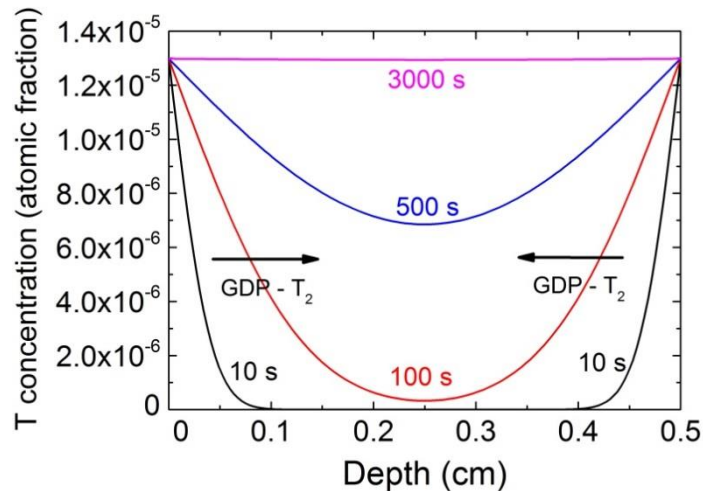


Figure 6.1 Case-1: Time evolution of T-concentration profiles calculated by the DIFFUSE-code for bi-directional GDP-T₂ from both surfaces, on which Sieverts' law is employed as the common boundary condition.

Recognize that the tritium concentration profiles associated with these two GDP-T₂ flows in the counter directions clearly interact with each other, exhibiting a relaxed curvature during the transient stage and then a straight line at steady state. Most interestingly here, the T-concentration gradient disappears at steady state, meaning that there is no net outflow of tritium to either side, indicating a quasi-thermodynamic “equilibrium” that permeation fluxes in the two directions are balanced.

For Case-2, two isotopes (D/T) and their flows in the two opposite directions that are driven by two mechanisms (PDP and GDP) are considered, a rather complicated but reactor-relevant situation. The input data for DIFFUSE are such that the thickness of a membrane made of α -Fe is 5 mm at a temperature of 527 °C, the D/T inflows from the upstream (plasma-facing) side are driven by PDP with D/T bombarding fluxes of 5×10^{15} D-atoms/cm²/s and 5×10^{15} T-atoms/cm²/s at a bombarding energy of 100 eV, and the T inflow from the downstream (gas-facing) side is driven by GDP with a tritium gas pressure of 1 Pa. Again, an intrinsic trap density of 1% atomic fraction and a tapping energy of 0.62 eV are assumed. Recombination release and Sieverts’ law are employed as the boundary conditions for the plasma-facing side and the gas-facing side, respectively.

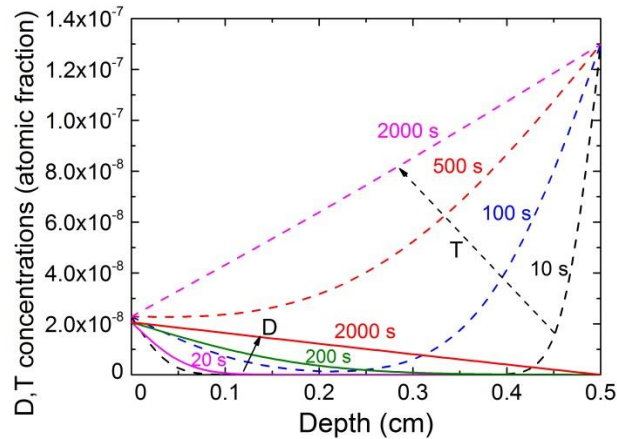


Figure 6.2 Case-2: Time evolution of D/T-concentration profiles calculated by the DIFFUSE-code for bi-directional PDP-D/T and GDP-T₂ from the upstream and downstream surfaces, respectively.

The time evolution of internal D/T concentrations calculated under these conditions is shown in Fig. 6.2. Here, note that T-concentration shows the sum of the contributions from the two flows: one is due to PDP and the other is due to GDP, whereas D-concentration is only due to the PDP flow.

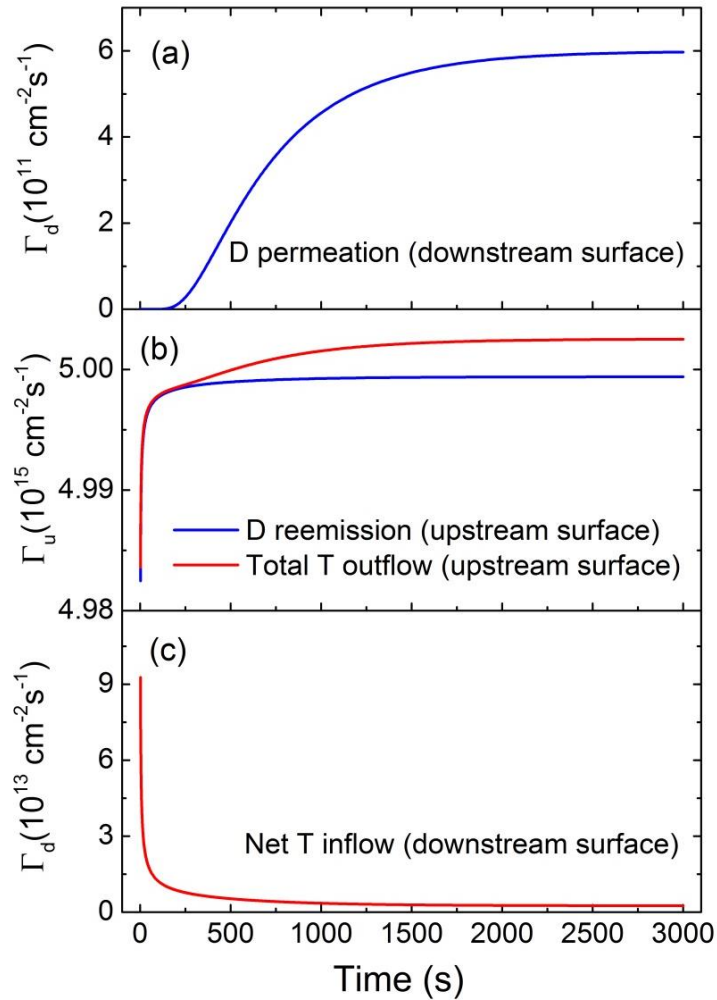


Figure 6.3 (a) D-permeation by PDP, (b) D-reemission by PDP and total T-outflow (i.e. reemission by PDP plus permeation by GDP) and (c) Net T-inflow from the downstream surface (i.e. absorption by GDP minus permeation by PDP). Here, Γ_u and Γ_d are the flows from the upstream and downstream surface, respectively.

As opposed to Case-1 shown in Fig. 6.1, one finds that there are clearly concentration gradients at steady state, indicative of diffusion-limited D/T flows. These D/T inflows and outflows are shown in Fig. 6.3.

Because it is independence of other flows, the D-flow driven by PDP is most straightforward to understand in that one sees the permeation and reemission fluxes, respectively, in Fig. 6.3 (a) and Fig. 6.3 (b). As to the T-flows, each driven by PDP and GDP, note that the total outflow shown in Fig. 6.3 (b) is larger than D-reemission because of the contribution of permeation from the downstream side driven by GDP. In other words, the difference here is the diffusion-limited T-inflow from the downstream side by GDP-T₂. Finally, the net T-inflow, shown in Fig. 6.3 (c), is equal to the absorption flux by GDP-T₂ from the downstream surface minus the permeation flux by PDP-D/T from the upstream surface.

6.4. Re-evaluation of the tritium pressure in FLiBe blankets

For the GDP experiments presented in Section 3.7.3, the hydrogen gas pressure is assumed to be the T₂ equilibrium gas pressures in the breeders at a T concentration of 0.1 ppm (i.e. $\sim 10^4$ Pa at 527 °C). However, fusion reactor studies indicate that the T₂ gas pressure in a blanket is related to a number of factors, e.g., fusion power, tritium breeding ratio, tritium recovery rate, structural material, temperature, flow rate of the breeder, etc.

In previous studies, evaluation of the T₂ gas pressure in the tritium loop was done by other researchers [8], assuming no T leakage from the first wall. Under these conditions, the pressure was found to be 10^3 - 10^4 Pa, depending on the integration method of the tritium recovery system. Preliminary tritium analysis for the blanket employing FLiBe was performed as well [9]. In the presence of tritium permeation barrier, the T₂ pressure varied from 5×10^3 – 4.5×10^4 Pa as a decrease of tritium recovery efficiency. To analyze the

For the blanket of a 3 GW fusion reactor with a tritium breeding ratio (TBR) of 1.3 [10], the tritium breeding rate J_1 is estimated to be 1.38×10^{21} T-atoms/s (6.89×10^{-3} g/s T); The hydrogenic ion implantation flux is assumed to be 1×10^{16} atoms/cm²/s (50% T and 50% D), which will lead to a steady state PDP flux of 1×10^{13} atoms/cm²/s, i.e., $J_2 = 2.5 \times 10^{-4}$ g/s T for a plasma facing surface area of 1000 m².

For calculating the tritium leakage from the first wall by GDP, the total surface area of the blankets modules is 3000 m² for a helical type reactor [10] and the wall thickness L is 5 mm [11]. The permeation flow J_{3-wall} is given by:

$$J_{3-wall} = DS \frac{\sqrt{p_{T_2}}}{L_{wall}} A_{wall} = P_{wall} \frac{\sqrt{p_{T_2}}}{L_{wall}} A_{wall} \quad (6.5)$$

where A_{wall} is the blanket surface area; D and S are the diffusion coefficient and solubility, respectively; $P_{wall} = DS$ is the permeability of hydrogen in the first wall material.

Similarly, the tritium leakage from pipes and the heat exchanger (HX) by GDP are expressed as following:

$$J_{3-pipe} = P_{pipe} \frac{\sqrt{p_{T_2}}}{L_{pipe}} A_{pipe} \quad (6.6)$$

$$J_5 = P_{HX} \frac{\sqrt{p_{T_2}}}{L_{HX}} A_{HX} \quad (6.7)$$

The tritium extracted by the tritium recovery system J_4 is given by:

$$J_4 = \chi FC_o = \chi FKp_o \quad (6.8)$$

where χ is the tritium recovery rate; F is the flow rate of FLiBe; K is the tritium solubility constant for FLiBe; C_o and p_o are the T_2 concentration and pressure at the breeder outlet, respectively.

The average T_2 pressure p_a driving GDP through the first wall is assumed to be the average of outlet pressure p_o and inlet pressure p_i . In the present study, the coolant pipes material and the heat exchanger material are assumed to be stainless steel and tungsten, respectively. The permeability data of these materials are available from literatures [12,13]. The other input data for the calculation are as follows: the FLiBe flow rate is 2.2×10^6 m³/s; the tritium solubility is 5.3×10^{-13} wt fraction/Pa [14]; the tritium recovery efficiency is 0.99; the surface area and thickness data for the coolant pipes and heat exchanger are the same as those used in literature [9].

Solving Eq. (6.4) for a steady state condition, the tritium pressure has been found to be $\sim 1.1 \times 10^3$ Pa, which is only $\sim 10\%$ of the tritium equilibrium pressure in FLiBe is only $\sim 10\%$ of the estimated T_2 equilibrium pressure in FLiBe at a T concentration of 0.1 ppm at 527 °C. Under these conditions, $\sim 4.7 \times 10^{-3}$ g/s T will be released from the first wall by gas-driven permeation, which means $\sim 68\%$ of the bred tritium will be released back to the plasma side.

6.5. Re-evaluation of hydrogen isotopes permeation through the first wall of FLiBe blankets

6.5.1. Evaluation of the hydrogen isotopes permeation fluxes

For magnetic fusion reactors, the first wall serves to separate the vacuum/plasma and the coolant/breeder at elevated temperatures, whereby hydrogen isotopes flow in and out in the two opposite directions simultaneously through the first wall. Using the tritium partial pressure data shown in previous section, hydrogen isotopes permeation through the first wall of FLiBe blankets has been re-evaluated by DIFFUSE-code as well.

The input data for DIFFUSE calculation are as follows: the first wall thicknesses are assumed to be 5 mm and the implanted hydrogenic fluxes (D/T) at the plasma-facing side are assumed to be 1×10^{16} atoms/cm²/s (5×10^{15} D -atoms/cm²/s and 5×10^{15} T-atoms/cm²/s) with a bombarding energy of 100 eV. At the blanket side, the tritium gas pressure is 1.1×10^3 Pa. The first wall temperature is assumed to be the average temperature of the inlet (500 °C) and outlet (600 °C) coolant temperatures. The trap density and tapping energy data are the same as the previous calculation.

Figure 6.5 shows the time evolution of the tritium and deuterium concentration profiles calculated by the DIFFUSE-code. Recognize that the T-concentration profile reflects two contributions: one by PDP from the upstream surface and the other by GDP from the downstream surface, whereas the D-concentration profile is only due to PDP. Here, note that the D concentration shown in Fig. 6.5 is enlarged by 100 times. The actual T concentration at the plasma-facing surface (depth ≈ 0) is larger than that of D.

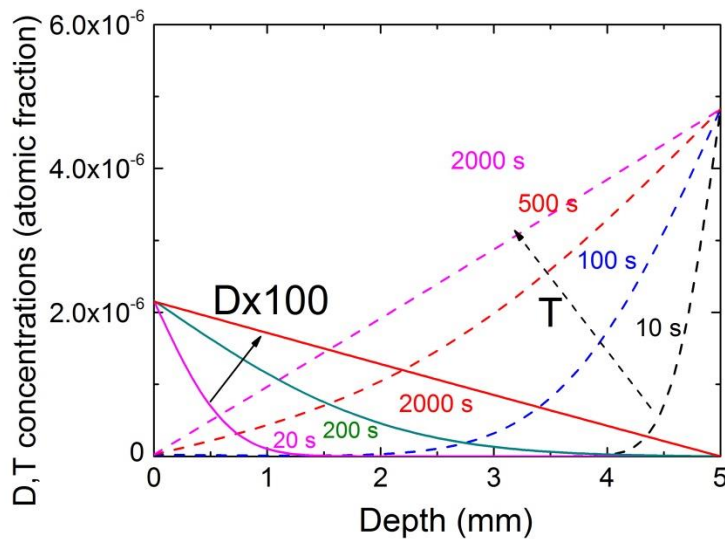


Figure 6.5 D/T-concentration profiles calculated by the DIFFUSE-code for bi-directional PDP-D/T and GDP-T₂ from the plasma-facing and breeder-facing surfaces, respectively.

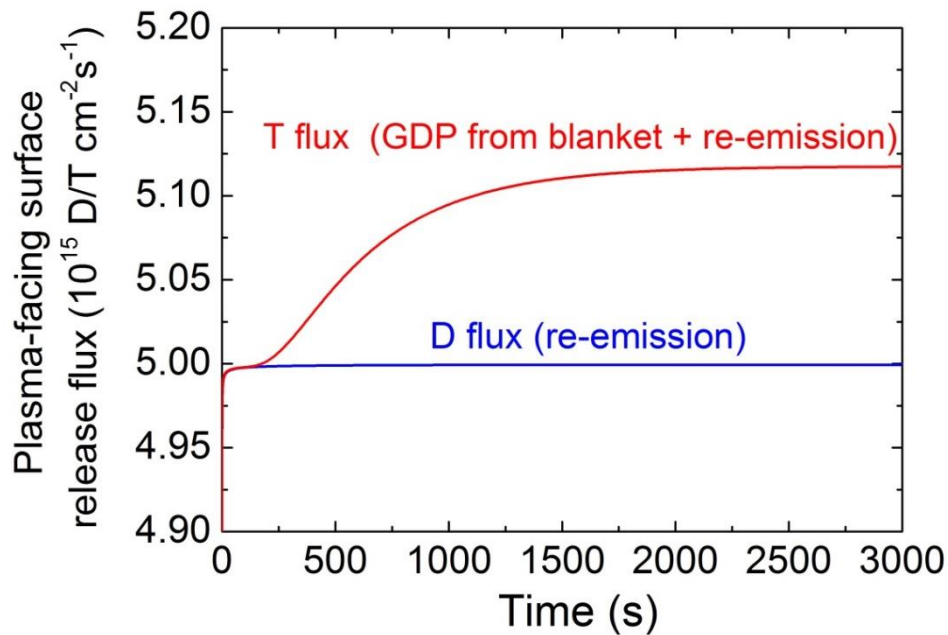


Figure 6.6 D/T release fluxes at the plasma-facing surface calculated by the DIFFUSE-code for bi-directional PDP-D/T and GDP-T₂. The total T flux is composed of the re-emission flux of the implanted T and the GDP-T from the blanket side.

Figure 6.6 shows the D and T release fluxes at the plasma-facing surface calculated by the DIFFUSE-code. The difference in T and D fluxes is mainly due to the T-GDP from the blanket side. The T-GDP flux is about 1.2×10^{14} T-atoms/cm²/s, which is 0.6% of the total incident flux. These data indicate that the hydrogen recycling rate at the plasma-facing surface would be > 100%, which will affect the edge plasma density control. Coating as a hydrogen isotopes permeation barrier would be necessary. However, the quality control of the coating would pose another technical issue because of the large surface area (several thousand m²). Note that the D flow appears to be independent of these tritium flows, driven

by its own concentration gradient in all the conditions examined in this work. That means isotopes separation would be necessary in the tritium recovery loop.

6.5.2. Evaluation of the possible impact of GDP on first wall recycling

Taking into hydrogen isotopes permeation into account, the first wall recycling rate R is defined as:

$$R = \frac{\Gamma_{\text{reflection}} + \Gamma_{\text{re-emission}} + \Gamma_{\text{GDP}}}{\Gamma_{\text{plasma}}}, \quad (6.9)$$

where Γ_{plasma} is the total incident ion flux from edge plasma; $\Gamma_{\text{reflection}}$ is the particle flux by surface reflection; $\Gamma_{\text{re-emission}}$ is the particle flux by remission and Γ_{GDP} is the steady state plasma- gas-driven permeation flux. The flux relation is shown in Fig. 6.7.

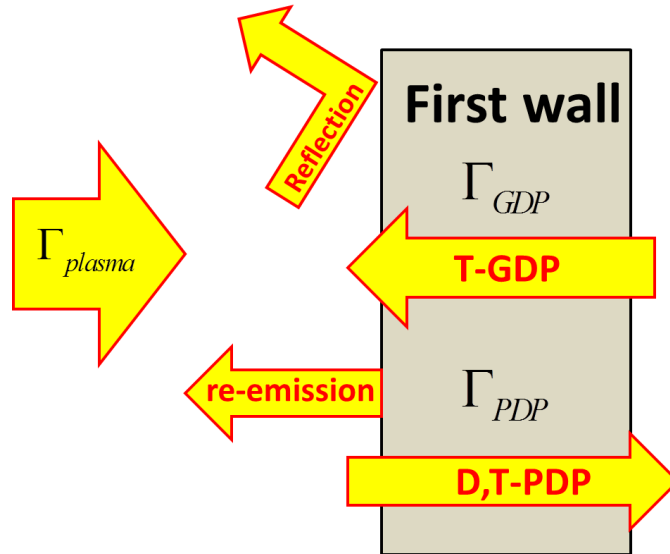


Figure 6.7 A schematic diagram of the fluxes involved in the bi-directional hydrogen isotopes permeation.

Experimental data (Fig. 3.30) indicate that the GDP permeation flux can be overwhelmingly larger than that of the PDP flux. In the particular case, the first wall recycling rate can be as high as $R = 1.025$. Notice that this result is based on the assumption that the GDP driving pressure is 10^4 Pa, which will not be realistic according to the analysis results shown in section 6.4.

The first wall recycling rate can be re-evaluated using the newly obtained flux data from DIFFUSE. Assuming a particle reflection coefficient of 0.5 and a wall flux of $\Gamma_{\text{plasma}} = 1 \times 10^{16}$ atoms/cm²/s, the total incident flux would be 2×10^{16} D&T·cm⁻²·s⁻¹ and the first wall recycling rate has been estimated to be $R = 1.006$.

6.6. Summary

To simulate more reactor-relevant conditions, the DIFFUSE-code has extensively been executed, employing multiple hydrogen isotopes (D/T) for bi-directional permeation. Results indicate that the same isotopic species in the counter flows interact with each other, affecting internal concentration profiles, whereby the resultant inflow and outflow from the upstream and downstream surfaces are modified in an interesting manner. Nevertheless, all these theoretical predictions should be experimentally verified.

Re-analysis of the tritium flows in a FLiBe loop has been conducted, taking into account tritium leakage from the first wall. The tritium pressure has been found to be 1.1×10^3 Pa, which is only ~10% of the tritium equilibrium pressure in FLiBe at a temperature of 527 °C. Under these conditions, ~68% of the bred tritium will be released at the plasma side by GDP and the first wall recycling rate has been estimated to be $R = 1.006$.

Reference

- [1] D. K. Brice, *Steady state hydrogen transport in solids exposed to fusion reactor plasmas, part III: Isotope effects*, Journal of Nuclear Materials 122&123 (1984) 1531.
- [2] R. Causey et al., *Tritium barriers and tritium diffusion in fusion reactors*, in Comprehensive Nuclear Materials, 1st edition, Elsevier, 2012.
- [3] H.H. Johnson, *Hydrogen in iron*, Metallurgical Transactions, A19 (1988) 2371.
- [4] M. I. Baskes, *DIFFUSE83*, Sandia Report SAND83-8231.
- [5] K. W. Kehr, *Theory of the Diffusion of Hydrogen in Metals*, in Hydrogen in metals I, Springer-Verlag, Berlin, 1978.
- [6] M.I. Baskes, *A calculation of the surface recombination rate constant for hydrogen isotopes on metals*, Journal of Nuclear Materials 92 (1980) 318.
- [7] Möller and J. Roth, *Physics of Plasma-Wall Interaction in Controlled Fusion Devices*, Plenum Press, New York, 1986, p. 439–494.
- [8] S. Fukada et al., *Diffusion coefficient of tritium through molten salt FLiBe and rate of tritium leak from fusion reactor system*, Fusion Science and Technology 48 (2005) 666.
- [9] Y. Song et al., *Analysis on tritium management in FLiBe blanket for LHD-type helical reactor FFHR2*, Plasma and Fusion Research 7 (2013) 245016.
- [10] A. Sagara et al., *Design activities on helical DEMO reactor FFHR-d1*, Fusion Engineering and Design 87 (2012) 594.
- [11] A. Sagara, et al., *Studies on FLiBe blanket designs in helical reactor FFHR*, Fusion Technology 39 (2001) 753.
- [12] C. San Marchi et al., *Permeability, solubility and diffusivity of hydrogen isotopes in*

- stainless steels at high gas pressures*, International Journal of Hydrogen Energy 32 (2007) 100.
- [13] E. Serra et al., *Hydrogen isotopes transport parameters in fusion reactor materials*, Journal of Nuclear Materials 255 (1998) 105.
- [14] S. Fukada, *A design for recovery of tritium from FLiBe loop in FFHR-2*, Japan-US Workshop on Fusion Power Plants and Fusion Power Plants and Related Advanced Technologies with Participation of EU, Kyoto, Japan, Feb. 5, 2007.

Chapter 7

Summary and outlook

7.1. Summary

The first wall is defined as the plasma-facing surfaces of the blanket units, whereby hydrogen isotopes flow in and out in the two opposite directions simultaneously through the first wall: in one direction by plasma-driven permeation (PDP) and in the other direction by gas-driven permeation (GDP). In this PhD thesis work, hydrogen isotopes permeation behavior through the first wall of a magnetic fusion power reactor has been studied.

A laboratory-scale plasma device (VEHICLE-1) has been installed with an experimental setup for bi-directional hydrogen permeation by PDP and GDP under conditions to be seen in the first wall environment. The hydrogen transport parameter data taken for SUS304 have been found to be in good agreement with the literature data, which means that the experimental setup on VEHICLE-1 is valid for the evaluation of other first wall candidate materials.

Both GDP and PDP of hydrogen through F82H have been found to be diffusion-limited under all the experimental conditions examined in this work. The hydrogen transport parameters such as permeability, solubility and diffusion coefficient have been evaluated for F82H from the GDP data. The recombination coefficient of hydrogen on a ferritic steel alloy has been experimentally evaluated from the PDP data for the first time.

The surface effects on hydrogen PDP have been investigated from two aspects: surface contamination and surface area. A new model has been proposed to interpret the surface condition effects. Thick surface impurity film (tens of μm) has been found to act as a second layer for diffusion and reduce the permeation flux. The steady state permeation flux has been found to be inversely proportional to the square root of surface area. Combined surface condition effects have been observed when the surface area-increased sample is oxidized.

A one-dimensional diffusion code: DIFFUSE-code has extensively been executed, employing multiple hydrogen isotopes (D/T) for bi-directional permeation. Results indicate that the same isotopic species interact with each other in the two counter flows. Deuterium

flow appears to be independent of these tritium flows, driven by its own concentration gradient.

Re-analysis of the tritium flows in a FLiBe loop has been performed, taking into account tritium leakage from the first wall. The tritium pressure has been found to be 1.1×10^3 Pa. Under these conditions, the first wall recycling rate has been estimated to be 1.006.

7.2. Outlook

This PhD thesis work has established some fundamental knowledge databases for fusion reactor design, which makes a contribution to magnetic fusion research in the field of fusion engineering. Using the data and methods presented in this thesis, it is possible to analyze hydrogen isotopes permeation behavior through the first walls under some of the reactor-relevant conditions.

For more precise evaluation of the hydrogen isotopes permeation flows through the first wall of a fusion reactor, more efforts are still required on this subject. Listed here are two aspects which warrant further investigation:

(1) Experimental validation of the bi-directional permeation behavior of multiple hydrogen isotopes. DIFFUSE-code calculations have been done to address isotopic effects on bi-directional permeation, which need to be verified experimentally. Unfortunately, only hydrogen can be used in the present experiments because of the local regulation. If deuterium is usable, the modeling results should be examined by experiments.

(2) The wetting effects of breeder on hydrogen isotopes permeation. For self-cooled molten salt and liquid metal breeders, the blanket-facing side of the first wall will be completely wetted by liquid. Under such conditions, the validity of Sieverts' law must be examined because most permeation studies for blanket structure materials are based on the assumption that hydrogen isotopes will arrive at the first wall in a molecular form.

List of publications

- [1] **H. Zhou**, Y. Hirooka, H. Zushi, A. Kuzmin, N. Ashikawa, T. Muroga, A. Sagara and the QUEST group, “*Effects of surface conditions on the plasma-driven permeation behavior through a ferritic steel alloy observed in VEHICLE-1 and QUEST*”, accepted by Journal of Nuclear Materials, November, 2014.
- [2] **Haishan Zhou**, Yoshi Hirooka, Naoko Ashikawa, Takeo Muroga and Akio Sagara, “*Gas- and plasma-driven hydrogen permeation through a reduced activation ferritic steel alloy F82H*”, Journal of Nuclear Materials 455 (2014) 470–474.
- [3] **Haishan Zhou**, Yoshi Hirooka, Hideki Zushi, Arseniy Kuzmin and the QUEST group, “*First wall particle flux measurements by an F82H permeation probe in QUEST*”, Plasma and Fusion Research 9 (2014) 3405041.
- [4] **H. Zhou**, Y. Hirooka, N. Ashikawa, T. Muroga, A. Sagara “*Hydrogen plasma-driven permeation through a reduced activation ferritic steel alloy F82H*”, Fusion Science and Technology T63 (2013) 361–363.
- [5] **Haishan Zhou**, Yoshi Hirooka, Naoko Ashikawa, Takeo Muroga and Akio Sagara, “*Bi-directional hydrogen permeation through F82H under DEMO-relevant conditions*”, Plasma and Fusion Research 8 (2013) 2402065.
- [6] **Haishan Zhou**, Yoshi Hirooka, Naoko Ashikawa and Takeo Muroga, “*Bi-Directional Hydrogen Isotopes Permeation through the First Wall of a Magnetic Fusion Power Reactor*”, paper submitted to Journal of Plasma and Fusion Research, under review.
- [7] Yoshi Hirooka and **Haishan Zhou**, “*Laboratory experiments and modelling on bi-directional hydrogen isotopes permeation through the first wall of a magnetic fusion DEMO reactor*”, Fusion Science and Technology 66 (2014) 63–69.
- [8] Yoshi Hirooka, **Haishan Zhou** and Masa Ono, “*Hydrogen and Helium Recycling from Stirred Liquid Lithium under Steady State Plasma Bombardment*”, Fusion Engineering and Design 89 (2014) 2833–2837.
- [9] Yoshi Hirooka, **Haishan Zhou**, Naoko Ashikawa, Takeo Muroga, Akio Sagara, “*Plasma- and gas-driven hydrogen isotope permeation through the first wall of a magnetic fusion power reactor*”, Fusion Science and Technology 64 (2013) 345–350.
- [10] Feng Liu, **Haishan Zhou**, Xiao-Chun Li, Yuping Xu, Zhongqing An, Hongmin Mao, Guang-Nan Luo, “*Deuterium gas-driven permeation and retention in tungsten foils with intrinsic defects*”, Journal of Nuclear Materials 455 (2014) 248–252.